Mix & Match Nanodendrons for Detection & Treatment of Breast Cancer Metastases

By

Randy Lee Ray Scherer

Dissertation

Submitted to the Faculty of the

Graduate School of Vanderbilt University

In partial fulfillment of the requirements

For the degree of

DOCTOR OF PHILOSOPHY

In

Interdisciplinary Materials Science

May, 2010

Nashville, Tennessee

Approved:

Lynn M. Matrisian

Todd D. Giorgio

Darryl J. Bornhop

J. Oliver McIntyre

Todd E. Peterson

Thomas E. Yankeelov

To my parents for always telling me I could do anything I put my mind towards, to

my friends for all the fun memories, and to my wife for her infinite love and never

ending support.

ORIGINAL PUBLICATIONS

Scherer RL, VanSaun MV, McIntyre JO, Matrisian LM (2008). Optical Imaging of Matrix Metalloproteinase-7 Activity *In Vivo* Using a Proteolytic Nanobeacon. *Molecular Imaging* 7: 118-131, 2008

Scherer RL, McIntyre JO, Matrisian LM (2008) Imaging Matrix Metalloproteinases in Cancer. *Cancer and Metastasis Reviews* 27:679-690, 2008

Scherer RL, Kobayash H, Lin CP (2010) Cancer Nanotechnology Offers Great Promise for Cancer Research and Therapy. *Cancer Metastasis: Biologic Basis and Therapeutics* (In Press 2010)

Yu SS, Scherer RL, Ortega RA, Bell CS, Soman CP, O'Neil CP, Hubbell JA, Giorgio, TD (2010) Preparation of multifunctional polymer-iron oxide nanoparticle micelles: Application to magnetic relaxation switch biosensors. (In preparation)

McIntyre JO, Scherer RL, Matrisian LM (2010) Near Infrared Optical Proteolytic Beacons for *In Vivo* Imaging of Matrix Metalloproteinase Activity. (In Press 2010)

ACKNOWLEDGEMENTS

TABLE OF CONTENTS

LIST OF TABLES

LIST OF FIGURES

ABBREVIATIONS

ABP: Activity Based Probes

ABX: Abraxane or Albumin Bound Paclitaxel

Ala: Alanine

AF: AlexaFluor

AHX: Aminohexanoic acid

AOA: Aminoacetyl:

APC: Adenomatous Polyps

C: Cysteine

CPP: Cell-Penetrating Peptide

CuAAC: Cu(I) catalyzed 1,3dipolar azide alkyne cycloaddition

DAA: D-Amino Acid

DMF: Dimethylformamide

DMSO: Dimethylsulfoxide

DOX: Doxorubicin

ECM: Extracellular Matrix

EPR: Enhanced Permeability and Retention Effect

Eq: Equivalent

FDG: [18F]-2-deoxy-2-fluoro-D-glucose

FRET: Förster Resonance Energy Transfer

G: Generation

HPLC: High Performance Liquid Chromatography

IP: Intraperitoneally

LLC: Lewis lung cell

MIN: Multiple intestinal neoplasia

MMP: Matrix metalloproteinase

MMPI: Matrix metalloproteinase inhibitor

MMTV: Multiple mammary tumor virus

MRI: Magnetic Resonance Imaging

MT-MMP: Membrane Type-MMP

ND: Nanodendron

ND^{PB}: Nanodendron Proteolytic Beacon G2 dendron

$ND_3{}^{PB}$: Nanodendron Proteolytic Beacon G3 dendron

ND^{Pxl}: Nanodendron Prodrug PXL G2 dendron

$ND_3{}^{PXL}$: Nanodendron Prodrug PXL G3 dendron

$ND_3{}^{Pxl}ND_3{}^{Pxl}$: Combined Prodrug-Proteolytic Beacon G3 dendron

NIR: Near Infrared

OCT: Tissue Freezing Compound

OIM: Optical Imaging

PAMAM: Poly(amidoamine)

PB: Proteolytic Beacon

PEG: Polyethylene glycol

PET: Positron emission tomography

PXL: Paclitaxel

PyVT: Polyoma virus middle T antigen

R: Reference

RES: Reticuloendothelial system

RO: Retro-orbitally

S: Sensor

SEC: Size-Exclusion Chromotography

SPECT: Single Photon Emission Computed Tomography

SUV: Standardized uptake value

TBTA: tris-(benzyltriazoylmethyl)amine

TGI: Tumor growth inhibition

THF: Tetrahydrofuran

TIMP: Tissue specific inhibitors of MMPs

CHAPTER I

INTRODUCTION

Breast Cancer and Metastatic Disease

The National Cancer Institute estimates there will be 195,000 new cases of breast cancer in the United States in 2009 and approximately 40,170 deaths from the disease [1]. Cancer morbidity is related to the ability of tumor cells to metastasize throughout the body; therefore, early detection is critical to improving treatment and survival. Women with localized breast cancers treated with surgery have a 97.5% five-year survival rate, but survival drops to 25.5% for women with distant metastases [2]. Early detection of both primary tumors and metastatic disease remains a major challenge in diagnosing and staging cancer. The need to selectively identify and eliminate very small clusters of abnormal cells calls for sophisticated new technologies and emerging data suggests that nanotechnology may provide new avenues for progress.

Metastasis is the spread of disease from its origin to a different location and is the hallmark of late stage (stage IV) breast cancer. Metastasis is a complex process in which a cancerous cell must break away from the primary tumor site, degrade proteins that make up the extracellular matrix, and migrate to other areas of the body via the bloodstream or lymphatic system [3]. Metastatic lesions themselves go through stages of progression in that they start as single or small clusters of cells that must survive in a foreign organ, establish a competent microenvironment,

grow, and undergo an angiogenic switch before they become clinically detectable metastases [4]. Cancer cells frequently spread to the lymph nodes near the primary tumor site, but can spread to almost any part of the body. The main sites for metastases are the lungs, bone, liver and brain [1]. In breast cancer the survival benefit of adjuvant therapy, in which an estimated 35% of women have non-detected, micrometastatic disease at the time of first diagnosis, supports the notion that targeting of "early stage" metastases can be effective in reducing early mortality due to metastatic diseases.

Current Cancer Therapies

Metastatic disease is treated with chemotherapy, radiation therapy, biological therapy, hormone therapy, surgery, cryosurgery, or a combination of the above. The treatment commonly depends on the type of primary cancer, the size and location of the metastasis, the patient's age and general health, and the types of treatments the patient has had in the past. Current adjuvant therapies for breast cancer are nonselective in that they target dividing cells or the estrogen pathway with associated side-effects on normal cells. Adjuvant therapies are quite effective at killing tumor cells; however, their non-selective nature 1) Leads to a number of nasty side-effects that reduce a patient's quality of life (especially since treatments are usually long term) and 2) Limits the dosage due to toxicity issues. Furthermore, the delivery agents/vehicles for some of these agents further exacerbates this problem.

Chemotherapy drugs are designed to enter the bloodstream, travel throughout the body and destroy cancer cells. These drugs are given as pills or injections, and are commonly administered over three to six months anywhere from weekly to two- or three-week cycles. There are currently seven common drugs given as adjuvant therapy for breast cancer patients; Cyclophosphomide (Cytoxan), Docetaxel (Taxotere), Doxorubicin (Adriamycin), Epirubicin (Ellence), Fluorouracil (Adrucil), Methotrexate (Trexall), and Paclitaxel (Taxol) [5]. In general, chemotherapy drugs target proliferating cells and interrupt the cell cycle in some manner to cause cell death. This systemic administration leads to the multiple side-effects associated with these drugs; most commonly nausea, vomiting, loss of appetite, hair loss, and lowered blood counts. See TABLE 1 for general drug functions and the common short/long term side-effects.

Table 1: Common Chemotherapies & Their Side-effects (modified from [5])

Drug	Method of Function	Side-effects
Cyclophosphamide	Growth Inhibition by blocking DNA translation	1,2,3,4,5,6,7,11
Docetaxel	Disruption of cellular machinery in cellular division	1,2,3,4,5,6,8,9,10
Doxorubicin	Insertion into DNA to block DNA translation	1,2,3,4,5,6,8,9,10
Epirubicin	Insertion into DNA to block DNA translation	1,2,3,4,5,6,7,11,14
Fluorouracil	Blocks enzymes necessary for DNA synthesis	1,2,3,4,5,6,7,10,12
Methotrexate	Inhibits an enzyme necessary for DNA synthesis	1,2,3,4,7,12,
Paclitaxel	Disruption of cellular machinery in cellular division	1,2,3,4,5,6,7,9,14

1	Nausea	8	Rash
2	Diarrhea	9	Peripheral neuropathy
3	Vomiting	10	Nail changes
4	Loss of appetite	11	Amenorrhea
5	Hair loss	12	Sensitivity to sun
6	Low blood count	13	Muscle aches
7	Mouth sores	14	Fatigue

Paclitaxel

Paclitaxel (PXL) based regimens are the current standard of care for early and advanced breast cancer. PXL is an anti-microtubule agent that promotes the assembly of microtubules from tubulin-dimers and stabilizes microtubules by binding to the hydrophobic pocket within the central domain to prevent depolymerization [6]. This stability results in the inhibition of the normal dynamic reorganization of the microtubule network that is essential for vital interphase and mitotic cellular functions. PXL induces abnormal arrays or bundles of microtubules throughout the cell cycle and forms multiple asters of microtubules during mitosis. The mechanism of paclitaxel action is concentration dependent; at high concentrations paclitaxel increases polymer mass and induces microtubule bundle formation in interphase cells while at low concentrations paclitaxel suppresses microtubule dynamics without altering polymer mass [7]. PXL has been shown to be effective in anthracycline-resistant metastatic breast cancer either as single agent, or in combination with anthracyclines such as doxorubicin (DOX) [8-13]. To date, several major prospective randomized clinical trials of at least 1000 patients with either only node-positive disease (two studies) or including both node-positive and high-risk node-negative breast cancer patients, showed significant improvements in terms of efficacy when PXL is administered post-operatively as compared with anthracycline-based regimens [14, 15].

While PXL is now considered the standard and preferred chemotherapy for early high-risk and metastatic breast cancer patients, the solvents used as vehicles in its formulation cause severe toxicities, mainly hypersensitivity reaction,

myelosuppression and neurotoxicity. The primary site of pathogenesis of PXL-induced peripheral neuropathy is not clear; with this major side-effect being dependent on the dose per treatment cycle, schedule and duration of infusion [16, 17]. Complications may also result from the toxicologic and pharmacologic behavior of Cremaphor, the emulsion solvent system used for paclitaxel [18]. The efficacy of administration of neuroprotective agents remains to be validated; and, peripheral neuropathy including muscle pain remains a significant quality-of-life issue for paclitaxel therapy [17]. New formulations of PXL, such as albumin-bound PXL (nab-PXL), are more effective in terms of solubility and vehicle toxicity. However, despite decreased rates of myelosuppression and hypersensitivity reactions, neurotoxicity is still a significant and sometimes permanent problem [19]. For patients with metastatic breast cancer, a head-to-head comparison study of albumin-bound PXL against PXL, showed significant improvements in both time-to-progression and objective response rates together with less neutropenia but with higher neuropathy rates [20]. Recent reports describing new formulations of PXL, including a poly(amidoamine) (PAMAM) dendrimer conjugate of paclitaxel, reflect the need for improved formulation of this useful chemotherapeutic agent [21-24]. Cancer patients' treatments would be improved dramatically by 1) Identifying and monitoring growth at metastatic sites, and 2) Delivering drug agents to the diseased tissue site in a more specific manner.

Mouse Models of Breast Cancer

The Multiple Mammary Tumor Virus (MMTV)-driven polyoma virus middle T antigen (PyVT) transgenic mouse, developed by Muller and colleagues in 1992 [25], is routinely used in the Matrisian laboratory for breast cancer studies. MMTV-PyVT animals develop multifocal mammary gland tumors that can affect all 10 glands with an average latency of 34 $\pm$ 6 days in females. Metastatic disease to the lung occurs in 100% of animals. A recent study has demonstrated that PyVT tumors develop through 4 distinct stages that are comparable to human disease both morphologically and by expression of biomarkers indicating that this is a very relevant model for human breast cancer [26, 27]. The Matrisian laboratory isolated and characterized a series of cell lines from a single primary tumor in an MMTV-PyVT FVB mouse. A highly aggressive PyVT antigen/E-cadherin-positive cell strain, referred to as PyVT1 [28], forms compact, rapidly growing unifocal tumors in the mammary fat pad of syngeneic FVB mice with morphologies that are consistent with the poorly differentiated component within MMTV-PyVT mammary tumors. These cells have been labeled with luciferase using a modified retroviral vector for in vivo imaging (PyVT1luc) [28]. PyVT1luc cells express MMP9 and therefore will provide an ideal mouse model of breast cancer to test the proteolytic beacon and prodrug PXL compounds discussed in Chapter 4.

Matrix Metalloproteinases

Matrix metalloproteinases (MMPs) are a family of more than 20 extracellular, zinc-dependant proteins that are capable of degrading the multiple components of

the extracellular matrix (ECM). MMPs play essential roles in many aspects of biology, including cell proliferation, differentiation, apoptosis, and migration through degradation of both matrix and non-matrix substrates. These processing enzymes have clear links to cancer and tumor progression, in which proteolysis of the ECM is required to accommodate increased growth, migration, and invasion of tumor cells. In the tumor microenvironment, host and tumor derived MMPs are often misregulated providing a promising target for *in vivo* detection of tumors. The recognition of the role of MMPs in both the growth and metastasis of tumors has guided the development not only of therapeutic strategies utilizing synthetic, small-molecule MMP inhibitors (MMPIs), but has also catalyzed methods to detect and image tumors *in vivo* by means of tumor-associated proteolytic activity. These imaging approaches target MMPs involved in cancer progression via contrast agents linked to MMP selective and specific substrates with sensitivity enhanced by amplification during enzymatic processing.

MMP Structure and Domains

The MMP family shares specific functional and structural components: the pre, pro, and catalytic domains necessary for extracellular secretion, activation of the enzyme, and enzyme activity respectively (reviewed in [29]). MMP family members are further classified on the basis of additional domains that contribute to their individual characteristics (Figure 1) [29, 30]. The majority of MMPs have additional domains such as the hemopexin region or a fibronectin-like region that are important for substrate recognition and in inhibitor binding. Another subset of

MMPs (MMPs 14 to 17), known as the membrane-associated MMPs (MT-MMPs, enumerated MT1 to MT4-MMP), contain a transmembrane domain or GPI anchor to maintain their attachment to cell surfaces.

MMPs are well regulated and are normally expressed at very low levels, if at all. However when active tissue remodeling occurs, MMPs are rapidly transcribed, secreted, and activated [31]. MMP catalytic activity is controlled extracellularly as the latent form of the enzyme requires removal of the pro-domain to become catalytically active. This process can be performed by other MMPs (eg. MT1-MMP activating proMMP2) or by other proteinases (e.g. plasmin activating proMMP3) [29]. Tissue specific inhibitors of matrix-metalloproteinases (TIMPs) further regulate MMP activity by binding with the active and inactive forms of the MMP and thus inhibit MMP activity or its activation [29]. A high level of control is necessary as MMPs are capable of cleaving not only ECM components, but also cell surface markers and other pericellular non-matrix proteins that regulate the cleavage and release of many important growth factors and cell surface substrates [31]. Therefore, with the potential to cleave such a variety of substrates, MMPs are capable of influencing diverse physiological and pathological processes, including embryonic development, tissue morphogenesis, wound repair, inflammatory disease, and cancer.

The proMMP catalytic site contains the required Zn++, chelated by three histidine residues and a cysteine from the pro domain. Removal of the cysteine and replacement with H_2O, and the presence of a compatible substrate in the active site, results in hydrolysis of the substrate between the S1 and S1' residues. MMP family members can have deep or shallow pockets in the active site, and subtle differences

in the primary amino acid sequence and secondary structure of the various MMP family members determine their substrate specificity. MMPs differ from serine and cysteine proteinases in the requirement for recognition by both P and P' sites, a feature that has precluded strategies for the generation of activity-based probes that covalently transfer a detector to the enzyme as a measure of enzymatic activity [32]. The cleavage points for MMP7, frequently finds proline (Pro) at P3, glycine (Gly) at P1, but also glutamic acid (Glu), leucine (Leu), and isoleucine (Ile) at P1' [29]. In MMP7, the other positions do not seem to be very selective. MMP9, almost always finds the P3 position occupied with Pro or alanine (Ala) and P1' richly occupied with Leu and Ile [29]. The subtle differences between the substrates cleaved by these MMPs appear in the P2' and P3' residues with Arg and Gly frequently occupying these sites for MMP9 proteins.
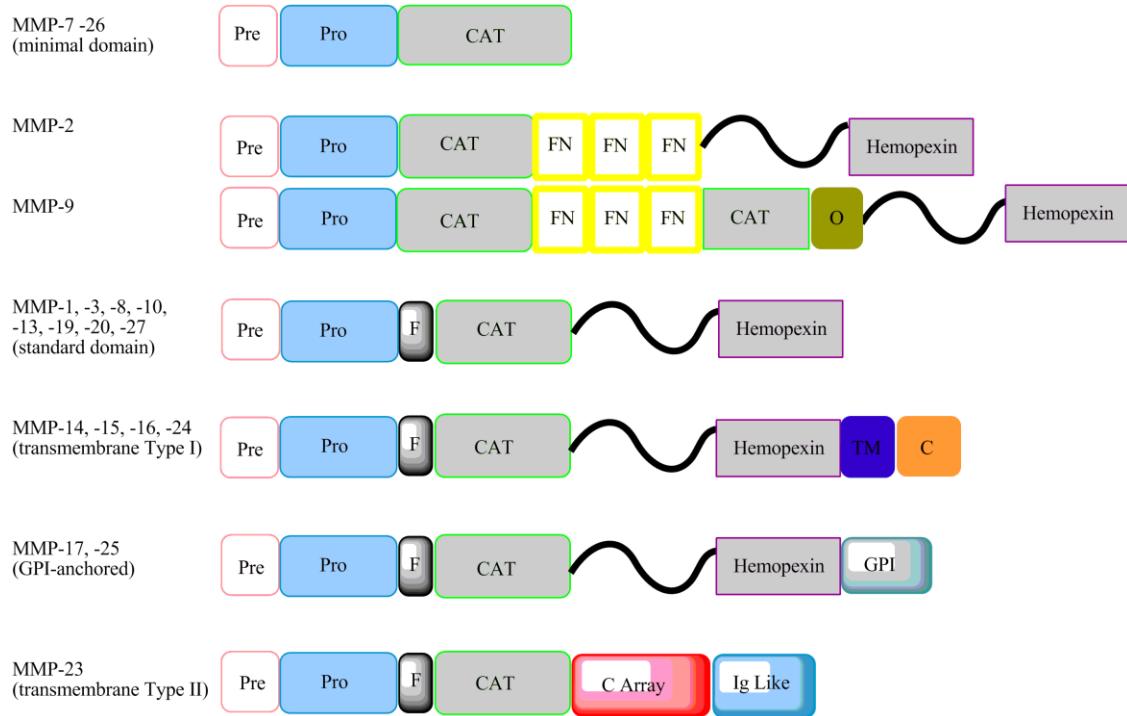
Figure 1: Domain Structures of the MMP family
Pre: pre domain; **Pro**: pro domain; **CAT**: catalytic domain; **Hemopexin**: hemopexin domain; **FN**: fibronectin domain; **~**: hinge region; **O**: O-glycosylated domain; **F**: furin cleavage site; **TM**: transmembrane domain Type I; **GPI**: GPI anchor; **C Array**: cysteine array; **Ig like**: Ig-like domain.

Tumor-associated MMP expression and activity is the result not only of tumor cell-expression of MMPs, but includes a robust contribution by the surrounding stromal cells. In fact, in epithelial cancers most of the upregulated MMPs are expressed by the host stromal cells [33]. The high level of MMPs at the tumor-stroma interface is indicative of stromal cell upregulation of MMP expression by supporting stromal cells in areas of active invasion [31]. Multiple MMPs are induced in connective tissue cells, such as fibroblasts and inflammatory cells, responding to a tumor; hence, MMPs from adjacent stromal cells facilitate invasion by the malignant epithelial cells [34]. MMPs can also be expressed by tumor cells themselves. MMP7 is commonly expressed in the epithelial component of adenocarcinomas, and several MMPs, including MMP9, are expressed in the malignant epithelium of tumors that have undergone an epithelial-to-mesenchymal transformation [34]. The multiple intestinal neoplasia (MIN) mouse model accurately recapitulates human colon tumorogenesis and expresses MMP7 in the polyps formed spontaneously in these mice. The MIN model is utilized to test a near-infrared (NIR) MMP7 beacon in this dissertation (see chapter 3).

MMP expression is generally present in higher amounts in and around malignant cancers compared to normal, benign, or premalignant tissues; and expression levels correspond to disease progression. For example, in melanomas the expression of MMP9 is associated with the conversion from radial growth phase to vertical growth phase and subsequent metastasis [35]. MMP2 is highly expressed in breast cancers, but the ratio of activated to total MMP2 levels increases as the

disease progresses to metastasis, increasing with tumor grade [36, 37]. MMPs are often associated with the removal of the ECM barrier to allow cancer cells to invade and metastasize. However, recent data indicate that MMPs do far more to influence cancer than merely remove barriers allowing metastasis. A number of MMPs are involved in cell growth, apoptosis, cell migration, tumor invasion, metastasis, and angiogenesis including MMPs 1,2,3,9, and 14 [38]. In addition, there is emerging evidence for a protective role of some MMPs in tumor progression [39]. These data support the concept that MMPs can contribute to virtually all stages of cancer from initiation through progression and metastasis to the establishment of metastatic disease at distal sites. Due to the differences in expression at diseased versus normal tissue, MMP activity provides ideal targets for the molecular imaging of cancer. Furthermore, their activity provides an attractive feature to exploit for cancer targeted prodrug therapy.

Role of MMP7 in Cancer

Of the 24 identified human MMP gene products, MMP7 is one of the smallest members of this family possessing only the domains necessary for targeting to the secretory pathway, control of latency, and catalytic activity. MMP7 is notably produced by cells of epithelial origin and contributes to tumor formation in a number of epithelial-derived adenocarcinomas [40, 41]. In addition, MMP7 is one of the few MMPs whose expression can be detected in benign intestinal tumors [42, 43]. MMP7 has been shown to be important in the progression of a number of tumors, notably those originating in the colon or in the breast [44-47]. Studies in MIN mice

indicate that MMP7 may serve as a suitable target for controlling disease progression in patients with high risk for colon cancer [48]. Wilson and colleagues demonstrated that the absence of MMP7 resulted in an approximate 60% reduction in mean tumor multiplicity in mice that were heterozygous for the APC[MIN] allele. Results also showed a significant decrease in the average tumor diameter, therefore this mouse model provides an ideal setting in which to study MMP7 activity levels. From a molecular imaging standpoint, MMP7 is a secreted extracellular proteinase that appears to be a promising target for *in vivo* detection of tumors and quantitative analysis. Thus, MMP7 provides an attractive target for developing an enhanced NIR proteolytic beacon (PB) to non-invasively assess proteolytic activity. (Refer to Chapter 3)

Role of MMP9 in cancer

MMP9 is one of two basement membrane-degrading type-IV collagenase/ gelatinases that have been classically associated with tumor invasion and metastasis [49]. MMP9 has the common motifs of the secreted members of the MMP family, and an additional fibronectin and hemopexin-like domains important for interaction with matrix protein substrates [29]. MMP9 can cleave the triple-helical native form of type-IV collagen, which is resistant to most mammalian proteinases [50]. In the studies performed in the second part of this dissertation, I have chosen to focus on MMP9 function in breast cancer metastasis. In a variety of cancers, including breast, MMP9 expression is associated with poor prognosis [reviewed in [51]]. In many cases, the majority of tumors MMPs appear to be expressed by the associated stromal cells.

14

However, MMP9 is frequently produced by tumor-associated stromal cells as well as by tumor cells themselves [reviewed in 52, 53]. Using the PyVT1-luc cell line derived from the MMTV-PyVT mouse model, MMP9 was shown to be important for the development of metastases [28]. Lung tumors in animals lacking MMP9 had a reduction in angiogenesis that was strain dependent [28]. This result is indicative of MMP9's function in the angiogenic process. MMP9 promotes angiogenesis by degrading the vascular membrane and releasing VEGF, which is a well known angiogenic molecule [54]. The matrix-interacting domains of MMP9 may serve in part to promote retention of this proteinase within the tumor-associated matrix or micro-environment following its secretion from either epithelial or stromal components of tumors. These qualities make MMP9 an ideal target to design prodrug activated therapies and imaging agents.

MMP Inhibitors: Challenges for future trials

MMPs have been associated with every step of tumor progression from initiation to metastasis, and therefore should be ideal targets for therapies to treat cancer. Despite the wealth of pre-clinical data to the contrary, trials with MMP inhibitors (MMPIs) failed; however, the interpretation of these results are heavily debated. For one, the trials failed to include surrogate endpoints to demonstrate that the MMPIs had reached and reduced the targeted MMPs' function. Patients received broad-spectrum inhibitors that led to dose limiting side-effects, mainly joint pain and inflammation, without appropriate end point measures to evaluate the efficacy of MMPIs [4]. In addition, individual MMP family members are known to

have pro- and anti- tumorigenic roles, thus proteinase activity of specific classes or individual members are needed. Carrying out further MMPI trials will require clear end point determination, as well as ways to document biologic activities such as angiogenesis or tumor proliferation using non-invasive techniques. It is also critical to determine the biologically active dose *in vivo*, which requires sensitive markers of protease activity.

MMP Substrates

The causal relationships between MMP over-expression and tumor progression drove the initial development of MMP inhibitors as cancer therapeutics. However, at the time of the initial MMPI clinical trials not much was known about the complexity of the range of proteolytic targets processed by these enzymes. Conventional methods of protease substrate identification, such as phage display and the yeast two-hybrid system have helped to identify several small peptide sequences that are selectively cleaved by specific MMPs. Innovative new strategies pioneered by Overall and colleagues, termed degradomics, take advantage of high throughput techniques such as proteomics, exosite scanning, inactive catalytic domain capture, and mass spectrometry to identify new protease substrates [55, 56]. Considering specific proteinases and their substrates as part of a system as a whole helps to identify which proteinases are responsible for processing a particular target and directs drug development against pro-tumorigenic MMPs to avoid side-effects.

Imaging MMPs

The need for highly sensitive techniques that can detect a small number of malignant cells with low levels of cancer markers on a molecular level has driven the interest in developing new approaches for tumor imaging. In addition, there is increasing interest in using molecular imaging as a means to identify patients that are likely to respond to specific treatments, and in monitoring their therapeutic response. There is a wealth of information on the expression patterns of MMPs in cancer and epidemiological evidence that supports the prognostic significance of these enzymes [51]. The advantages to using MMPs as a molecular target for an imaging agent are several-fold. These enzymes are secreted and activated in the extracellular environment, avoiding the need to transfer the probe to intracellular compartments. They are active at physiological pH, and perhaps most importantly, their activity is catalytic and thus provides an opportunity for signal amplification not found with targets that bind in a 1:1 fashion.

A variety of imaging modalities are utilized for the clinical detection and imaging of both primary tumors and metastatic disease. Utilizing MMPs as targets for *in vivo* imaging is a relatively young field of research and much has been done over the past decade to develop probes specific for MMPs. At this time, imaging MMPs has been limited to optical imaging (OIM), positron emission tomography (PET), single photon emission computed tomography (SPECT), and magnetic resonance imaging (MRI). Table 2 summarizes the strengths and weaknesses of molecular imaging modalities. A number of new probes and techniques are under development for the molecular imaging of MMPs that can be applied to give both

temporal and spatial resolution to characterize not only the progression of the disease but also have the potential to assess response to therapy.

Table 2: Relevant properties of imaging modalities utilized to image MMPs in cancer [57]

Imaging Modality	Energy Used	Spatial Resol (mm)	Temporal Resol (s)	Mol Sens (mol/l)	Tissue Penetration	Small animal or Clinical	Cost	Advantages	Disadvantages
PET	Annihilation Photons	1-4 Anim 6-10 Clin	1-300	$10^{-11} - 10^{-12}$	>300	Both	$$$$	Sensitivity versatility, targeted probes	Cyclotron required, low radiation isotopes
SPECT	Gamma Rays	0.5-5 Anim 7-15 Clin	60-20,000	$10^{-10} - 10^{-11}$	>300	Both	$$$	Multiple probes simultaneously detected	10-100 fold < sensitive than PET
MRI	Radio Frequency Waves	0.025-0.1 Anim 0.2 Clin	60-3000	$10^{-3} - 10^{-5}$	>300	Both	$$$$	Anatomical & functional imaging, high spat res.	Low sens, long acq time, poor contrast
FLI	Visible to NIR light	2-10	10-2000	$10^{-9} - 10^{-11}$	1-20	Small Animal	$	Physiological Imaging & multiple types of probes	Attenuation and autofluorescence
Ultrasound	Ultrahigh frequency Sound Waves	0.05-0.5 Anim 0.1-1 Clin	0.1-100	$< 10^{-12}$ a	1-200	Both	$	Images morphology and physiology	Limited ability to image through bone & lungs

Prodrugs are chemicals with little or no pharmacologic activity that require transformation to a therapeutically active drug [58]. The development of prodrugs is now a well established strategy to improve the physiochemical, biopharmaceutical, or pharmacokinetic properties of drug candidates to increase their usefulness in treating disease. Prodrugs provide the opportunity to overcome barriers in drug formulation and delivery that are all too common for potent compounds, such as poor solubility, chemical instability, insufficient oral absorption, rapid metabolism, inadequate brain penetration, toxicity, and drug targeting [59]. Prodrugs can be classified into the Type I and Type II categories based on their conversion site. Type I prodrugs are converted intracellularly, whereas Type II prodrugs are converted extracellularly (for review[60]). Conversion of a prodrug to its active metabolite can occur by many processes, for example, depending on changes in pH, oxygen tension, temperature, salt concentration, or by spontaneous decomposition [61]. A major approach in prodrug design is the synthesis of inert compounds that are activated by enzyme activity to release the active drug [59].

The properties that make MMP activity useful for imaging cancerous lesions make them excellent targets in directing drugs to diseased tissue. Utilizing specific MMP substrates to deliver therapies enzymatically is just one approach utilized in prodrug delivery [60]. Enzymatic prodrugs are designed to reduce the side-effects of chemotherapeutics by binding a drug to a substrate that upon conversion releases the therapy in its functional form, resulting in a higher concentrated dose of drug at the target site. While overall reducing the circulating drug and unwarranted side-

effects, enzymatic prodrugs potentially improve therapeutic effectiveness. This type of therapy has been successfully created by attaching DOX to a MMP-cleavable peptide in which the substrate is cleaved between the Gly (P1)-Leu (P1′) bond in the presence of the enzyme [62]. The prodrug form not only had a better therapeutic index, but also a greater efficacy than DOX alone. There have been a number of prodrugs developed targeting specific proteinases and utilizing different active drug metabolites. While much has been done with prodrug therapies, we believe that substrate specificity is vital to delivering active therapies in effective doses.

The structure of PXL allows derivitazation with ester, carbamate, and carbonate linkages to produce non-ionic or charged compounds. Tumor targeting moieties, sugars, polymeric chains, and enzymatically cleavable groups have been attached to the C-2′ and/or the C-7 hydroxyl groups to increase the targeting and solubility of PXL in clinical use, however these modifications have failed to improve the overall solubility and efficacy of PXL [63]. These studies demonstrate that chemical modifications to PXL are readily performed with good yields, but when successful *in vitro* translating to *in vivo* models of cancer have been unsuccessful [64]. The ability to modify PXL and retain its toxic effect was demonstrated recently when attaching PXL to PAMAM dendrimers [64]. This approach, classified as polymer directed prodrug therapy, solubilizes PXL but does not improve the targeting of the drug. The idea to make an MMP targeted prodrug PXL on a dendron to improve the selectivity of PXL and improve the solubility may improve the effectiveness of this valuable chemotherapeutic. The synthesis, characterization and testing of a new formulation of dendron prodrugs utilizing a MMP9 substrate are summarized in Chapter 4.

Nanotechnology

Nanotechnology, sometimes shortened to nanotech, refers to a field of applied science whose theme is the control of matter on an atomic and molecular scale. Nanotechnology is an extremely diverse and multidisciplinary field, ranging from novel extensions of conventional device physics, to completely new approaches based upon molecular self-assembly, all developing new materials with sizes ranging from 0.1 to hundreds of nanometers. A nanometer is one-billionth of a meter, 10^{-9} m, which is about ten times the size of the smallest atom hydrogen, and ~1/80,000 the width of a human hair. This scaling comparison reveals the opportunity to make devices in the nanoscale range and emphasizes Richard Feynman's famous statement "there is plenty of room at the bottom" [65].

Nanostructures have been used for cancer diagnosis, imaging, and therapy for many years. However, the critical feature that characterizes modern nanotechnology is the capability to design and fabricate complex structures having defined function(s) with exquisite control [66]. The capability to synthesize complex nanostructures enables the combination of functions and offers the power to colocalize medical image contrast enhancement and drug delivery. Cancer nanotechnology seeks to design molecular-size tools capable of utilizing cellular and molecular components to facilitate diagnosis and treatment. This field is relatively young, but is expected to lead to major advances in cancer therapy because of the targeting ability of nanoparticle platforms. The ability to combine several distinct functions on a single element is a characteristic that distinguishes nanotechnology from traditional chemistry approaches, and provides the opportunity to develop

cancer detection, prevention, or treatment strategies in single dose administration. The ability to target nanoparticles greatly improves the ability to detect cancerous cells with imaging agents, diagnose cancer types with selective markers, and treat tumors or metastases by selectively delivering chemotherapeutics to specific sites. Nanomaterials with multiple controllable functions are cost-effective tools that will improve the efficiency of cancer research and treatment [66]. The challenge in generating and applying multi-functional nanoparticles, however, lies in the diversity of expertise required to achieve a single particle with multiple functions. Expertise in chemistry, physics, engineering, biology, radiology, and oncology must be brought to bear on the design, synthesis and testing of these novel cancer-targeted reagents. We believe these characteristics are vital for driving the developments of new therapies in the fight against breast cancer. The future of "specialized" medicine lies with multifunctional nanoparticles and the ability to elucidate specific functions that are tailored to patients' needs.
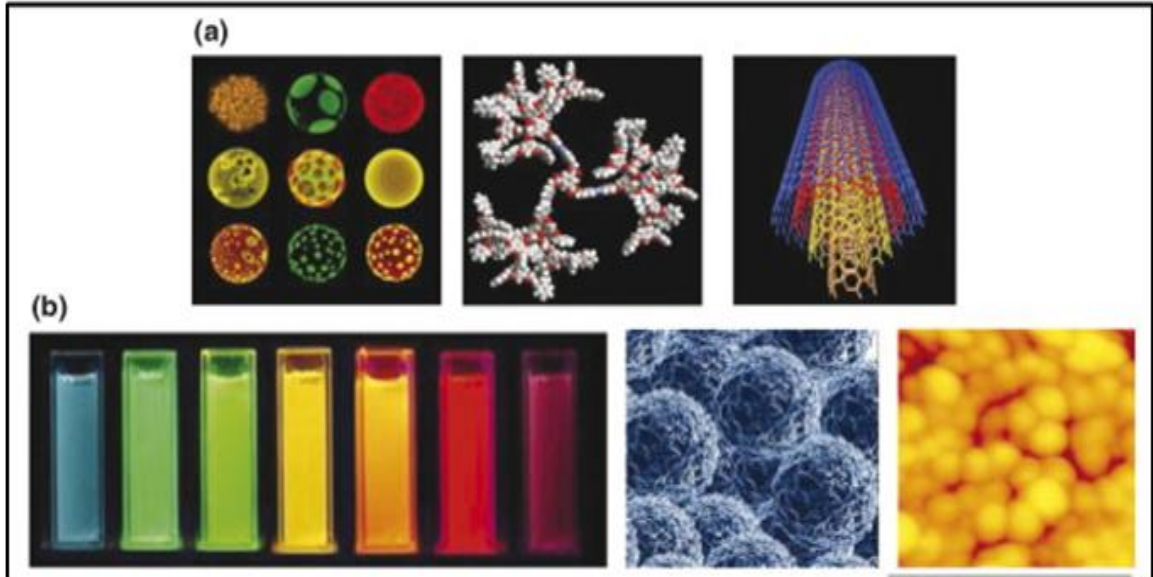
Figure 2: Current nanoparticle platforms
Organic Nanoparticles-Liposomes, Dendrimers, Carbon Nanotubes; Inorganic Nanoparticles-Quantum Dots, Magnetic FeOx Nanoparticles, Gold Nanoparticles (left to right) (a and b) (Adapted from Scherer, Boelte, Lin, in press 2010)

Nanoparticles and Platforms

Nanoparticles are prepared with organic polymers or inorganic elements and show unique physical and chemical properties depending on the specific composition and shape of the nanoparticle (Figure 1). At present, there are five distinct classes of nanoparticles: liposomes, dendrimers, carbon nanotubes, quantum dots, magnetic nanoparticles, and metallic nanoparticles [67]. Table 3 summarizes their current uses. Each class of materials has a variety of different chemical structures that lead to advantages and disadvantages. In our studies we will utilize polymer-based agents as they offer the advantages of being easily synthesized, water-soluble, nontoxic, biodegradable, conjugatable and the ability to be surface modified (i.e. pegylated).

Table 3: Current Nanoparticle Applications (adapted from Scherer, Boelte, Lin, in press 2010)

Nanoparticle	Application	Indication	Company
Liposomes	Drug delivery	Cancer	Liplasome Pharma (Lyngby, Denmark), Schering-Plough Corp (NJ, USA)
	Drug delivery	Vaccines: Influenza Hepatitis A	Berna Biotech AG (Basel, Switzerland)
	Drug delivery	Fungal infection	Enzon (Bridgewater, NJ, USA) Gilead Science (Foster City, CA, USA)
Dendrimers	Therapeutics	HIV, cancer, ophthalmology	Starpharma (Melbourne, Australia)
Carbon nanotubes	*In vitro* diagnostics	Respiratory fxn. monitoring	Nanomix (Emeryville, CA, USA)
	Imaging	Atomic-force microscopy	Carbon Nanoprobes Inc (WA, USA)
Quantum dots	*In vitro* diagnostics, imaging	Labeling reagents: Western blotting, flow cytometry, biodetection	Evident Technologies (NY, USA), Quantum Dot Corp. (CA, USA), Nanoco Technologies Ltd (Manchester, UK)
Magnetic nanoparticles	*In vitro* diagnostics	Cancer	Immunicon (PA, USA)
	Imaging, therapeutics	Liver tumors, cardiovascular disease, anemia	Advanced Magnetics (MA, USA)
	Therapeutics	Cancer	Nanospectra Biosciences Inc (TX, USA)
Gold nanoparticles	*In vitro* diagnostics	HIV	Amersham/GE (Little Chalfont, UK)
	In vitro diagnostics, imaging	Labeling reagents (PCR, RNA, Western blot), angiography & kidney	Nanoprobes Inc. (Yaphank, NY, USA)

Dendrimers

Dendrimers are well-defined highly branched synthetic polymer macromolecules with architectures consisting of a central core, an internal region, and numerous terminal groups that determine dendrimer characteristics. A dendrimer can be prepared using multiple types of chemistry that define their nanoscale spherical architecture, polydispersity, and surface functionality. Dendrimers can be synthesized by convergent and divergent methods leading to a complex array of dendritic architectures with varying solubility and biologic activity. Dendrimers, like other macromolecules, are transported into and across cells via the endocytic pathway, and therefore are excellent drug and imaging diagnostic-agent carriers through chemical modification of their multiple terminal groups [68]. For targeting tumors *in vivo*, the structural flexibility of dendrimers contributes to facilitating their escape from the "leaky" neovasculature associated with tumors and reduced lymphatic drainage called the enhanced permeability and retention (EPR) effect [69]. This is a very important aspect to take into account when designing imaging and drug delivery agents to preferentially accumulate at a target site. Thus, dendrimers present as useful vehicles for delivery of imaging reagents and therapeutics to tumors.

The first and most extensively studied dendrimers are the PAMAM™ dendrimers (Figure 2). PAMAM dendrimers are built from an ethylenediamine inner core with a divergent synthetic approach. Each iterative reaction adds a water soluble generation to the dendrimer that can be modified with various surface functionalities (amines, esters, or alcohols). PAMAM dendrimers are attractive

scaffolds for biological applications because of their tunable size, shape, biocompatibility, elimination/degradation, solubility, and minimal non-specific binding properties [69]. PAMAM dendrimers have some limitations that arise from the divergent synthetic method utilized during their production. The divergent method begins with a central core and builds towards the periphery by adding successive layers to form higher generations. The functional groups on the surface of divergent dendrimers are uniformly dispersed, which limits the control over modifications that can be made to the molecule in a selective manner [70].
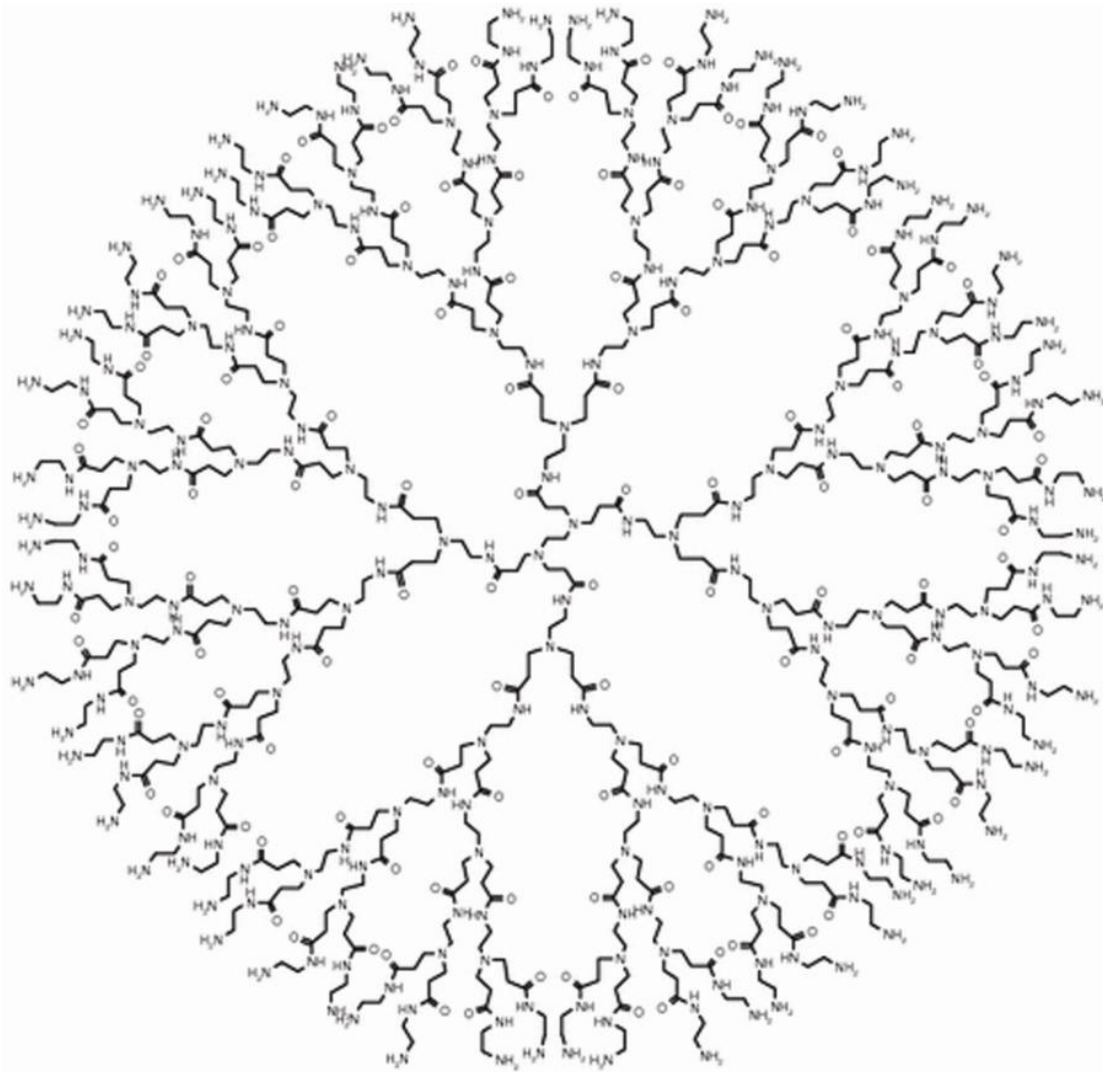
Figure 3: Generation 4 PAMAM Dendrimer

Convergent dendrimer synthesis is the preparation of dendrons of a preselected generation that are subsequently added to a central core to form a dendrimer. Such convergent dendrons are mono-disperse wedge shaped dendrimer sections with multiple terminal groups and a single reactive function at the focal point. Convergent synthesis creates homogeneous molecules by controlling the location of functional groups during synthesis that can be used to make dendrimers in a "mix and match" fashion to provide a variety of dendrimers. The "mix and match" dendrimers being developed in Chapter 4 are bis-MPA (2,2-Bis(hydroxyl-methyl)propionic acid) dendrons with alkyne, azide, or carboxylic acid focal points. Alkyne cores are suited for "click chemistry" to azides, whereas carboxylic acids can be selectively reacted with amines by using common dehydration reactions.

The Chemistry of Nanotechnology

The use of nanomaterials, in particular polymer-based materials for biomedical applications have gained enormous impact during the past decade. The novel applications have led to an increasing demand for well-defined reactions with tailorable properties. Most importantly these reactions need to be biologically inert and occur with high efficiency due to the scale for these types of reactions. Two synthetic techniques have been gaining popularity recently due to their attractive properties in biological reactions. One is "click chemistry" or the Cu (I) catalyzed 1,3-dipolar azide alkyne cycloaddition (CuAAC) and the other is oxime chemistry.

Click Chemistry

Developed by Sharpless and co-workers in 2001, click chemistry reactions have gained popularity for the synthesis of polymers with multiple architectures for biomedical and pharmaceutical applications [71]. In this reaction, an organic azide reacts with an alkyne to form a triazole ring, similar to the Huisgen cycloaddition [72]. This reaction is very selective and can be performed in the presence of multiple functional groups, which is almost a necessity when working with biological molecules. The reaction can also be performed in aqueous media with high reaction rates and good yields. The triazole moiety has also been suggested to mimic a peptide amide bond and has functioned as a dipeptide isostere in β-strands and α-helical coils [72]. A potential drawback with this reaction is the toxicity of the Cu (I) catalysts. This can be remedied with purification techniques such as HPLC or by utilizing ligands such as tris-(benzyltriazoylmethyl)amine (TBTA) that bind Cu (I) and can be removed more readily [73]. The CuAAC reaction has many forms and has been applied to synthesize block and graft polymers, dendrimers, hydrogels, nanoparticles, and many pharmaceutical and biomedical polymers. Expect to see the use of this reaction increase in popularity among biochemists in the coming years.

Oxime Ligations

The reaction rate constants of current chemoselective ligation chemistries typically range from 10^{-3} to 100 Moles^{-1} second^{-1} under ambient conditions [74]. As a result, high concentrations, a large excess of one of the reactants, or elevated

temperatures are typically used to compensate for the slow reaction kinetics. Aldehydes can be introduced fairly easily into biomolecules and are virtually inert towards reaction with other functional groups [74]. Aromatic aldehydes are potent electrophiles and are more reactive than the ketone and glyoxylyl groups typically used in imine bioconjugation reactions [75]. Aminooxyacetyl (AOA) groups are readily incorporated into biological macromolecules and chemoselectively form a hydrolytically stable oxime bond.

Since biomolecules are often present at low concentrations, their efficient labeling depends on the reaction rate of the ligation chemistry used. Aniline is a weak base that is moderately nucleophilic and does not react with the amino acid side chains of unmodified peptides, but forms a very reactive Schiff base with aldehyde containing moieties [75]. Aniline catalysis has given the reaction between aromatic aldehydes and R-effect amines a new dimension by exceeding the reaction rates of current chemoselective ligation chemistries and by bringing covalent chemistry one step closer to the rates observed in noncovalent interactions. Aniline-catalyzed imine chemistry will find wide utility in biomolecular labeling owing to its fast kinetics under mild conditions at neutral pH, providing the ideal synthetic reaction for multiple functional group chemistry utilized to make molecular imaging agents and targeted therapies.

Therapeutic and Imaging Applications of Nanoparticles

Nanoparticle platforms can be developed as vehicles to deliver anticancer drugs and imaging agents specifically to tumors. The use of nanoparticles for targeted drug delivery is likely the most exciting and clinically important application for cancer nanotechnology. Current therapies do not differentiate between cancerous and normal cells, which lead to systemic toxicity and adverse side-effects. Designing nanoparticles to deliver anticancer drugs to the targeted tumor tissue provides a platform to be able to reach desired tumor tissues, and the ability to selectively kill tumor cells without affecting normal cells. This strategy is associated with improvements in patient survival and quality of life by increasing the effective dose of drug and the reduction of systemic side-effects.

The size and surface characteristics of nanoparticles controls their ability to effectively deliver drugs and imaging agents to the targeted tumor tissue. Nanoparticles must have the ability to remain in the bloodstream for long periods of time without being eliminated from circulation by the reticuloendothelial system (RES) [76]. The size of the sinusoid in the spleen and the fenestra of the Kuffer cells in the liver varies from 150-200nm, and the size of gap junctions between endothelial cells of the leaky tumor vasculature varies from 100-600nm [76]. A major advantage of nanoparticles is the ability to tune their size to a range large enough to prevent rapid leakage into blood capillaries, and small enough to escape the RES (approximately 100nm). The capability to regulate surface groups on nanoparticles is also an important factor to improve circulation time and provide the ability to escape capture by macrophages [76]. Coating the surface of nanoparticles with

hydrophilic polymers, such as polyethylene glycol (PEG), or forming the nanoparticles from hydrophilic polymers, protects them from plasma protein adsorption and improves the solubility of hydrophobic drugs associated with the complex [76]. With over 40% of potential chemotherapeutic drugs in combinatorial screening programs being identified as poorly soluble, the ability to improve bioavailability with PEGylation may have a tremendous impact.

The ability to manipulate the size and surface characteristics of nanoparticles is leading to the development of highly specific and effective anti-cancer treatments. Passive and active targeting strategies are being utilized for nanoscale drug delivery systems. In passive targeting, the pathophysiological characteristics of the tumor vasculature and microenvironment enable nanoparticles to selectively accumulate in tumor tissues [77]. Rapidly growing cancer cells release angiogenic regulators, such as growth factors and matrix metalloproteinases, that result in highly disorganized neovascularization leading to leaky defective architecture and impaired lymphatic drainage. The mechanism by which nanoparticle accumulation occurs is called the EPR. This effect describes the ability of macromolecules, including nanoparticles, with a molecular weight above 50 kilo Daltons to selectively accumulate in the tumor interstitium [76].

The unique microenvironment surrounding rapidly growing cells also contributes to passive targeting. The high metabolic rate and resulting reduction in the supply of oxygen and other nutrients is not sufficient for hyper-proliferating cancer cells. This leads to tumor cells using glycolysis to obtain the required energy to maintain growth, resulting in an acidic environment. Liposomes that are sensitive

to pH have been designed to be stable at physiological pH~7.4 but break down and release active drug when the pH is less than physiologic values [76]. Furthermore, cancer cells release unique enzymes, such as matrix metalloproteinases, that have been associated with metastasis and cell survival mechanisms [57]. An alternative passive targeting strategy, known as tumor-activated prodrug therapy, makes use of these enzymes to deliver drugs to the tumor microenvironment by conjugating the drug to a nanoparticle with an enzyme cleavable peptide. The drugs are inactive until cleaved at the targeted site by the enzymes produced by the tumor [77]. This strategy has been used to conjugate DOX to an MMP-2 specific peptide sequence that was observed to be efficiently and specifically cleaved by MMP-2 in-vivo [76].

Drug delivery and imaging systems relying solely on passive targeting methods inevitably face limitations on specificity. These limitations are being overcome by the inclusion of active targeting agents that provide preferential accumulation of nanoparticles in the tumor-bearing organ, the tumor itself, individual cancer cells, or intracellular organelles inside the cancer cells. The ideal targeting cell surface antigen or receptor should be homogenously expressed solely on tumor cells and should not be shed into blood circulation. After selecting a viable surface marker, it is also important to choose a targeted conjugate that can be internalized upon binding. Generally internalization takes place via receptor mediated endocytosis, which may provide a means to circumvent multiple drug resistance.

Multifunctional nanoparticles

The development of novel materials and devices operating at the nanoscale range is driving major advancements in cancer imaging, diagnosis, and therapy. The combination of technology from drug delivery systems and nanoscale imaging agents is leading to the development of multifunctional "smart" nanoparticles. The ability to diagnose, treat, and assess a patient's response simultaneously with one agent could revolutionize the medical industry and personalize medicine. Multifunctional nanoparticles are just starting to emerge in scientific literature providing insight into the future of nanomedicine and the possibilities that nanotechnology is facilitating. It is conceivable that with the further advancement of nanotechnology, imaging agents, and the identification of tumor-specific biomarkers, targeted multifunctional nanoparticles will provide an effective means to detect cancer at the earliest stages, kill the tumors, and report tumor response simultaneously. Nanotechnology will help to turn the promise of personalized cancer therapy into reality in the near future.
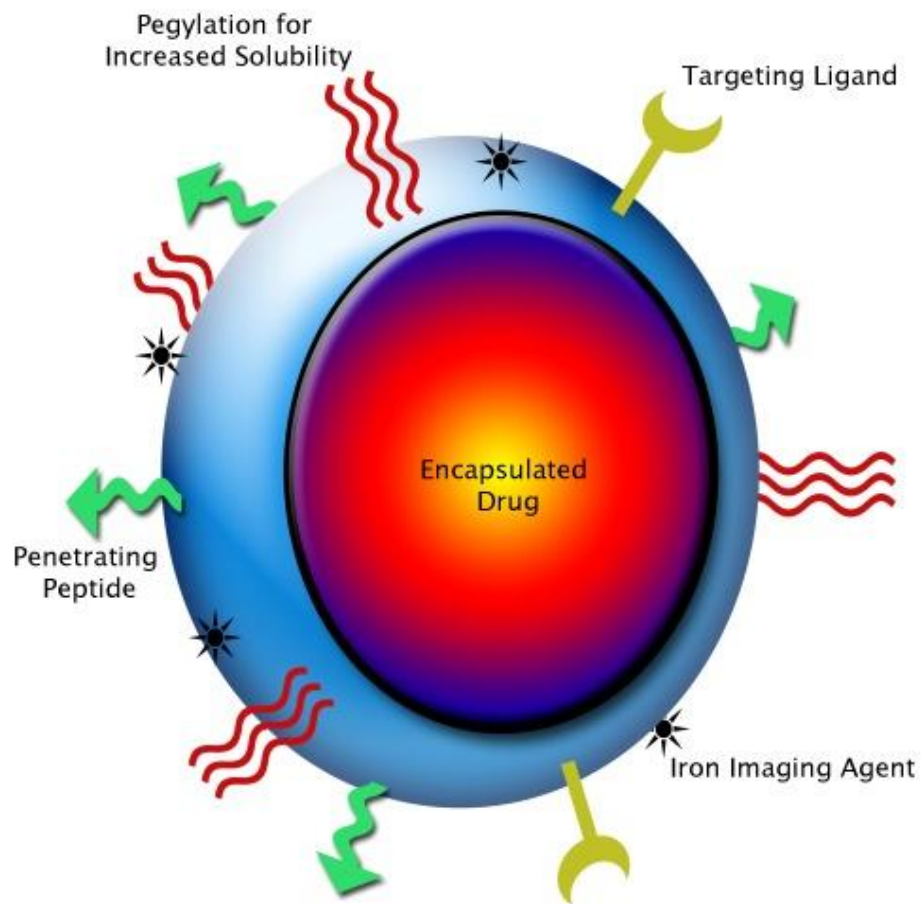
Figure 4: Possible Design for Future Multifunctional Nanoparticle (Adapted from Scherer, Boelte, Lin in press 2010)

Optical Imaging

OIM is capable of evaluating a number of *in vivo* processes with the mechanism of contrast generally requiring the accumulation of a fluorescent reagent at the target site. A multitude of fluorescently labeled probes have been developed that target cell surface receptors, enzyme biodistribution, protein function, and gene regulation [78]. The main objective of OIM is to accumulate fluorophores at a targeted region that upon excitation emit photons. OIM utilizes the ability to probe tissue with light for minimal/non-invasive detection of cancer and is practical mainly due to the development of fluorescent probes emitting in the NIR spectrum where tissue has both low absorption and reduced scattering (Figure 5) [79]. OIM plays a major role in breast cancer research and detection, despite having low resolution because of its unique ability to reveal information about the structure, physiology, and molecular characteristics in tissues.

Fluorogenically labeled substrates for MMPs have been designed that are quenched due to the proximity of the fluorophores or that utilize Förster Resonance Energy Transfer (FRET) to quench the fluorescent signal that is then enhanced upon proteolytic cleavage [80-82]. Weissleder et al. first demonstrated the in vivo optical detection and imaging of protease activity less than a decade ago in mouse xenograft tumors [83]. The optical contrast agents developed utilized NIR fluorophores as optical sensors attached to a linear poly-lysine-polyethyleneglycol copolymer. The location of the fluorophores on the polymer substrate quenched the fluorescent signal. Upon proteolytic cleavage of the poly-lysine peptide linker, fluorescent signal was enhanced producing an optically detected NIR fluorescence signal associated

with the tumor. Optimizing substrates specific for MMPs, with the same concept of off and on fluorescent signal has been utilized to develop self-quenched and FRET pair proteolytic beacons to specifically image tumor associated MMPs.

MMP2 was identified as one of the key MMPs involved in tumor invasion, metastasis, and angiogenesis, and is capable of degrading type-IV collagen, the major component of basement membranes. Bremer et al. developed the first probes capable of imaging MMP activity using reagent that was modified from the original protease-sensing probes by incorporating a peptide linker that was cleaved by MMP-2 but that could also be cleaved by other MMPs and proteinases [84]. The peptide substrate (GPLG*VRGK(FITC)C-NH$_2$, cleavage site denoted by asterisk) was labeled with Cy5 NIR fluorophores conjugated to the amino terminus with the design based on endogenous quenching of the closely positioned fluorophores. This particular probe allowed for the assessment of tumor-associated MMP activity in response to treatment with a broad spectrum MMPI, Prinomastat [85]. The development of this probe demonstrated the ability to sense and image MMP response directly *in vivo* and served as the first reporter probe to detect MMP activity.

The first MMP probes developed lacked the ability to quantitatively assess and efficiently determine specific MMP activity. To remedy this limitation, McIntyre et al. developed dendrimer-based fluorogenic substrates referred to as proteolytic beacons (PBs) to image MMP7 activity using a FRET pair as sensor and an internal reference fluorophore [80]. The internal reference attached to the probe allowed for the quantitative evaluation of both the cleaved and uncleaved substrate providing a

means to directly correlate MMP activity with fluorescent signal. The substrate utilized (Fl(AHX)RPLA*LWRS(AHX)C-COOH, asterisk denotes MMP7 cleavage site) was shown to be more selective for MMP7 than other MMPs that might also be present, particularly within the tumor microenvironment. The PB demonstrated differential response between MMP7 positive versus MMP7 negative xenograft tumors. A NIR version of this probe is investigated in Chapter 3. There is still a need for development of probes that image specific MMPs. With our knowledge of proteolysis and optical imaging, we plan to utilize this process to image delivery of therapies and correlate MMP activity with therapeutic delivery using prodrug technologies.
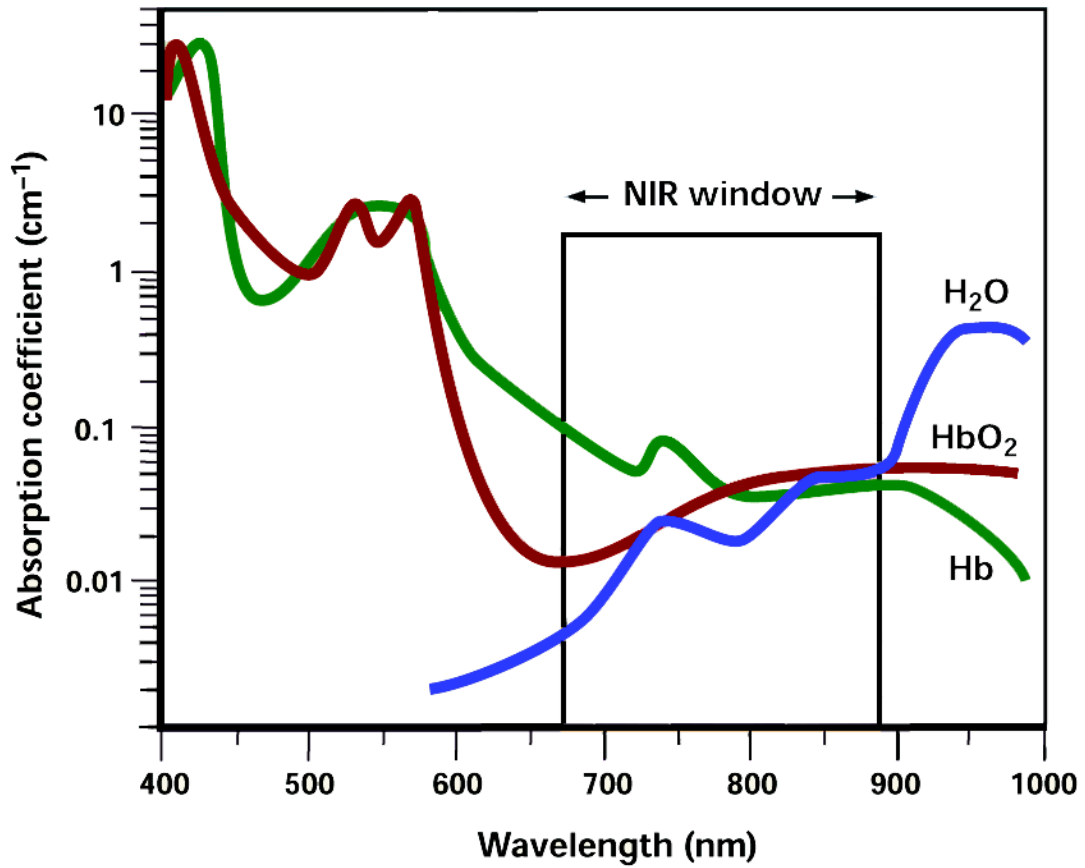
Figure 5: Near-Infrared Window:
Across this wavelength range (∼650-900nm), light absorption by physiologically abundant molecules such as hemoglobin, oxyhemoglobin, deoxyhemoglobin and, to a lesser extent, water, is reduced to a minimum. Utilizing fluorophores in the NIR increases sensitivity and depth of detection of photons traveling through tissues by reducing scattering and absorption properties [57].

Response to therapy imaging using PET

PET is a highly sensitive and quantitative molecular imaging modality, whose utility in clinical and experimental medicine is based on the assessment of radiolabeled tracer molecules. The radioactive isotope usually has a short half-life and decays by emitting a positron. When the positron interacts with a nearby electron, positron annihilation occurs and two 511keV photons are emitted in opposite directions. For *in vivo* assessment, positron emitting isotopes are produced in a cyclotron, chemically linked to a probe/tracer molecule, and injected intravenously. Since the emitted photons travel in a straight line (line of response) coincident to one another, it is possible to localize the source of the annihilation by using scintillation detectors. Hence, the fundamental physics of PET allows for the tracking of radiolabeled compounds within the body providing molecular functional imaging.

To date, many types of PET tracers for cancer imaging have been developed. For example, [18F]-2-deoxy-2-fluoro- D-glucose (FDG) is the most widely and successfully used for clinical diagnosis of cancers [86]. FDG monitors glucose metabolism and is applied in staging and diagnosis of cancer, radiotherapy treatment planning, and assessing response to therapy and prognosis. Tumor uptake of FDG tracers is considered to correlate with tumor proliferation, an important feature of tumor malignancy and will be utilized to monitor response to our prodrug therapies in Chapter 4.

<u>Combining Imaging and Therapy</u>

Two kinds of strategies have been used to combine imaging and therapy based on proteolytic activity and each has a drastically different approach. Bogyo et. al. has taken proteomics information and designed a unique class of activity-based probes (ABP) that address protein function at the level of regulation of enzyme activity [87]. These probes consist of a tag, linking agent, and a so-called "warhead" that is capable of covalently attaching to the active site of an enzyme, while the tag is used for identification and purification of modified enzymes. These particular probes are being used to monitor and profile protease activity throughout disease stages and will help to identify target proteinases for drug development. The ABP concept could also be used in robust screens for small molecule inhibitors of enzyme targets by creating a set of variable warhead molecules and testing them within large families of related enzymes. The APB probes are a great step forward in multi-functionality, but lack *in vivo* applicability.

To date the most novel probe for proteinases imaging has been developed by Tsien et. al. based on incorporating cell-penetrating peptides (CPP) labeled with either fluorosceine or Cy5 that upon cleavage by MMP2 or MMP9, penetrate or translocate into the cytosol of mammalian cells [88]. This new strategy selectively delivers molecules to tumor cells allowing for accumulation and concentration of imaging agents within cells or within the vicinity of MMP activity. The CPPs are capable of delivering attached payloads into cells without specific receptors through endocytosis. The activatable CPP concept was tested in a xenograft model using HT1080 cells showing significant uptake of the labeled peptide in cells compared to

43

a scrambled control. These activatable cell-penetrating peptides offer another means of imaging extracellular MMPs and have been hypothesized to be capable of delivering therapies.

There are a variety of probes that are capable of imaging proteolytic activity, but they have not yet related the amount of therapy or indicated therapeutic delivery *in vivo*. Most research has also been focused on *in vitro* studies or mouse models that utilize subcutaneous xenograft tumors that have been receiving much debate in their relevance to actual tumor environments. There is a clear need for probes that image therapeutic delivery and response to therapy in mouse models that are accepted as having clear significance to mimic human disease.

CHAPTER II

MATERIALS AND METHODS

This chapter is divided into two distinct materials and methods sections. Part I is based on techniques utilized for PAMAM synthesis of optical beacons, while Part II is based on methodology utilized in making "mix and match" nanodendrons.

Part I

Materials for Synthesis and Testing of PAMAM-based Beacons

All chemicals and biochemicals were reagent-grade and solutions were prepared in deionized filtered water (Milli-Q, Billerica, MA, USA). Generation 4 Starburst® PAMAM dendrimer (10% w/w in methanol), Brij® 35 solution (30% w/v) and Tricine (>98%) were obtained from Sigma-Aldridge (St. Louis, MO, USA). PEG5000 was obtained from Shearwater Polymers, Inc (Shearwater, TX, USA). SIA (N-succinimidyl iodoacetate) was obtained from Pierce Chemical (Rockford, IL, USA). M7 [(AHX)-RPLALWRS-(AHX)-C, where AHX is aminohexanoic acid], a HPLC-purified peptide that includes two AHX linkers was obtained from Open Biosystems (Huntsville, Al, USA). The N-hydroxysuccinimidyl (NHS) ester derivatives of Cy5.5 and AF750, two near-infrared fluorophores were obtained from GE Healthcare (London, United Kingdom) and Molecular Probes, Invitrogen (Carlsbad, CA, USA), respectively. MMP7 was obtained from Calbiochem (San Jose, CA, USA). Low

Fluorescent (TD-97184) and high fat chow (TD-5015) were obtained from Harlan Teklad (Madison, WI, U.S.A.)

Synthesis of PB-M7NIR

The polymer-based fluorogenic substrate PB-M7NIR was synthesized according to the procedure outlined in Figure 6.

Labeling M7Peptide with Cy5.5

The Cy5.5-labeled peptide, Cy5.5-M7, was designed for selective cleavage by MMP7 to yield a relatively insoluble fluorescent labeled N-terminal fragment that includes an AHX linker (Scheme 1). In the first step of synthesis, a methanolic solution (5mM) of the M7 peptide was reacted with 0.8 equivalents (eq) of Cy5.5-NHS in DMSO (7 mM) and triethylamine added to 1% (v/v) to fluorescently label the peptide at the N-terminal amine. After overnight reaction at ambient temperature, residual NH_2 groups were blocked using NHS-acetate (20 mg/ml in 2.5 eq/peptide) for 1 hr followed by glycine (2M in H_2O at 2eq/acetate) to quench residual NHS-acetate. Dithiothreitol (2 mg/ml in methanol, 0.15 eq) was then added to the reaction mixture to reduce the sulfhydryl groups on the C-terminal cysteine of Cy5.5-M7.

Coupling Cy5-M7 to G4-PAMAM-PEG

G4-PAMAM-PEG was prepared by reacting an aliquot of the PAMAM stock solution (in methanol) with an equimolar equivalent of NHS-PEG5000 (dissolved at 22 mM in methanol). To synthesize the thioether-bonded conjugate (Cy5.5-M7)$_m$-PAMAM-

PEG5000, the PAMAM-PEG conjugate was first activated by treatment with SIA (8 mg/ml methanol, 20 eq/PAMAM). After reaction for 20min at ambient temperature, the SIA activated PAMAM-PEG was immediately reacted with the reduced Cy5.5-M7 peptide in methanolic solution (8 peptides/PAMAM) and allowed to react at ambient temperature (24 hr in the dark) with gentle mixing. The reaction mixture was then diluted 10-fold with aqueous 0.1 mM EDTA (pH 8, previously treated with 1mM phenylmethylsulfonylfluoride) and then concentrated and purified by at least three rounds of diafiltration (CentriPrep YM-10, Millipore) followed by concentration. The fraction of Cy5.5-M7 incorporated into the peptide-PAMAM-PEG5000 co-polymer (>95%) was calculated from the relative Cy5.5 concentration in the reaction mixture versus effluents. The product $(Cy5.5-M7)_8$-PAMAM-PEG5000 (~90% based on the ninhydrin assay) was stored (4^oC) at approximately 1 mg PAMAM/ml overnight and subsequently labeled with AF750 as described below.

Coupling of AF750 to $(Cy5-M7)_8$-PAMAM-PEG5000

To label the PAMAM scaffold of $(Cy5.5-M7)_8$-PAMAM-PEG5000 with AF750, the peptide-PAMAM co-polymer was made 50 mM in Na_2CO_3 (pH 9) and reacted with up to eight equivalents of AF750-NHS (7mM in DMSO). After overnight incubation at ambient temperature ($22-24^oC$ in the dark), the reaction mixture was diluted 10-fold with aqueous 0.1 mM EDTA (pH 8) and the product $(Cy5.5-M7)_8$-PAMAM-$(PEG5000)(AF750)_n$ was separated from unincorporated AF750 by diafiltration (as above) using a total of 4 washes with the same buffer. Incorporation of AF750 was calculated from absorbance at 750nm with a concentration determined to be 6

AF750/PAMAM. The final product $(Cy5.5-M7)_8$-PAMAM-$(PEG5000)(AF750)_6$, now referred to as PB-M7NIR, was stored in the dark at 4^oC in 0.1 mM EDTA (pH 8) until administration after dilution into sterile saline.

Fluorescence spectroscopy

Fluorescence excitation and emission spectra of PB-M7NIR, diluted with deionized water (0.05–0.1 µM) to obtain an absorbance of <0.05, were measured in 4 mm x 4 mm quartz cuvettes at 25^oC using an L-format Quanta Master QM-9 photon counting fluorimeter (1 nm steps, 2 nm slits) operated with Felix software (Photon Technology International, Lawrenceville, NJ, U.S.A.). Fluorescence spectra of PB-M7NIR and subsequent controls were recorded before and after treatment with MMP7and are illustrated with the same amplitude after cleavage to account for differences in the fluorescence concentration of each sample.

Cell Culture

SW480 human colon cancer cells were obtained from A.T.C.C. (Manassas, VA, U.S.A.). Stable clones expressing the neomycin selection cassette (SW480neo) or neomycin and MMP7 (SW480mat) were isolated and characterized as reported previously[89]. Cells were maintained in Dulbecco's modified Eagles's medium containing 10% (v/v) fetal calf serum at 37^oC in a 5% CO_2 environment.

In vivo Imaging of xenograft model

SW480neo control and MMP7-expressing SW480mat colon cancer cells ($1x10^6$ cells) were seeded on the flanks of athymic nude mice (n=13) (Harlan, Indianapolis, IN, U.S.A.). Tumors of approximately 5-10 mm in size developed after 3-4 weeks of growth. Mice were placed on a low-fluorescent diet one week post injection of cells to reduce autofluorescence particularly from the intestinal region. After 4 weeks of tumor growth, mice were anesthetized using 2% isofluorane and imaged using a cryogenically cooled CCD camera, IVIS 200 Imaging System by Xenogen (Alameda, CA, USA), in the Cy5.5 (Sensor-Cy5.5) and ICG (Reference-AF750) channels. PB-M7NIR (1.0 nmol in 100ul of sterile 0.9% saline) was retro-orbitally injected and animals were imaged for up to 30min post injection. Additional image sets of animals were recorded every hour for up to 4 hrs post injection of PB-M7NIR. *In vivo* results were from thirteen animals, each bearing control and MMP7-expressing xenograft tumors with *ex vivo* data from tumors removed from four of the same animals. All animal experiments were in accord with IACUC regulations. The imaging data sets were analyzed using Living Image® software by Xenogen in the Cy5.5 and ICG channels that predominately measure Cy5.5 (sensor) and AF750 (reference) fluorescence respectively. Regions of interest were created to measure the average radiance (photons/sec/cm^2/steradian) both pre and post injection of PB-M7NIR in the tumor bearing regions and in the hind leg of the mouse (muscle tissue) for use as normal tissue control. Sensor and reference signal is measured either as signal above pre-injection background and/or signal minus background post-injection as indicated.

49

Ex-vivo Imaging of intestinal adenomas

Four congenic C57Bl/6-Min (Min/+) mice positive for the Apc[Min] allele (Jackson Laboratory, Bar Harbor, ME, USA), three congenic C57Bl/6-Min-MMP7-null mice [90], and four C57Bl/6 normal control mice (Jackson Laboratory, Bar Harbor ME, USA) were placed on a high fat diet 5015 (Harlan Teklad) for fifteen weeks and then on low fluorescent chow (TD-97184, Harlan Teklad) for two weeks to reduce tissue autofluorescence. Mice were anesthetized using 2% isofluorane and retro-orbitally injected with PB-M7NIR (1.0nmol in 100ul sterile saline 0.9%). Approximately 1 hr post injection, animals were sacrificed using CO_2 asphyxiation at which point their small intestine (duodenum, jejunum, ileum), cecum, and colon were removed, rinsed with ice-cold 1X phosphate buffer saline (50 ml), and opened longitudinally to reveal adenomas on the luminal surface. Images were taken in the Cy5.5 (Cy5.5-sensor) and ICG (AF750-reference) channels using a cryogenically cooled CCD camera (IVIS 200 Imaging System, Xenogen, Alameda, CA, U.S.A.) to examine fluorescence signal from MMP7 cleavage. The tumor and non-tumor image data sets were analyzed using Living Image software by Xenogen to measure fluorescence intensities in regions of interest. Signal was recorded as average radiance (photons/second/cm^2/steradian) for both channels and calculated as signal minus background intensity.

Histological Imaging of Proteolytic Activity

Xenograft tumors or intestinal adenomas were each resected, placed in optimal cutting temperature (OCT) embedding media, snap frozen in liquid nitrogen, and

stored at -20^0C until sectioned (5-10mm) using a cryomicrotome. For histological analysis, OCT was removed from the samples by immersing the slides in H_2O followed by 70% EtOH. Slides were aqueously mounted (Biomeda, Foster City, CA, USA) in media containing 4',6-diamidino-2-phenylindole (DAPI, 2μM). Quantitative fluorescence imaging was done by taking digital pictures with full-frame, black and white CCD camera (MicroMax 1317-K1; Princeton Instruments, Trenton, NJ, U.S.A.) coupled to a fluorescence microscope with a variety (10X, 20X, and 40X-oil immersion) of Plan-Neofluar objective lenses (Axiophot; Carl Zeiss, Thornwood, NY, U.S.A.). Camera control, image acquisition and analyses were performed using Metamorph imaging software (Universal Imaging, Downingtown, PA, U.S.A.). Fluorescence signal was linear with camera exposure time, and the exposure conditions were optimized for maximum dynamic range. White light and DAPI images were used to focus and orient the specimen field before fluorescence excitation. At least two images were then acquired for optimal excitation. Light was collected using the 40X objective lens under oil immersion. Fluorescence *sensor* signal (Peak Emission 694 nm) was discriminated using a Cy5.5 near infrared band-pass filter set (Chroma Technology Corp., Brattleboro, VT, U.S.A.) from *reference* fluorescence signal (Peak Emission-776 nm) using a Cy7 band-pass filter set (Chroma Technology Corp., Brattleboro, VT, U.S.A.). The intensity in each channel was calculated as the average counts/pixel after subtraction of background signals from control samples (non-tumor bearing C57Bl/6 intestine).

<u>Immunohistochemistry</u>

Spontaneously occurring intestinal polyps were harvested from *Min/+* and *Min*-7-null mice, along with normal intestinal tissue harvested from C57Bl6 normal mice, frozen in OCT, and used to generate 5-μm sagital sections. Sections were rinsed in a series of graded alcohols to remove the OCT, rehydrated, incubated in 0.6% hydrogen peroxide for 30 minutes to remove endogenous peroxidase activity, and heated to 95°C for 3.5 minutes in 10 mM citrate buffer, pH 6.0, to reveal antigenic epitopes. Blocking was performed by incubating for 1 hour at room temperature in a solution containing 5% goat serum, 1% bovine serum albumin, 0.5% Tween-20 and 0.1 M MgCl2 in 10 mM Tris-HCl, pH 7.4. Sections were then incubated with a rat monoclonal antibody raised against MMP7 [91] diluted 1:100 in blocking solution overnight at 4°C. The slides were washed three times in TBS containing 0.05% Tween-20 before incubating for 1 hour at room temperature with biotinylated rabbit anti-rat IgG (Vector Laboratories, Burlingame, CA) diluted 1:1000. After another series of washes in TBS containing 0.05% Tween-20, the sections were processed using the Vectastain Elite ABC kit (Vector) according to the manufacturer's instructions. Positive signal was detected using diaminobenzidine (Sigma, St. Louis, MO) as a chromogen and the sections were counterstained with Mayer's hematoxylin (Sigma).

<u>Statistical Analysis</u>

All data generated using PB-M7NIR *ex vivo* imaging assays were analyzed with a one-way ANOVA (Newman-Keuls Multiple Comparison Test) method for three

sample sections or for two sample sets using a nonparametrical (Mann-Whitney) method. Data generated using the xenograft and Min models were analyzed using a nonparametrical (Mann-Whitney) method (Graph Pad Software, San Diego, CA, USA).

Part II

Materials for Synthesis and Testing of "Mix and Match" Nanodendrons

All materials were reagent grade or HPLC grade quality and solutions were prepared in deionized filtered water (Milli-Q, Billerica, MA, USA). Peptide Sequences were purchased from New England Peptide LLC (Gardner, MA, USA) and D-AA acid peptides from Biomer Technology (Pleasanton, CA, USA). The N-hydroxysuccinimidyl (NHS) ester derivative of AF700 and the maleimide derivative of AF750, two near-infrared fluorophores were obtained from Molecular Probes, Invitrogen (Carlsbad, CA, USA). MMP9 was obtained from Calbiochem (San Jose, CA, USA). Low Fluorescent (TD-97184) chow was obtained from Harlan Teklad (Madison, WI, U.S.A.). G3 azide and alkyne core dendrons (D) were purchased from Sigma Aldrich and made by Polymer Factory (Nacka, Sweden). Size Exclusion BioBasic 120 and 300 columns were purchased from Thermo Fisher Scientific Inc. (Waltham, MA, USA). Analytical and Preparatory C18 Polaris columns were purchased from Varian Inc. (Palo Alto, CA, USA) All other reagents and chemicals were purchased from Fischer Scientific or Aldrich companies and used as specified.

Aldehyde Dendron Synthesis

G2 dendrons (8, 2-(benzyloxycarbonyl)-2-methylpropane-1,3-diyl bis(3-hydroxy-2-(hydroxymethyl)-2-methylpropanoate) reported by Hult et. al.[174], were prepared by Lynn Samuelson and obtained from the Bornhop lab (compound 1). Both G2 and G3 dendrons were modified by adding formyl benzoic adic to the free hydroxyl

surface groups using DCC and DMAP as coupling agents (compounds 2, 7, 11). These reactions work best in methylene chloride, however the solubility of the acid requires 1:1 tetrahydrofuran (THF): methylene chloride (DCM) for this reaction. Dendron (either G2 or G3) is dissolved in 1:1 THF/DCM with 1.2 eq per hydroxyl group of formyl benzoic acid. Next 1.5 eq per hydroxyl DCC or DIC (both work well with similar yields) is added to the flask. The reaction is allowed to stir for 3 days and concentrated under vacuum. The crude product was separated using the Biotage SP1® system with silica gel using an ethyl acetate/hexanes gradient to give ~40% yield G2 dendron-aldehyde$_4$ and 77% G3 dendron-aldehyde$_8$. Example reaction conditions (using 56.3 mg [6.479×10^{-5}] moles G3 alkyne dendron, requires 93.3mg formyl benzoic acid [6.21×10^{-4} moles] and 160mg DCC [7.77×10^{-4} moles] with 10 molar% DMAP 6.3 mg; yields 95.4mg ND$_3$ dendron with 8 aldehyde groups attached.

Dendron Peptide Oxime Ligation

The typical reaction requires 4 peptides per dendron G2 and G3. Dendron is dissolved to 50 mg/ml in DMSO and Analine is added (100mM final concentration) and stirred for 5 minutes. Peptide H2N-AHX-AVRWLLTA-AHX-(w or w/o C)-AHX-(DprAOA)-NH2 (10-20 mgs) is dissolved in acetate buffer 0.05M NaAc/HOAc buffer at pH 4.5. The peptide is then added to the DMSO dendron aniline solution and allowed to stir overnight. Typical reaction conditions were 10mgs peptide in 500μl acetate buffer added to 200μl of G2 dendron aldehyde (or 200μl of G3 dendron aldehyde) with 9μl Aniline in DMSO. The reaction is monitored with Size Exclusion

(SEC) High Performance Liquid Chromatography (HPLC) at 280nm to monitor the tryptophan in the peptide chain and 254nm to monitor the benzene groups of the dendron aldehyde compound (Conditions: Static: 55% H_2O 0.05% TFA-45% Acetonitrile 0.065%TFA). The product is then purified using C18 reverse phase Prep HPLC using gradient elution (95% H_2O 0.05% TFA: 5% Acetonitrile 0.065% TFA to 5% H_2O over 26 minutes) to obtain Dendron-(Peptide-NH2)$_4$ (Compounds 3, 8, 12) with typical yields ranging from 85-95%.

Proteolytic Beacon Synthesis ND^{PB}

H2N-AHX-AVRWLLTA-AXH-C-Dendron (Compound 3, 12) is dissolved in 250μl anhydrous DMF in a 1.5ml amber vial. AF750 Maleimide (1mg) is then dissolved in 250 μl anhydrous DMF and added drop-wise to dendron peptide over 30 minutes. This reaction is allowed to stir for 4 hours at which time AF700-NHS ester (1mg) is dissolved in 250μl DMF and added to the reaction mixture. The reaction vial is shaken over night and purified by using preparatory C18 RP-HPLC to give product with an average of 4 AF700 and 4 AF750 dyes attached to each dendron via absorbance spectra ND^{PB} & ND$_3$^{PB} (Compounds 4, 13). C18 HPLC Conditions: H_2O 0.01% TEA (A), Acetonitrile 0.01% TEA (B), starting conditions 95%-A using gradient over 25 minutes to 95% B, 95% B to 100% B over 5 minutes, 100% B for 10 minutes.

The stock solution of ND^{PB} was diluted into 1ml of Tricine buffer with 50μl 0.2mM EDTA to give approximate concentration of 164μM ND^{PB}. 182μl of Stock Solution was diluted to 30nMoles in Tricine Buffer. 10μl of this sample was added to 80μl buffer and 10μl of MMP 9 diluted 25 X. Triplicate samples were prepared and stored at 37 degrees C overnight to digest. Samples of ND^{PB}-DAA, and ND^{PB} with EDTA to inhibit MMP function were prepared. Matrigel™ (phenol red free) was diluted in sterile phosphate buffer as indicated by manufacturer, and aliquots of 225μl stored at -20 degrees C. Matrigel™ was kept on ice at all times during this experiment. After overnight incubation, ND^{PB}, ND^{PB}-DAA, ND^{PB}/EDTA was added to Matrigel™ for desired concentrations (i.e. 3μM, 1μM, .3μM, .1μM, 0.03μM-for example, for 10X dilution of stock into Matrigel™ add 25ul sample to 225ul Matrigel™ to give 3uM concentration). Syringes were kept on ice during this procedure to minimize Matrigel™ solidification during injection. 100μl of matrigel with ND^{PB} was injected subcutaneously into the mouse after anestisizing with 2% isofluorane. Images were taken with the LI-COR PEARL® imaging system in the visible, 700, and 800 channels.

In vivo Imaging using ND^{PB} Xenograft Model

Lewis Lung Carcinoma Cells (LLC) were modified previously in the Matrisian laboratory to express high levels of recombinant MMP9 [92]. These cells were modified from LLC cells by incorporating an empty vector (LLC-RSV) and an MMP9 vector (LLC-MMP9) into the cells. The LLC-RSV (referred to as LLC-MMP9 (-)) and

LLC-MMP9 (+) have undetectable and high levels of MMP9 respectively. LLC-MMP9 (-) and LLC-MMP9 cells ($5.0x10^5$ cells) were seeded on the flanks of athymic nude mice (n=8) (Harlan, Indianapolis, IN, U.S.A.). Tumors of approximately 5-10 mm in size developed after 1-2 weeks of growth. Mice were placed on a low-fluorescent diet one-week pre-injection of cells to reduce autofluorescence particularly from the intestinal region and fat pads. After 1-2 weeks of tumor growth, mice were anesthetized using 2% isofluorane and imaged using the LI-COR PEARL® Imaging System in the 700 (Sensor-AF700) and 800 (Reference-AF750) channels. ND[PB] (3.0 nmol in 100ul of sterile 0.9% saline) was injected retro-orbitally and animals were imaged for up to 30min post injection. Additional image sets of animals were recorded every hour for up to 6 hrs post injection of ND[PB]. *In vivo* results were from eight animals, each bearing control and MMP9-expressing xenograft tumors. All animal experiments were in accord with IACUC regulations. The imaging data sets were analyzed using LI-COR PEARL® software in the 700 and 800 channels that predominately measure AF700 (sensor) and AF750 (reference) fluorescence respectively. Regions of interest were created to measure the average counts/sec both pre and post injection of ND[PB] in the tumor bearing regions and in the hind leg of the mouse (muscle tissue) for use as normal tissue control. Sensor and reference signal is measured either as signal above pre-injection background and/or signal minus background post-injection as indicated.

In vivo Imaging of PyVT1-luc Mammary Tumors

FVB-wild type (FVB-WT) mice obtained from Jackson laboratories were used in these studies. Mice were anestesized with 2% isofluorane and a tiny incision was made just to the right of mammary gland two. PyVT1-luc cells (1.0×10^6 cells) were injected into the mammary tissue in 20 μl sterile PBS solution. The incision was closed with a wound clip which stayed in for up to four days before removal. The PyVT1-luc cells are tagged to express luciferase and were monitored with the IVIS imaging system (Caliper Life Sciences) to quantitate luminescence starting 2 days post injection, and every 4 days thereafter. Firefly luciferin (120mg/kg in sterile PBS, Gold Biotechnology Inc.) was injected intraperitoneally 10 minutes prior to imaging. Living Image Software (Caliper Life Sciences) was used to quantify luminescence in the tumor bearing mammary gland over time. After 1-2 weeks of tumor growth, mice were anesthetized using 2% isofluorane and imaged using the LICOR PEARL Imaging System, in the 700 (Sensor-AF700) and 800 (Reference-AF750) channels. ND^{PB} (1.0 nmol in 100ul of sterile 0.9% saline) was retro-orbitally injected and animals were imaged for up to 30min post injection. Additional image sets of animals were recorded every hour for up to 6 hrs post injection of ND^{PB}. For GM6001 and D-amino acid ND^{PB} studies, 5 mice were selected from the cohort and imaged with ND^{PB}. These five mice were then treated with GM6001 for three days and on the third day administered with ND^{PB} (1.0nmol in 100 ul of sterile 0.9% saline) and imaged as described above. For DAA studies, mice were treated with

ND[PB]-DAA (1.0nmol in 100ul sterile 0.9% saline) and imaged as described above for

ND[PB].

PXL-COOH Synthesis

This compound was made essentially as described in Mojoros et al [24]. PXL (77.61

mg, 0.091 mmols) was dissolved in methylene chloride (6 mL). Succinic anhydride

(13.1 mg, 0.131 mmols) in 0.8 mL of methylene chloride was added followed by

pyridine (27 µl). The reaction was stirred for 4 days. TLC (1:1 hexanes: ethyl acetate

on silica gel) indicated 4 spots under a UV lamp and with potassium permanganate

staining. Staining with bromo-cresol green indicated that the carboxylic acid was the

last spot. The reaction was concentrated onto silica gel and purified with the

Biotage™ SP1 system using a hexane/ethylacetate gradient followed by flushing

with methanol to elute the product. After concentration the last peak eluted was

77.6 mg (89.3%) of desired product as confirmed by MS. MS (ESI)+ Found: 954.30

Dalton; calculated: 954.99 Dalton.

PXL-NHS Ester Synthesis

The procedure for synthesis of PXL-NHS ester was followed as described in [24]. A

volume of 15 µL (4.3 equiv) of triethylamine was added to a solution of 27.2 mg of

PXL-hemisuccinate and 1.5 mol equiv of SDPP in 1.5 mL of acetonitrile. The reaction

was stirred for 6 h at room temperature, than concentrated under vacuum. The

residue was dissolved in 2.5 mL of ethyl acetate and 1 mL of hexane and purified on

silica gel. The purified PXL-NHS ester was dried for 24 h in vacuum at room temperature to give 29.4 mg (98.0%).

PXL-Peptide-Dendron (ND^Pxl) Synthesis

PXL-COOH Method

This procedure is based on and follows that described by Lynn Samuleson (Ph.D thesis). All glassware used in the reaction was flame dried and cooled in a desiccator prior to use. The solvents were anhydrous and all solid materials were dried under vacuum for more than 3 hours prior to use and exposed to anhydrous Ar(g) gas upon breaking the vacuum seal. Example reaction conditions: First, PXL-COOH (8.51 mg, 0.0091 mmols) was dissolved in 0.5 mL DMF. Next, EDCI (5.00 mg, 0.026 mmols) and BOP (5 mg, 0.011 mmols) were added to the PXL-COOH solution followed by DIEA (180 μl). The reaction was stirred for 30 minutes prior to adding H2N-[Ahx]-AVRWLLTA-[Ahx]-Dendron (3.56 mg, 0.00068 mmols Compound 3, 8), dissolved in 0.5 mL DMF. The reaction was stirred under Ar(g) overnight with SEC spectra taken 5 minutes after H2N-[Ahx]-AVRWLLTA-[Ahx]-Dendron addition and after 24 hours. A notable change in the elution time of the first peak indicated coupling occurred. The reaction was concentrated under vacuum, and dissolved in DMSO. The product was purified first by using Amicon Centrifugation Diafiltration tubes (3,000 MWCO) to concentrate the high molecular weight compounds followed by three washings with DMSO to remove the low molecular weight compounds. The remaining high molecular weight compounds were separated using C18 RP-HPLC (95% H_2O 0.05% TFA: 5% Acetonitrile 0.065% TFA to 95% Acetonitrile 0.065%

TFA over 26 minutes) to yield 3.79 mg (55.6%) of pure (PXL-[Ahx]-AVRWLLTA-[Ahx])4-Dendron (Compound 5, 9).

PXL-NHS Ester Method

This method was only utilized on the last batch of $ND_3{}^{Pxl}$ synthesis. All glassware used in the reaction was flame dried and cooled in a desiccator prior to use. The solvents were anhydrous and all solid materials were dried under vacuum for more than 3 hours prior to use and exposed to anhydrous Ar(g) gas upon breaking the vacuum seal. H2N-AHX-AVRWLLTA-AHX-(w or w/o C)-Dendron (10.69mg, 1.49μmoles) was dissolved in DMF followed by addition of PXL-NHS ester (1.2eq, 5.7mg) in DMF. The reaction was stirred overnight and then purified using C18 RP-HPLC to give 12.9mgs (78.7% Yield of compound 9). This reaction has a superior yield as compared with the PXL-COOH method above and should be utilized for future coupling procedures.

ND^{Pxl} Studies

PXL concentration was determined by UV-VIS analysis at 229nm and by quantitative HPLC methods. ND^{Pxl} is dissolved in DMSO to the desired concentration and diluted into sterile saline for retro-orbital injection. Fifty mice were injected with PyVT1-luc mammary tumors ($1.0x10^6$ cells) in the mammary fat pad. After 1 week of growth, mice were dosed with ND^{Pxl} every 2 days for six doses at 12.5mg/kg and 4.16mg/kg. Abraxane was administered at 25mg/kg every 4 days to provide a dose of PXL equal to the total dosing with ND^{Pxl}. Control mice were injected with either 40%

DMSO/sterile saline or 100% sterile saline; DMSO treated controls had no significant difference than the saline-treated controls. Tumor volumes were recorded with calipers, monitored with bioluminescence, and FDG-PET.

$ND_3{}^{Pxl}ND_3{}^{PB}$ Click Reaction

$ND_3{}^{Pxl}$-azide (Compound 9) and $ND_3{}^{PB}$-alykyne (Compound 13) were linked together using CuAAC reaction conditions [73, 93]. $ND_3{}^{Pxl}$ and $ND_3{}^{PB}$ were dissolved and mixed in 200μl DMF at 1.2 equivalents $ND_3{}^{PB}$ alkyne to $ND_3{}^{PXl}$ azide derivates. Water (10μl) was added until the solution became opaque. At this point, 0.1 mole % Tetrakis-(acetonitrile)copper(I) hexafluorophosphate (Cu (I) source) and tris[(1-benzyl-1H-1,2,3-triazol-4-yl)methyl]amine (TBTA) were added in 1:1 acetonitrile:DMF. The reaction was monitored by C18 RP-HPLC and was complete after 24hrs time to give 1:1 linking of $ND_3{}^{Pxl}ND_3{}^{PB}$ (Compound 14). C18 conditions: H_2O 0.01% TEA (A), Acetonitrile 0.01% TEA (B), starting conditions 95%-A using gradient over 25 minutes to 95% B, 95% B to 100%B over 5 minutes, 100% B for 10 minutes. PXL concentration as well as AF700/750 concentration was monitored with quantitative HPLC and UV-VIS analysis.

$ND_3{}^{Pxl}D$ Mammary Tumor Toxicity Studies

$ND_3{}^{Pxl}$-azide (Compound 9) was first clicked together with G3 alkyne dendron (Compound 10) with non functionalized hydroxyl surface groups to improve solubility of the construct. 1.2 equivalents of the G3 alkyne dendron was dissolved into 200μl DMF with 1 equivalent of $ND_3{}^{Pxl}$. dH2O (10μl) was added until the sample

turned cloudy white. At this point 0.1 mole % TBTA and 0.1 mole % Tetrakis-(acetonitrile)copper(I) hexafluorophosphate (Cu (I) source) were added. The reaction was shaken overnight and then purified using C18 RP-HPLC to give the final product (Compound 15). PXL concentration was determined by using quantitative HPLC and UV-VIS analysis at 229nm. Thirty mice were injected with PyVT1-luc cells in the mammary fat pad and after 1 week of growth treatment studies began. ND$_3^{PXL}$D was administered intraperitoneally (I.P.) in sterile saline with 30% DMSO at concentrations of 25mg/kg every day, 12.5mg/kg, and 4.16 mg/kg every two days for 12 days. Abraxane mice were treated at 12.5 mg/kg and 4.16 mg/kg every two days for 12 days I.P. Control mice were injected with sterile saline and 30% DMSO. In this study, the first dose of all compounds was given by retro-orbital injection and resulted in death of 2/5 animals attributed to embolism. Thereafter reagents were administered I.P with no further side-effects. Tumor volume was monitored with calipers, bioluminescence, and FDG-PET.

<u>Neurobehavioral Mouse Screen</u>

A subset of tests from the Irwin Neurological Screen was used to evaluate gross neurological function. The screen was performed on each mouse in all treatment groups prior to beginning ND$_3^{Pxl}$ studies, 1 week into treatment, and after the completion of the study. Body weight, coat color, presence of whiskers, appearance of fur, trunk curl, reaching reflex, body tone, Pinna reflex, Preyer reflex, toe pinch, limb tone, grip, wire hang, and pole climbing abilities of each mouse was evaluated and scored using the Irwin Test. At the end point of the ND$_3^{Pxl}$ study, mice were

transferred to the Neurobehavioral core for rotorod and hot plate response analyses. Mice were tested again one week post the final dose of therapy.

Statistical Analysis

All data generated using ND^{Pxl} and ND^{PB} was analyzed with a one-way ANOVA (Newman-Keuls Multiple Comparison Test) method for three sample sections or for two sample sets using a nonparametrical (Mann-Whitney) method. All data analysis was performed using the GraphPad Prism Software (San Diego, CA, USA).

CHAPTER III

OPTICAL IMAGING OF MATRIX METALLOPROTEINASE-7 *IN VIVO*

USING A PROTEOLYTIC NANOBEACON

<u>Introduction</u>

One of the defining characteristics of malignancy is the ability of cancer cells to metastasize and invade distant organ sites. Proteolysis of the ECM is required to accommodate increased growth, migration, and invasion of tumor cells. MMPs are a family of extracellular, zinc-dependent proteinases that are capable of degrading most of the multiple components of the ECM [31]. In the tumor microenvironment, host and tumor derived MMPs are often misregulated leading to uncontrolled degradation of the ECM. Of the 24 identified human MMP gene products, MMP7 is one of the smallest members of this family possessing only the domains necessary for targeting to the secretory pathway, control of latency, and catalytic activity. MMP7 is notably produced by cells of epithelial origin and contributes to tumor formation in a number of epithelial-derived adenocarcinomas [40, 41]. From a molecular imaging standpoint, MMP7 is a secreted extracellular proteinase that appears to be a promising target for *in vivo* detection of tumors and quantitative analysis. Thus, MMP7 provides an attractive target for developing an enhanced near-infrared (NIR) proteolytic beacon (PB) to non-invasively assess proteolytic activity.

The ability to probe tissue with light for minimal/non-invasive detection of cancer has become feasible mainly due to the development of fluorescent probes emitting in the near-infrared spectrum where tissue has both low absorption and reduced scattering [79]. A number of different fluorescent approaches have demonstrated the capability to detect specific molecular events *in vivo* [83, 94-96]. For optical imaging, Achilefu and colleagues have prepared a number of NIR optical contrast agents designed to either bind to or be metabolized by tumors and, together with Chance, has demonstrated the feasibility of detecting 2-cm deep subsurface tumors using a metabolism-enhanced NIR fluorescent contrast agent and NIRF *in vivo* imaging [97-99]. Weissleder and colleagues have utilized NIR probes to assess proteolytic activity and subsequent inhibition by MMP inhibitors [84, 100, 101]. The Tsien group described a new strategy using protease activatable cell-penetrating peptides to deliver fluorescent labels within tumor cells [88]. Probes have been developed to assess proteolytic activity based on FRET: endogenous quenching of closely positioned fluorochromes on peptide substrates that upon proteolytic cleavage produce enhanced fluorescence [80-82]. In particular, Pham *et al* have developed an MMP7 NIR probe that was capable of imaging protease activity *in vitro* [102]. Thus, the principle to detect proteolytic activity *in vitro* and *in vivo* has been demonstrated.

In the present study, we present the in vivo detection and quantitation of MMP7 activity using a specific near-infrared polymer-based proteolytic beacon, PB-M7NIR. PB-M7NIR is a pegylated polyamidoamine PAMAM-G4 dendrimer core covalently coupled to a Cy5.5 labeled peptide representing a selective substrate that

monitors MMP7 activity (S, sensor), and AF750 as an internal reference to monitor relative substrate concentration (R, reference). In vivo imaging of tumors expressing MMP7 had a median S/R ratio 2.2-fold higher than a bilateral control tumor. Ex-vivo imaging of intestines of multiple intestinal neoplasia (APCMin) mice injected systemically with PB-M7NIR revealed a 6-fold increase in S/R in the adenomas of APCMin mice compared to control intestinal tissue or adenomas from MMP7-null Min mice. PB-M7NIR detected tumor sizes as small as 0.01cm2, and S/R was independent of tumor size. Histological sectioning of xenograft tumors localized the proteolytic signal to the extracellular matrix; MMP7-overexpressing tumors displayed an approximately 300-fold enhancement in S/R compared to non-expressing tumor cells. In APCMin adenomas, the proteolytic signal co-localized with the endogenously-expressed MMP7 protein with S/R ratios approximately 6-fold greater than that of normal intestinal epithelium. PB-M7NIR provides a useful reagent for the in vivo and ex vivo quantitation and localization of MMP-selective proteolytic activity.

<u>Results</u>

Preparation and Fluorescence Properties of PB-M7NIR

PB-M7NIR was constructed on a pegylated (PEG5000) dendrimeric scaffold (Starburst®; G4-PAMAM) with both an optical protease sensor (Cy5.5-M7) and an internal reference, AF750 (Figure 6A). The peptide sequence of Cy5.5-M7 is based on a fluorogenic peptide that was optimized for MMP7 cleavage [89]. PB-M7NIR

reagent was prepared to have similar equivalents of sensor and reference fluorophores for optimal self-quenching and fluorescence resonance energy transfer quenching. After preparation, absorbance taken from product compared to reaction mixture yields an average of 8 Cy5.5-M7 peptide substrates and 6 AF750 reference fluorophores per PAMAM (Figure 6B). After treating PB-M7NIR with active MMP7, the relative increase in Cy5.5 spectral amplitude yields an approximate 5-fold increase in Cy5.5-fluorescence compared to the EDTA treated control (Figure 7). In contrast, the AF750 reference fluorescence signal increases minimally upon treatment remaining virtually the same signal as the EDTA-treated control. Comparison of the amplitudes of the emission spectra of PB-M7NIR before and after treatment with MMP7 shows that the Cy5.5 fluorescence signal functions as an optical sensor to detect proteolysis of the Cy5.5-M7 peptide, whereas the AF750 fluorescence serves as an internal reference to monitor the total (cleaved and uncleaved) concentration of the reagent, consistent with the original design of this PB.

1. A). Pegylation of PAMAM with PEG5000

G4-PAMAM + PEG5000-NHS ester ⟶ PAMAM-PEG5000
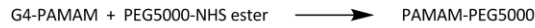
B). Activation of PAMAM-PEG5000

PAMAM-PEG5000 + SIA ⟶ IA-PAMAM-PEG5000

C). Labeling M7 peptide with Cy5.5

MMP-7 Cleavage site

(AHX)RPLA*LWRS(AHX)C-(COOH) + Cy5.5-NHS ester ⟶ Cy5.5-M7 conjugate

N-Terminal Amine   Sulfhydryl to attach to PAMAM
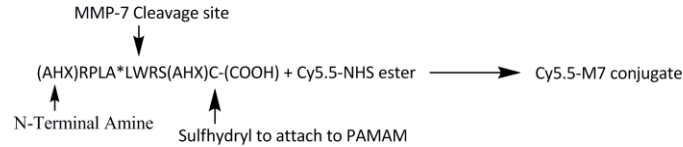
2. Coupling Cy5.5-M7 to IA-PAMAM-PEG

IA-PAMAM-PEG5000 ⟶ (Cy5.5-M7)$_8$-PAMAM-PEG5000
Cy5.5-M7
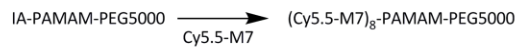
3. Coupling of AF750 to (Cy5.5-M7)8-PAMAM-PEG5000

(Cy5.5-M7)$_8$-PAMAM-PEG5000 $\xrightarrow{AF750}$ (Cy5.5-M7)$_8$-PAMAM-(PEG5000)(AF750)$_6$
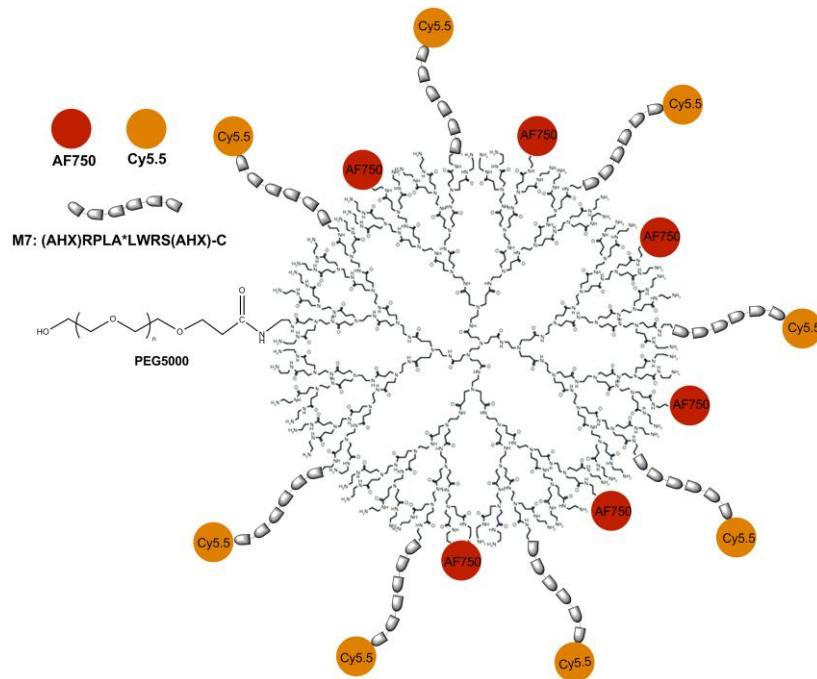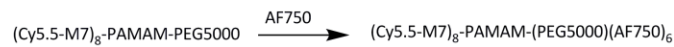
Figure 6: Synthesis and structure of PB-M7NIR
A). Scheme for the synthesis of PB-M7NIR, a (Cy5-M7)8-PAMAM-(PEG5000) (AF750)6 co-polymer. SIA = N-Succinimidyl iodoacetate B.)The Cy5.5 optical sensor is linked via AHX to the N-terminus of the MMP selective cleavable peptide (RPLA*LWRS, cleavage site denoted by asterisk) that is coupled via a second AHX and Cysteine with the PAMAM. The internal reference, AF750, of PB-M7NIR is linked directly to the dendrimer (Starburst® PAMAM dendrimer, Generation 4). Structure is not drawn to scale.
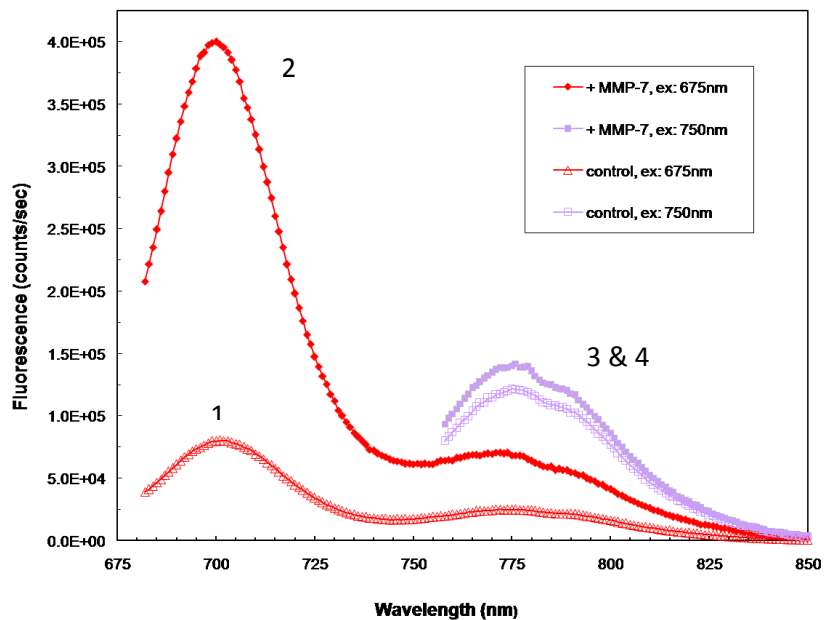
Figure 7: Fluorescence spectra for PB-M7NIR before and after MMP7 treatment.
Spectra 1 represent the untreated PB-M7NIR Cy5.5-M7 peptide and spectra 3 the untreated AF750 internal reference. Spectra 2 demonstrates an approximately 5 fold increase in fluorescence of the Cy5.5 sensor post MMP7 treatment while spectra 4 demonstrates a minimal increase in fluorescence post MMP7 treatment.

In vivo imaging of subcutaneous xenograft tumors

To evaluate the selectivity of PB-M7NIR, athymic nude mice were subcutaneously injected on either flank with a human colon cancer cell line that does not express MMP7 (SW480neo), and a cell line derived from the same parental cells following transfection with the human MMP7-cDNA (SW480mat). Mice were imaged at various time points up to four hours post injection in the Cy5.5 channel to measure the Cy5.5 *sensor* signal and in the ICG channel to measure the AF750 *reference* signal (Figure 8A-C). Signal in the reference channel was highest at the first measurement after injection (1 hr) and decreased thereafter, presumably due to the clearance of the cleaved and uncleaved PAMAM-AF750 core (Figure 8D). In contrast, the sensor signal markedly increased over the first three hours consistent with MMP7 cleavage resulting in enhanced fluorescence in the Cy5.5 channel. Sensor signals varied in intensity from mouse-to-mouse; however, signal in the control tumor was always less than in the MMP7 expressing tumors in the same mouse (Table 4). To further evaluate the effective cleavage of PB-M7NIR, sensor to internal reference ratios (S/R) were calculated to assess the cleaved (sensor, S) to total substrate (reference, R) retained in the tumor; S/R ratio increased over time (Figure 8D). Using data from the four hour time point, S/R ratios were calculated for the control neo tumor and the MMP7 expressing mat tumor (Table 4). The S/R ratio in the MMP7 expressing mat tumors ranged from 24 to greater than 1000, with an average of 275 and median of 60.8. The control neo tumor in the same animal consistently showed a lower S/R ratio (Figure 8E), but the numbers where highly variable and ranged from 1 to 293 (mean= 69.7 and median=39.2). Despite mouse-

to-mouse variation, the S/R ratio in the MMP7-expressing tumors divided by the S/R ratios in the control tumor in the same mouse gave an average of 6.8 fold increase and a median of 2.2 (Figure 8F, Table 4).
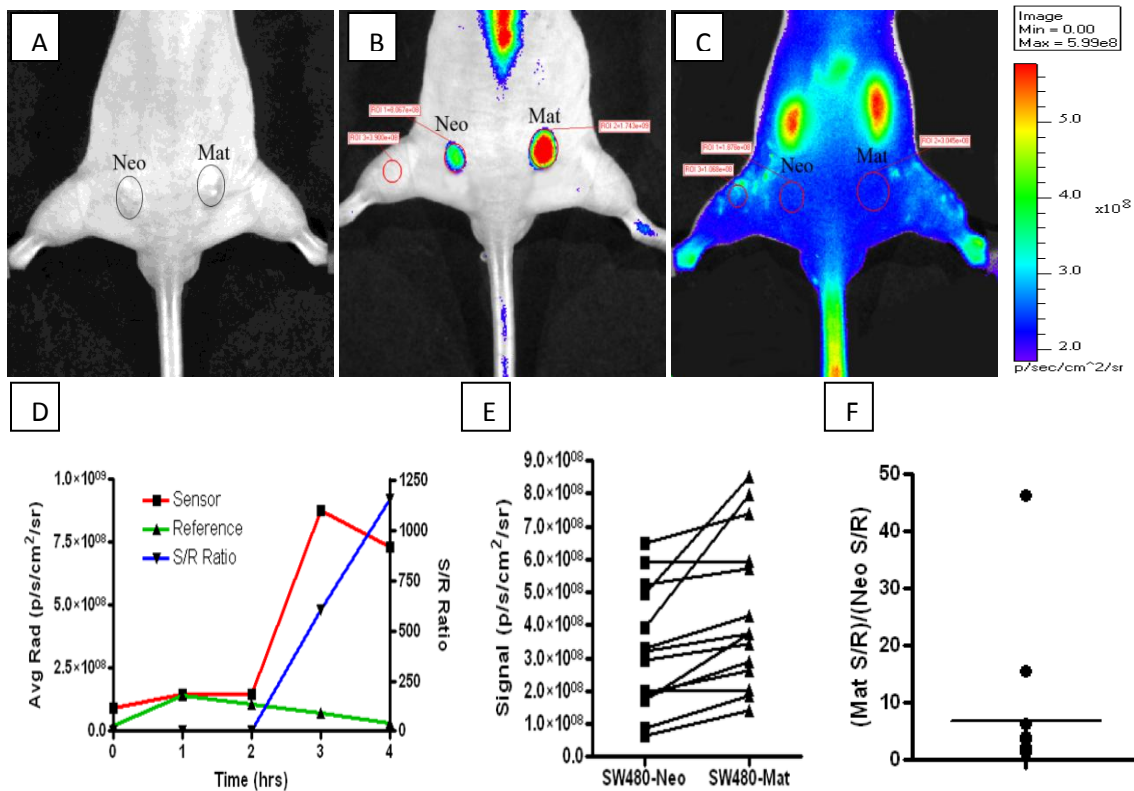
Figure 8: *In vivo* **imaging of MMP7 beacon selectivity by quantitative fluorescence imaging of mouse subcutaneous Xenograft tumors using PB-M7NIR**

Subcutaneous injection into nude mice of either SW480neo or SW480mat cells resulted in xenograft tumors within 3-4weeks, in the dorsal, caudal view of the mouse. The areas (approx. $57mm^2$ each) are shown in white light (A), the Cy5.5 *Sensor* channel (B), and the ICG *Reference* channels (C) and were obtained 4hr post retro-orbital intravenous injection of PB-M7NIR (B) Demonstration of effective cleavage of PB-M7NIR sensor signal in the Mat MMP7 tumor with reduced signal in the Neo control tumor. (C) Shows the uniform reference signal in the both mat and neo tumors with accumulation of PB-M7NIR in the kidneys and liver of the mouse. (D) Sensor and reference signals plotted over time in a mat tumor showing increased signal in the sensor channel starting at the 2hr time point reaching a maxima at the 3-4hr imaging point. S/R ratio increases as the cleaved and uncleaved reagent clear the circulatory system. (E) Sensor signal (n=13) variation occurs in both tumors but remains higher in mat tumors. (F). Mat S/R ratio divided by the control neo S/R ratios gives an average of 6.8 fold increase and a median of 2.24 (See Table 1 for Raw Data).

Mouse	Neo Tumor				Mat Tumor				Mat S/R Neo S/R
	Tumor Size (cm)	Signal (p/s/cm/sr)	Reference (p/s/cm/sr)	S/R Ratio	Tumor Size (cm)	Signal (p/s/cm/sr)	Reference (p/s/cm/sr)	S/R Ratio	
1	1.10	6.75E+06	6.47E+06	1.04	0.80	3.40E+08	7.34E+06	46.3	44.5
2	0.88	4.14E+08	2.00E+07	24.3	0.46	4.87E+08	1.20E+07	34.5	1.42
3	0.70	9.40E+07	1.70E+07	5.54	0.71	4.90E+08	1.43E+07	34.3	6.19
4	0.71	1.19E+08	1.60E+06	74.3	0.70	1.74E+08	1.50E+05	1160	15.6
5	0.58	1.69E+08	2.24E+06	75.4	0.82	2.61E+08	9.10E+05	287	3.80
6	1.20	1.82E+08	6.38E+06	28.5	0.81	3.14E+08	5.58E+06	57.0	2.00
7	0.29	6.15E+07	3.50E+06	17.6	0.83	1.38E+08	9.90E+06	39.3	2.24
8	0.35	8.33E+07	3.74E+06	19.7	0.46	8.97E+07	4.22E+06	24.0	1.22
9	0.19	1.06E+08	3.60E+05	293	0.31	2.93E+08	1.17E+05	1150	3.93
10	0.21	8.59E+07	4.30E+06	199	0.32	1.87E+08	4.30E+06	435	2.18
11	0.29	3.49E+08	4.07E+06	85.8	0.23	4.54E+08	4.02E+06	113	1.32
12	0.34	1.72E+08	4.37E+06	39.2	0.28	3.73E+08	2.72E+06	137	3.49
13	0.58	1.76E+08	4.12E+06	42.6	0.81	2.33E+08	3.83E+06	60.8	1.43
				Avg. =69.7				Avg = 275	Avg. = 6.87

Table 4: Fluorescence Imaging Detection of PB-M7NIR *in vivo*
Fluorescence intensities (photons/sec/cm^2/steradian) measured in the Cy5.5 (signal) and ICG (reference) channels (n=13) of images containing anesthetized live mice carrying bilateral xenograft tumors (SW480neo and SW480mat). Regions of interest were drawn around the tumors and results are expressed in avg. radiance after correction for background signal (see experimental section). Results were taken at the 4hr time point post injection of PB-M7NIR with sensor/reference ratios determined for each tumor with an average (Mat tumor S/R)/(Neo tumor S/R) of 6.87 with a median of 2.24.

Quantitative ex vivo fluorescence imaging of PB-M7NIR in histological sections

To localize MMP activity in the tumor microenvironment at the cellular level, subcutaneous xenograft tumors were removed 4 hr post injection of PB-M7NIR and snap frozen prior to cryostat sectioning (z = 5 μm). Sections were aqueously mounted with DAPI and analyzed by fluorescence microscopy (Figure 9A-C). In the MMP7 positive xenograft tumors, PB-M7NIR sensor signal was predominately localized at the tumor-stroma interface with high fluorescence being detected in the ECM (Fig 9A-D). Sensor signal was not localized in the control tumors and remained lower than the MMP7 positive tumor signal for all mice. Sensor/reference ratios were calculated for each sample in three different regions of the tumor (Figure 9E). The S/R ratio in the MMP7 expressing tumors ranged from 600 to over a 1000, with an average of 692 and a median of 629. The control neo tumor in the corresponding animal consistently showed a lower S/R ratio with an average of 2.3 and a median of 1.9. On average, the Mat S/R ratio divided by Neo S/R ratio gave a average 355-fold increase and a median of 360 (Figure 9 E,F). It should be noted that the sensor and reference signals measured using the fluorescent microscope are in counts/sec differing from the average radiance measurements using the IVIS instrument. However, the dramatic increase in S/R ratios in the MMP7 positive tumors compared to the control tumors confirms the ability of PB-M7NIR to effectively localize and assess MMP7 activity in the tumor microenvironment.

Figure 9 -Quantitative Fluorescence imaging of PB-M7NIR in the tumor microenvironment
SW480 xenograft tumors were harvested post injection of PB-M7NIR at 4hr and frozen in OCT, sectioned, and stained with DAPI. Images taken with the Axiophot fluorescent microscope (40X images, white dash =50 microns) in the DAPI channel showing the tumor stroma interface (A), Cy5.5 *Sensor* Channel demonstrating activation of PB-M7NIR in the ECM (B), and the Cy7 *Reference* channel showing uptake of PB-M7NIR at the tumor-stroma boundary (C). (D) A merge of the images from there respected channels demonstrates the cleavage of the sensor in the ECM and the accumulation of reference signal at the outer rim of the tumor. (D) Sensor to Reference ratio values were calculated from the integrated background-corrected intensities for neo and mat tumors using metamorph software, images were taken in triplicate and averaged. (F) Shows the Neo-Mat S/R ratios for the sectioned slices calculated using the integrated fluorescence intensities.

Ex Vivo imaging of MMP7 activity in APC^Min mice

The sensitivity of PB-M7NIR was tested by identifying intestinal adenomatous polyps in APC^Min mice. PB-M7NIR was administered to 15-week old APC^Min mice by retro-orbital injection and the mice were sacrificed 1hr post injection. The intestines and colon removed and opened longitudinally displaying luminal adenomas. Adenomas were imaged under white light, Cy5.5-*Sensor*, and ICG-*Reference* channels (Figure 10 A-D). Adenomas in APC^Min mice demonstrated robust sensor signal, with S/R ratios averaging approximately 100 (Figure 10 E & F). In contrast, the intestines of wild type mice demonstrated very little fluorescence in the sensor channel, with S/R ratios less than 2 (Figure 10 F). PB-M7NIR was capable of detecting polyps of all sizes with S/R ratios remaining independent of tumor size and efficient cleavage resulting in the detection of adenomas as small as 0.01 cm^2 (Figure 10 E-G). To determine the selectivity of the signal, APC^Min mice genetically deficient in MMP7 were generated[48] and the intestines imaged with PB-M7NIR. Although these mice develop less tumors due to the deficiency in MMP7, the tumors that do develop have a much lower sensor signal than WT APC^Min mice, and an average S/R ratio of 7 (Figure 10E, F). Statistical analysis was performed on this data using a one-way ANOVA with a Newman-Kuels multiple comparison test showing significant differences between Min and WT ($p<0.001$) as well as Min and Min-7-null ($p<0.001$) datasets, and an approximately 6-fold S/R enhancement (Min vs. Min-7-null) that can be specifically attributed to MMP7.
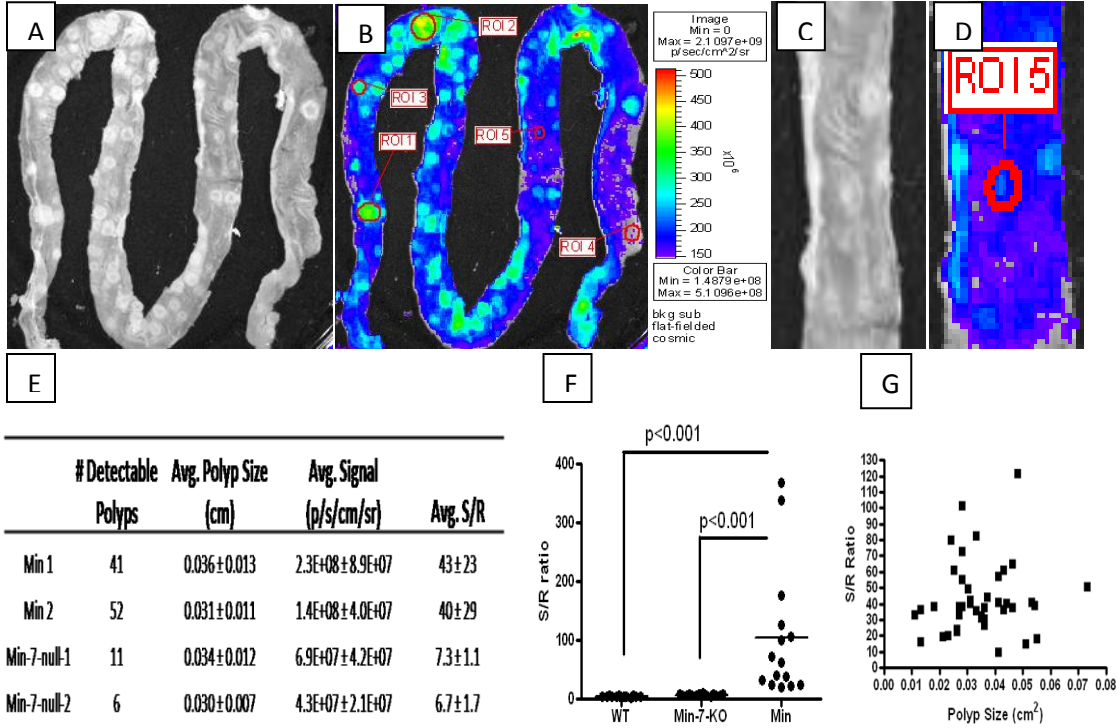
Figure 10: **Quantitative Fluorescence imaging of *ex vivo* APC^{MIN} intestinal adenomas**

Ex-vivo imaging of MMP7 activity in intestinal adenomas (A) White light image of explanted mouse intestine from APC^{MIN} mouse with spontaneous polyps after post-injection of PB-M7NIR Beacon (60min removal). (B) NIRF image in the Cy5.5 channel (sensor) signal showing tumor MMP7 activity with additional smaller adenomas visible (C&D). (E) Table of data showing the reduced number of polyps in the Min-null mice compared to the Min-WT mice with significantly higher signal in polyps of the APC^{Min} mice. S/R ratios averaged ~40 in Min mice with decreased S/R ratios in Min-7-null mice. (F) S/R ratios for WT, Min-7-null, and Min-WT mice showing significant ($p<0.001$, one-way ANOVA) for Min to WT and Min to Min-7-null animals.(G) S/R Ratios showing size independent activation of PB-M7NIR and detection of MMP7 at various polyp size.

Ex vivo histological imaging of adenomas

To determine on a cellular level where PB-M7NIR has been activated by MMP7 in the APC^{Min} model, both whole mount and sagital sections of intestinal adenomas were imaged in the Cy5.5 (sensor) and Cy7 (reference) channels by fluorescence microscopy at 10X and 40X magnification. Sensor to reference ratios between seven to greater than 25 were observed in the adenomas of APC^{Min} mice (Figure 11 J). As a control, normal wild type C57Bl6 mice treated with PB-M7NIR had their intestines removed and imaged in the same manner, showing limited activation of the beacon with S/R ratios less than three (Figure 11 J). To confirm the presence and localization of MMP7, histochemical analysis was performed using a monoclonal antibody for MMP7. Images are shown at 40X magnification for the same sectioned adenoma verifying that MMP7 localizes to the epithelial compartment of the adenomas (Figure 11 K, L). Similar to the results with *ex vivo* IVIS imaging, the adenomas displayed an approximately 6-fold enhancement in signal that could be specifically attributable to MMP7.
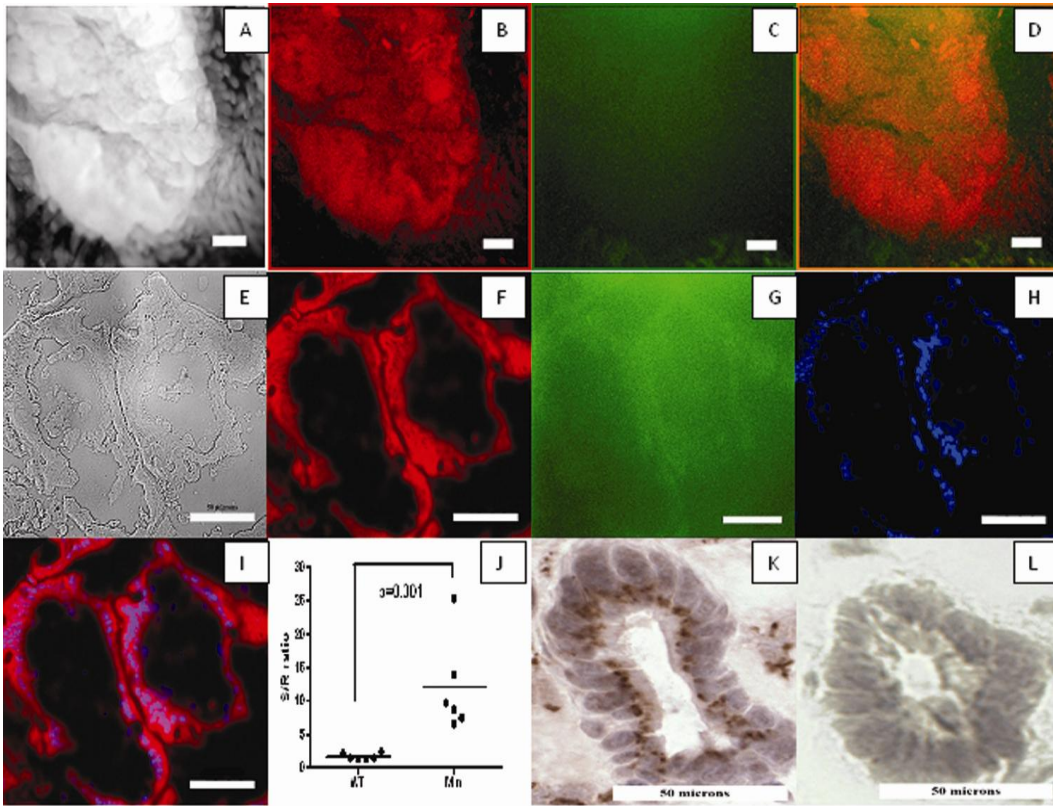
Figure 11- *Ex vivo* quantitative imaging of adenoma microenvironment

E*x* vivo white light image of intestinal adenoma from APC Min mouse at 10X magnification (A). False coloring applied to the same adenoma in the Cy5.5 (sensor-red) channel showing activated PB-M7NIR in the lumen (B). The Cy7 (Reference-green) channel does not detect AF750 signal in same adenoma (C). Images from both Cy5.5 and Cy7 channels merged to localize PB-M7NIR activation (D). A 5um sagital section of the previous adenoma was taken at 40X magnification in white light (E), Cy5.5 sensor channel showing PB-M7NIR signal (F), Cy7 reference signal (G), and DAPI signal (nuclear staining) (H). Images from the Cy5.5, DAPI, and Cy7 channel merged and localized expression of PB-M7NIR to the basolateral side (I). Quantitative fluorescent images were analyzed using Metamorph software with intensities recorded in counts/sec. Sensor to Reference ratios were calculated after background subtraction for PB-M7NIR showing a significant difference from Min adenomas to WT intestinal tissue (J). Immunohistochemistry shows MMP7 staining in epithelial cells of a section from the previous adenoma (A-I) and its respective IgG control. This specific staining pattern corresponds to the cleavage and activation of PB-M7NIR seen in the Cy5.5 (sensor) channels. (A-D white line=100 microns; E-I white line=50 microns)

Conclusions

In summary, PB-M7NIR is the first of the dendrimeric near-infrared fluorescent probes designed for the *in vivo* detection and imaging of MMP7 activity. The intravenous administration of PB-M7NIR allowed for the sensitive and selective visualization and localization of MMP7 activity in whole animals and in tissue sections. The ability to image the tumor microenvironment may help to distinguish the specific functions of MMPs at various stages of tumor progression and in different tumor models. *In vivo* assessment of MMPs activity may aid in the evaluation of the tumor and in the development of MMP-targeted therapies. Reagents of this type can easily be modified to image a wide variety of diseases associated with enhanced proteolytic activity.

CHAPTER IV

MIX-AND-MATCH NANODENDRONS FOR DETECTION AND

TREATMENT OF BREAST CANCER METASTASES

Introduction

Morbidity is related to the ability of tumor cells to metastasize throughout

the body. Women with localized breast cancers treated with surgery have a 97.5%

5-year survival rate, but survival drops to 25.5% for women with distant metastases

[2]. Metastasis is the hallmark of late stage (stage IV) breast cancer. Metastatic lesions

go through stages of progression in that they start as single or small clusters of cells

that must survive in a foreign organ, establish a competent microenvironment,

grow, and undergo an angiogenic switch before they become clinically detectable

metastases [4]. The survival benefit of adjuvant therapy supports the notion that

targeting "early stage" metastases can be effective in reducing early mortality due to

metastatic diseases. The need to selectively identify and eliminate small clusters of

abnormal cells calls for sophisticated new technologies. Nanostructures – materials

with at least one dimension less than 100 nm – have been used for cancer diagnosis,

imaging and therapy for many years. However, the critical feature that

characterizes modern nanotechnology is the capability to design and fabricate

complex structures with defined function(s) with exquisite control [66]. The capability

to synthesize complex nanostructures enables the combination of functions and

offers the power to colocalize medical image contrast enhancement and drug

delivery. The ability to combine several distinct functions on a single element is a characteristic that distinguishes nanotechnology from traditional chemistry approaches, and provides the opportunity to develop cancer detection, prevention, or treatment strategies in single dose administration.

Here we describe a novel set of compounds that selectively detect and target tumors by virtue of their expression of the matrix metalloproteinase MMP9. The compounds made are a new class of self-reporting nanoparticle based imaging/therapeutics with molecular recognition and targeting capabilities designed specifically for enhanced treatment of breast cancer, and in particular breast cancer metastases. The focus is on solubilizing and delivering pro-paclitaxel (PXL) with compounds that can be linked together to provide early assessments of therapeutic efficacy towards metastatic breast cancer lesions while minimizing side effects of standard chemotherapy.

<div align="center">Results</div>

Optimization of Förster Resonance Energy Transfer

FRET is a nonradiative energy transfer method based on dipole-dipole interactions involving donor and acceptor fluorophores which are spatially separated by a distance usually between 1 and 10 nanometers [103]. Intramolecular FRET is based on the donor and acceptor being connected by a linker where energy transfer is between a single donor and acceptor [104]. In designing and optimizing new molecular beacons it is critical to test donor and acceptor pairs on the labeled

substrate. The maximum estimated spacing between donor and acceptor pairs for the MMP9 substrate is 47.2 Å and therefore is consistent with efficient energy transfer between fluorophores (Figure 12). Fluorophores were tested for FRET in different combinations using the LI-COR PEARL® Imaging System. AF700, LI700, and VE680 fluorophores are commercially available as NHS carboxylic succinimidyl ester formats and were tested as donor fluorophores. AF750 and LI800 are available as maleimide compounds and served as acceptor fluorophores. These pairs were linked in 6 different combinations to the MMP9 substrate H2N-AHX-AVRWLLTA-AHX-C-COOH at the amine and thiol reactive sites (Figure 12). The products were purified using preparative HPLC and digested with MMP9 and trypsin to ensure cleavage of the substrate. Emission was measured for each dye using the LI-COR Odyssey® imaging system in the 700 and 800nm channels (Table 5). The best change in signal arose from the AF700 and AF750 pair of fluorophores giving approximately 25-fold increase in signal. Interestingly, the AF750 acceptor fluorophore signal also increases approximately 7-fold, indicating there is significant reverse FRET between these fluorophores and/or dye stacking [105]. Upon digesting, the change in signal for the VE680/LI800 pair increases almost 9-fold in the 700 channel, however overall signal was much weaker than with the AF700/AF750 pair (Table 5).
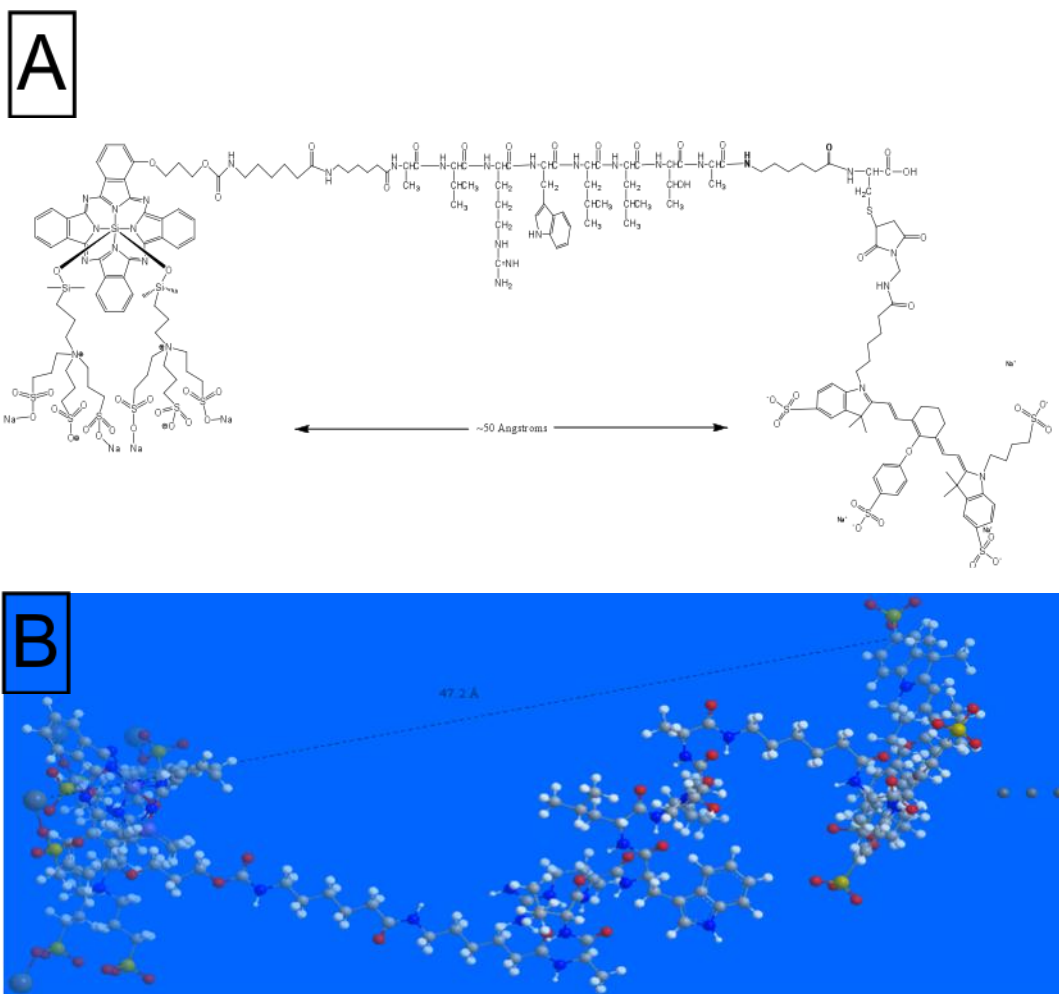
Figure 12: Optimization of FRET Parameters Using a MMP9 Substrate
Licor700-AHX-AVRW*LLTA-AHX-C(Licor800)-COOH labeled MMP9 substrate structure (A) and Chemdraw 3D file demonstrating the maximum distance between the two fluorescent dyes. Optimum FRET distance is <100 Angstroms; ~ distance between FRET pairs on MMP9 substrate 47.2 Å.

Table 5: Current Near-Infrared Fluorophores Available for Amine and Thiol Chemistry & Their FRET Properties When Linked to an MMP9 Substrate

Fluorophore	Ex	Em	FRET PAIR	Δ Sen	Δ Ref
AF700	695	719			
			AF700/AF750	24.66	6.77
AF750	752	779	AF700/LI800	5.77	2.10
Li700	689	700	LI700/AF750	1.09	0.78
			LI700/LI800	0.22	0.00
Li800	774	794			
			VE680/AF750	4.56	3.88
VE680	679	702	VE680/LI800	8.98	2.88

*** The left side of the table denotes the excitation and emission wavelengths for each commercially available fluorophore. The right side demonstrates the different FRET pair combinations that were tested in triplicate during the digestion assay. The average change in signal was calculated for each pair in the 700nm (Sen) and 800nm (Ref) channels and is expressed as counts/sec.

Design and Synthesis of Mix-and-Match Nanodendrons: Developing Generation 2 Dendrons for Imaging Quantification of Proteolytic Activity

Nanodendron proteolytic beacon (ND[PB]) was built using the best overall performing FRET pairs AF700/AF750. ND[PB] is an optical imaging proteolytic beacon that is designed to detect MMP9 activity. Building on previous versions of PBs we utilized a dendron scaffold to act as a vehicle for the MMP9 substrate that serves as the optical detection agent upon cleavage. ND[PB] was constructed on a 2-(benzyloxycarbonyl)-2-methylpropane-1,3-diyl-bis(3-hydroxy-2-(hydroxymethyl)-2-methylpropanoate) dendron (Figure 13, compound [1]). The peptide sequence is based on a fluorogenic peptide that was optimized for selective cleavage by MMP9 [89]. The dendron was modified by attaching formyl benzoic acid to provide aldehyde groups for oxime ligations between the dendron and the MMP9 selective peptide (Figure 13, compound [2]). The MMP9 selective peptide H2N-[AHX]-AVRW*LLTA-[AHX]-C-DprAOA-amide (or alternatively the D-AA version) was attached in 0.3 M ammonium acetate buffer at pH 4.5 in DMSO with 100 mM concentration of aniline to yielding a product with 4 peptides per dendron (Figure 13, compound [3]). AlexaFluor 700 NHS-ester and AlexaFluor 750 maleimide are then added to the MMP9 peptide to produce ND[PB] (Figure 13, compound [4]). Each reaction step was monitored with size exclusion high performance liquid chromatography (SEC-HPLC) and showed the expected increase in size as determined by a decrease in retention time by SEC-HPLC (Figure 13). The resulting ND[PB] reagent was prepared to have similar equivalents of sensor and reference fluorophores for optimal self-quenching and fluorescence resonance energy transfer quenching. During and after

preparation, absorbance spectra taken from product compared to reaction mixture yields an average of 4 AF700 and 4 AF750 reference fluorophores per ND (Figure 14, A, B). After treating ND[PB] with active MMP9, the relative increase in AF700 spectral amplitude yields an approximate 7.4-fold increase in AF700-fluorescence compared to the EDTA-treated control (Figure 14, B, C). In contrast, the AF750 reference fluorescence signal increases minimally upon treatment remaining similar to signal from the EDTA-treated control. Comparison of the amplitudes of the emission spectra of ND[PB] before and after treatment with MMP9 shows that the AF700 fluorescence signal functions as an optical sensor to detect proteolysis of the MMP-9 peptide, whereas the AF750 fluorescence serves as an internal reference to monitor the total (cleaved and uncleaved) concentration of the reagent, consistent with the original design of this ND.
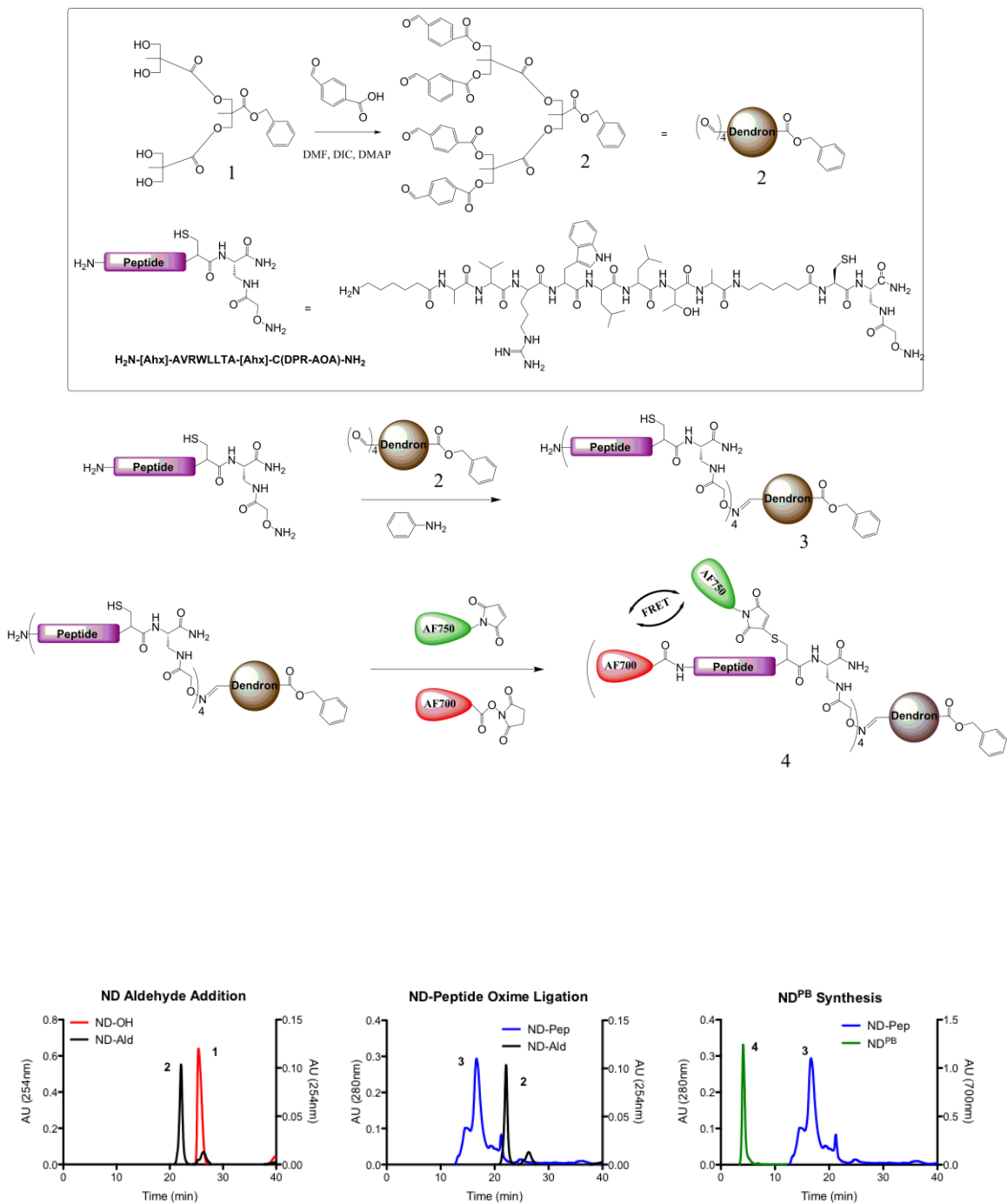
Figure 13: Schematic illustrating the synthesis of ND^PB with SEC-HPLC to validate synthesis
Refer to numbers throughout the schematic to relate to products found in the SEC HPLC traces.
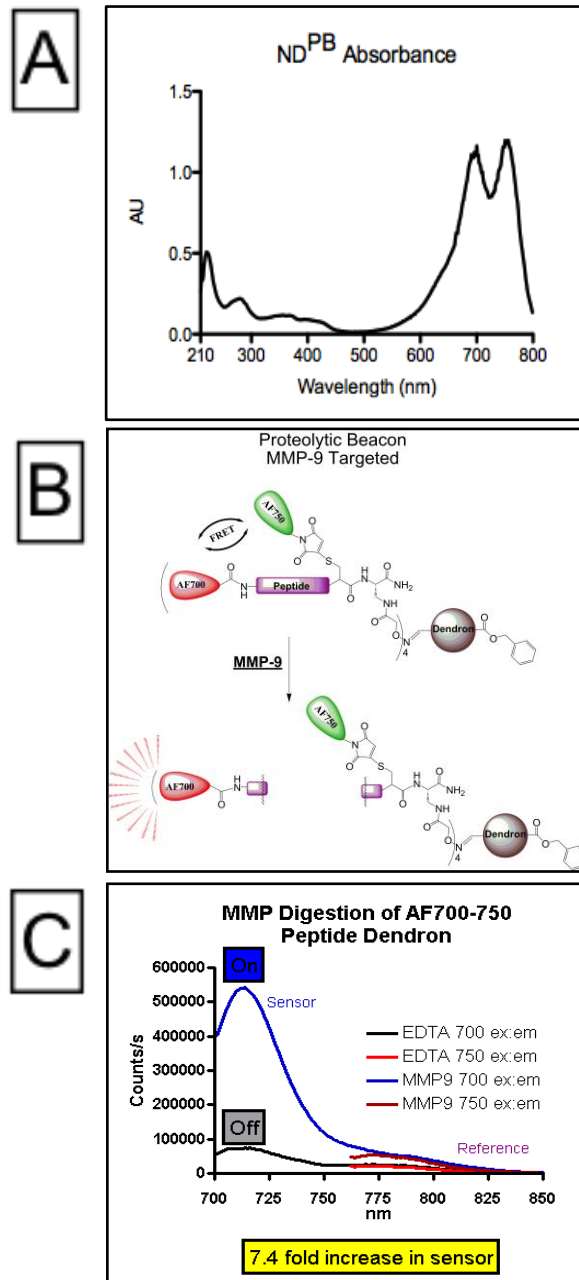
Figure 14: Characterization of ND^PB

Absorbance of ND^PB with 4 AF700 and 4 AF750 dyes per construct (a) FRET is demonstrated by taking the emission profiles of the AF700 (sensor) and AF750 (reference) molecules in the presence of MMP9 and ethylene-diamine-tetra-acetic acid (EDTA) (b & c) There is a 7.4 fold increase in sensor signal with a minimal increase in reference signal, allowing quantization of cleaved substrate and MMP9 activity.

Determining Protease Activation in Phantoms: Quantitative Beacon Analysis as an Estimate of Cleavage

For subcutaneous detection and imaging of ND[PB], samples of uncleaved (ND[PB]-EDTA), MMP9 cleaved (ND[PB]), and D-AA (ND[PB]-DAA) were diluted 10 fold into Matrigel™ at 4 °C. Aliquots of 100 µl were injected subcutaneously into several sites near the mammary glands of FVB-WT mice in different combinations. All mice were injected with Matrigel™ samples alone as controls, and were imaged with the LI-COR PEARL® imaging system in the visible, 700nm, and 800nm channels. 0.3 µM concentrations of ND[PB], ND[PB]-EDTA, and ND[PB]-DAA were first injected to demonstrate FRET visualization (Figure 15 A-C). ND[PB] gave a Sensor/Reference (S/R) ratio of 28.9 in comparison to 2.8 and 2.6 for ND[PB]-EDTA and ND[PB]-DAA respectively (Figure 15 J). By measuring fluorescence as a function of concentration of the cleaved ND[PB] probe, the limit of detection was found to be ~0.1µM ND[PB] in such phantoms (Figure 15 D-F, K). To maintain a constant concentration of acceptor dye AF750, activated ND[PB] was mixed with ND[PB]-DAA and was injected at 0, 10, 20, 50, and 100% ND[PB] (Figure 15 G-I, L). Values for S/R ratios, as well as sensor and reference signals, were later used to estimate the cleavage of the substrate and its concentration occurring at a tumor site.
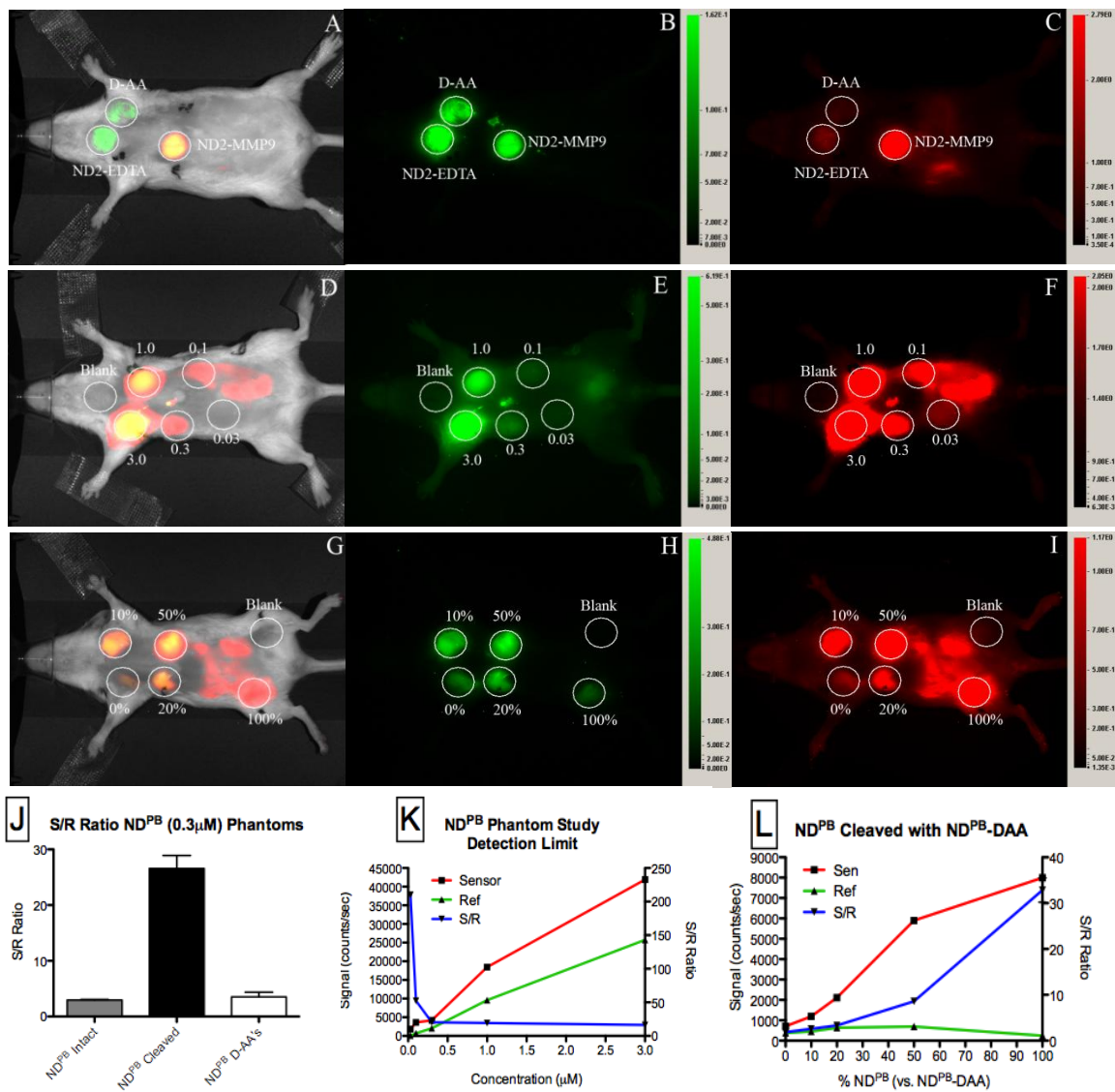
Figure 15: ND^PB phantom studies
ND^PB, ND^PB w/EDTA, and ND^PB-DAA with MMP-9 in Tricine buffer 30mM EDTA were digested with MMP9 diluted 10X into Matrigel™ at various concentrations and imaged in the LI-COR PEARL® with overlay (A, D, G), 800nm (B, E, H), and 700nm (C, F, I) channels. 0.3μM of ND^PB, ND^PB w/EDTA, and ND^PB-DAA were subcutaneously injected and S/R ratios quantified (A-C and J). The detection limits of the PEARL were tested with 3, 1, 0.3, 0.1, and 0.03μM concentrations of ND^PB cleaved with MMP9 (D-F, K-Reference at 10X). ND^PB and ND^PB-DAA were imaged together to maintain a constant concentration of reference signal at different % of MMP9 cleaved ND^PB (G-I, L)

Imaging Selectivity of ND^{PB} using a Xenograft model

Murine Lewis lung carcinoma (LLC) cells, derived from a spontaneously arising lung carcinoma in C57Bl-6 mice, normally express very low levels of MMP9. Cells were transfected with a human MMP9 expression vector (LLC-MMP9 (+)) and the empty vector to serve as a control (LLC-MMP9 (-) [92, 106]. Control and MMP9 expressing xenograft tumors were established on the flanks of athymic nude mice by subcutaneous injection of 5x10^6 LLC-MMP9 (+) or LLC-MMP9 (-) cells. Tumors of approximately 1-2cm developed after 2 weeks of growth at which point the animals were anaesthetized and images were recorded using the LICOR PEARL® imaging system in the visible, 700, and 800 nm channels to serve as background tissue fluorescence control images. Eight mice were then administered 3nMoles of ND^{PB} retro-orbitally in 100 µl of sterile 0.9% saline. Mice were imaged directly after injection of ND^{PB} and at hourly time points for up to 6 hours (Figure 16 A-C). Two mice had undetectable tumor activity, possibly due to an elevated production of the antiangiogenic compound angiostatin [107]. Responding animals had S/R ratios in MMP9 (+) tumors ranging from 193 to 8.3 with an average of 44.2 (Figure 16 D). S/R ratios in MMP9 (-) tumors averaged 12.7 (Figure 16 D, E). One animal has significantly higher signals in both tumors that might be attributed to receiving a higher dose of ND^{PB} or an unusually low rate of clearance. Sensor signals were always higher in the MMP9 positive tumors with S/R ratios of MMP9 positive tumors to S/R ratios of MMP9 negative tumors averaging 4.6 ± 2.4 (Figure 16 D, E, p=0.04).
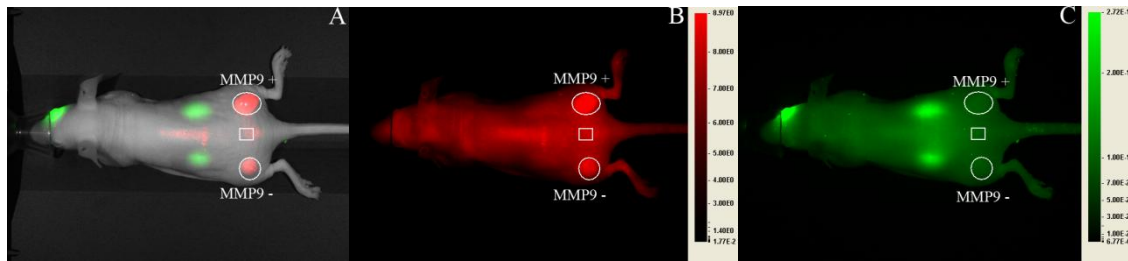
| M#	LLC-MMP9 (+) Tumors				LLC-MMP9 (-) Tumors				(MMP9+S/R) (MMP9- S/R)
	Tumor Vol. (mm³)	Sensor (counts/sec)	Reference (counts/sec)	S/R	Tumor Vol. (mm³)	Sensor (counts/sec)	Reference (counts/sec)	S/R	
1	339.1	6855.2	273.8	25	514.4	1207	260	4.6	5.4
2	72.9	3563.5	372.1	9.6	182.6	766.3	170.4	4.5	2.1
3	381	20894.9	107.9	193.6	240.1	9584.9	162	59.2	3.3
4	652.5	2362.1	284	8.3	337.4	847.5	412.2	2.1	4.0
5	145.9	1692.9	109.1	15.5	148.8	309.5	191.3	1.6	9.6
6	296	3953.7	300.6	13.2	487.1	1293.5	300.4	4.3	3.1
								Avg.	**4.6**
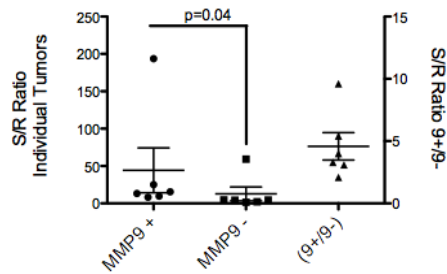
Figure 16: Imaging Selectivity of ND^PB using LLC-MMP9 (+) and LLC-MMP9 (-) xenograft tumors. Images of a representative mouse 4 hours post injection of ND^PB in the visible with overlay, 700nm sensor channel, and 800nm reference channel (A-C). Tumor volumes, Sensor Signal, Reference Signal, and S/R ratios were quantified and compared for MMP9 (+) and (-) xenograft tumors (D, E).

Exploring Protease Activity in the Presence of MMP Inhibitor GM6001 and Using D-Amino Acids

To test ND[PB] in an orthotopic model of breast cancer, MMTV-PyVT1-luc cells derived from an MMTV-PyVT transgenic mouse [28], were established in mammary gland number two of eleven FVB-WT mice. Tumors were given 1 week to establish palpable growths and imaged with 1.0nMole ND[PB]. Typical results for imaging these animals in the sensor channel and reference channels indicate significant MMP9 activity in the tumor site with S/R ratios of 9.8 ± 4.2 (n=11, Figure 17, 18 A). The kinetics of ND[PB] in a typical mouse usually takes 4-6 hours for detectable levels of reference signal to exit the system; however sensor signal around tumor sites is still significantly high at 4 hours post injection (Figure 17, D). Results for five of the eleven mice are shown in Figure 17, E. These five mice were selected because of their high proteolytic activity (S/R ratios 11.4 ± 5.6 Figure 17, E) and administered 35 mg/kg GM6001, a broad spectrum MMP inhibitor, intraperitoneally for three days. Two hours after the last injection of GM6001, these mice were reimaged with ND[PB], demonstrating a 6.6 fold reduction in beacon activity (p= 0.001, Figure 18 B, C). Ratios for sensor signal and S/R before and after GM6001 treatment averaged 7 ± 2 and 15 ± 6 fold respectively. Five mice were also imaged with ND[PB]-DAA at this time and had very low S/R ratios with an average of 0.7 ± 0.4 (Figure 18, D, p=0.0004).
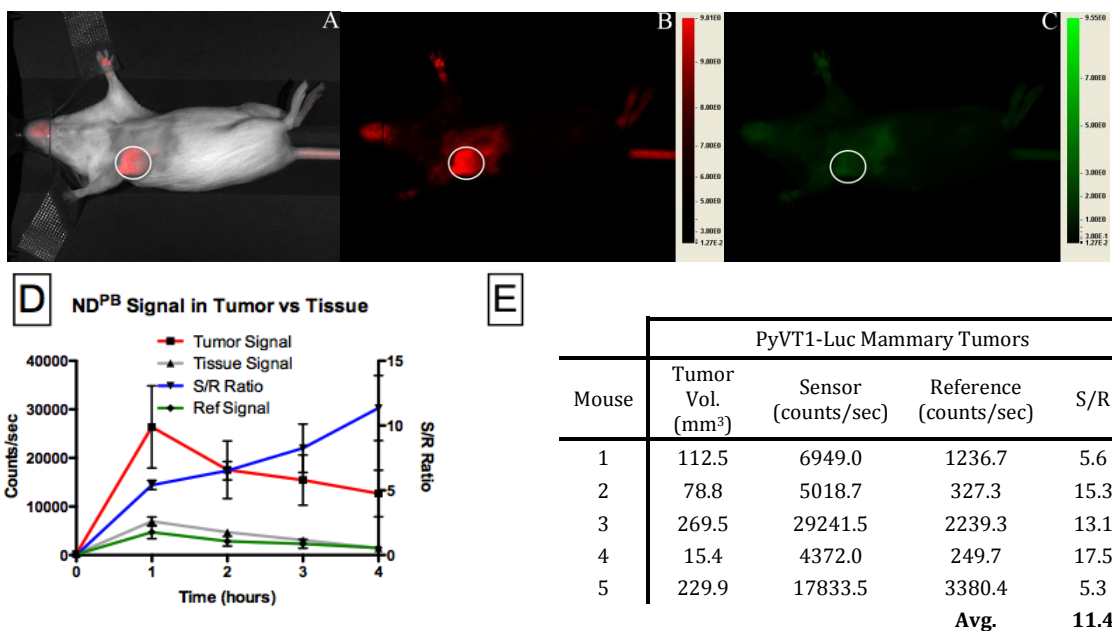
Figure 17: Testing ND^PB in Mouse Models of Breast Cancer

A representative mouse imaged with ND^PB in the visible with overlay, sensor, and reference channels (A-C). ND^PB kinetic properties comparing tumor sensor signal, tissue sensor signal, tumor reference signal, and S/R ratios over 4 hours n=11 (D). Five representative mice were selected and tabulated their tumor volumes, Sensor Signal, Reference Signal, and S/R ratios
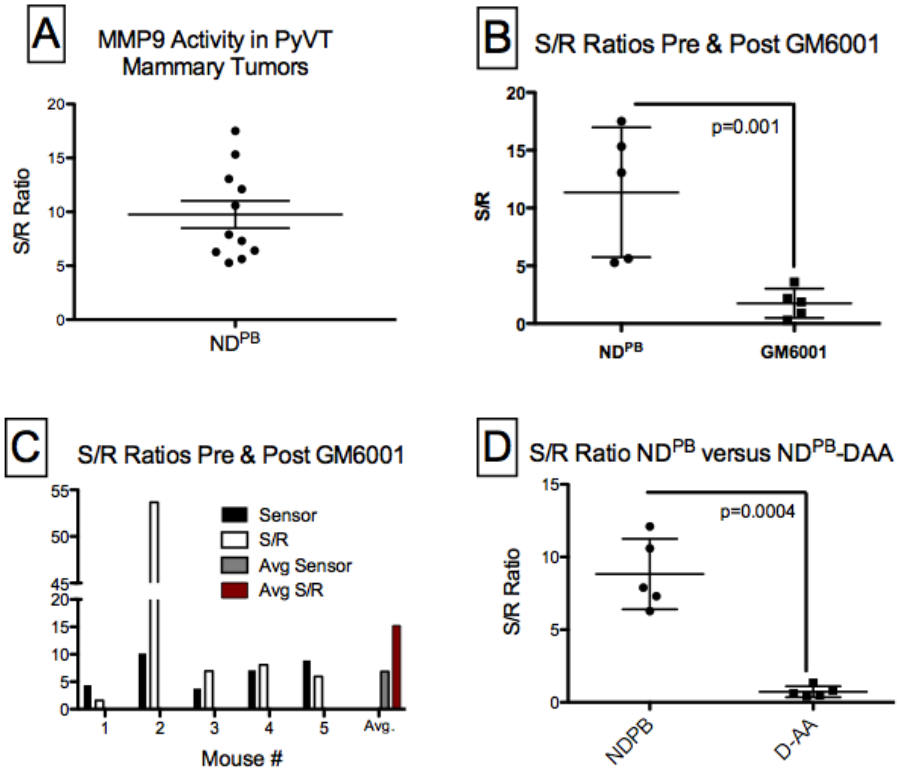
Figure 18: GM6001 MMP Inhibition Detection with ND[PB]
Mice were imaged with ND[PB] containing PyVT1 mammary tumors (n=11, A). Five mice were administered GM6001 for three days and reimaged with ND[PB] (B, C). Five mice were administered ND[PB]-DAA after being imaged with ND[PB] (D). S/R ratios are compared for each group and plotted with averages and standard deviations.

Abraxane Toxicity Study in MMTV-PyVT1-luc Mammary Tumors

PXL based regimens are the current standard of care for early and advanced breast cancer. PXL is an anti-microtubule agent that induces the assembly of tubulin subunits and prevents microtubule depolymerization leading to cell cycle arrest [108]. Abraxane™ is the albumin bound form of PXL and is currently a preferred formulation for this chemotherapeutic in the clinic. Abraxane has been tested on MDA-231 breast cancer cells [108] but to our knowledge has not been evaluated against MMTV-PyVT mammary tumors or derived cell lines. We performed a pilot study with Abraxane at relatively low doses to evaluate if this drug would be effective against the PyVT1-luc tumor cell line. Mammary tumors were established in 7 mice as described above and allowed 11 days to grow. Four mice were then administered 10mg/kg Abraxane for 5 days. Tumor volume was monitored with calipers, cell numbers were evaluated with bioluminescence imaging, and tumor metabolic activity was evaluated with FDG-PET (Figures 19-20). This low dose pilot study provided information regarding the methodology used to evaluate tumor response to therapy. Luminescence imaging demonstrates a reduction in luciferase expression from day 10 to day 17, with recovery quickly establishing by day 25 (Figure 19 B). The control mice luminescence imaging saturates signal by approximately day 17 indicating a problem utilizing this type of imaging for long term treatment studies in animal models of cancer. Tumor volume taken by calipers provides a similar response, however, later time points after day 19 show more significant differences between the control and Abraxane treated animals (Figure 19 C).

99

PET is a highly sensitive and quantitative molecular imaging modality, whose utility in clinical and experimental medicine is based on the assessment of radiolabeled tracer molecules. To date, many types of PET tracers for cancer imaging have been developed. For example, [18F]-2-deoxy-2-fluoro-D-glucose (FDG) is the most widely and successfully used for clinical diagnosis of cancers [86]. FDG monitors glucose metabolism and is applied in staging and diagnosis of cancer, radiotherapy treatment planning, and assessing response to therapy and prognosis. Tumor uptake of FDG tracers is considered to correlate with tumor proliferation, an important feature of tumor malignancy. FDG-PET provided mean standardized uptake values (SUV) for the control and treated animals. FDG was administered to animals 2 days before treatment began, 1 day after treatment, and 14 days post treatment. SUV values were inconclusive as the SUVs did not change significantly during the study and further control animals averaged lower SUV than treated animals (Figure 20).
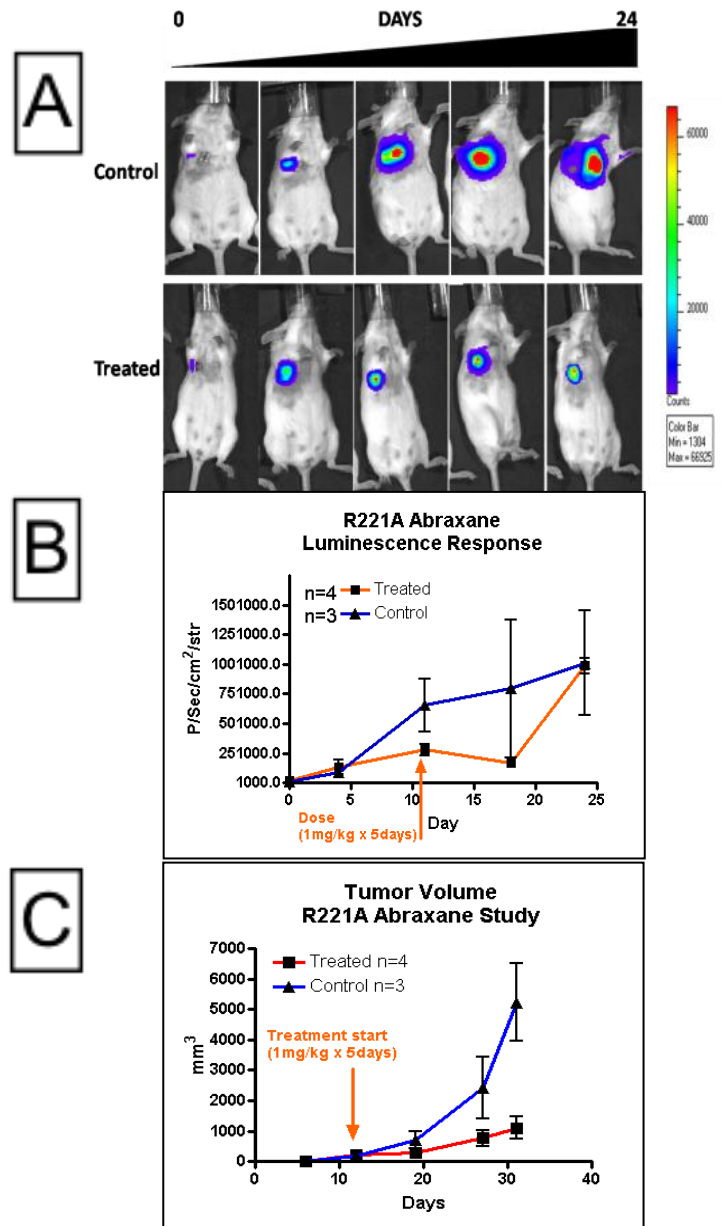
Figure 19: Abraxane Pilot study in FVB-WT mice bearing MMTV-PyVT1-luc mammary tumors
Luminescence was recorded to evaluate tumor cell numbers over time and indicates early response to therapy, but is challenged to differentiate at later time points (A, B). Tumor volume was recorded with digital calipers and demonstrates a better overall response to therapy as the study progresses (C).
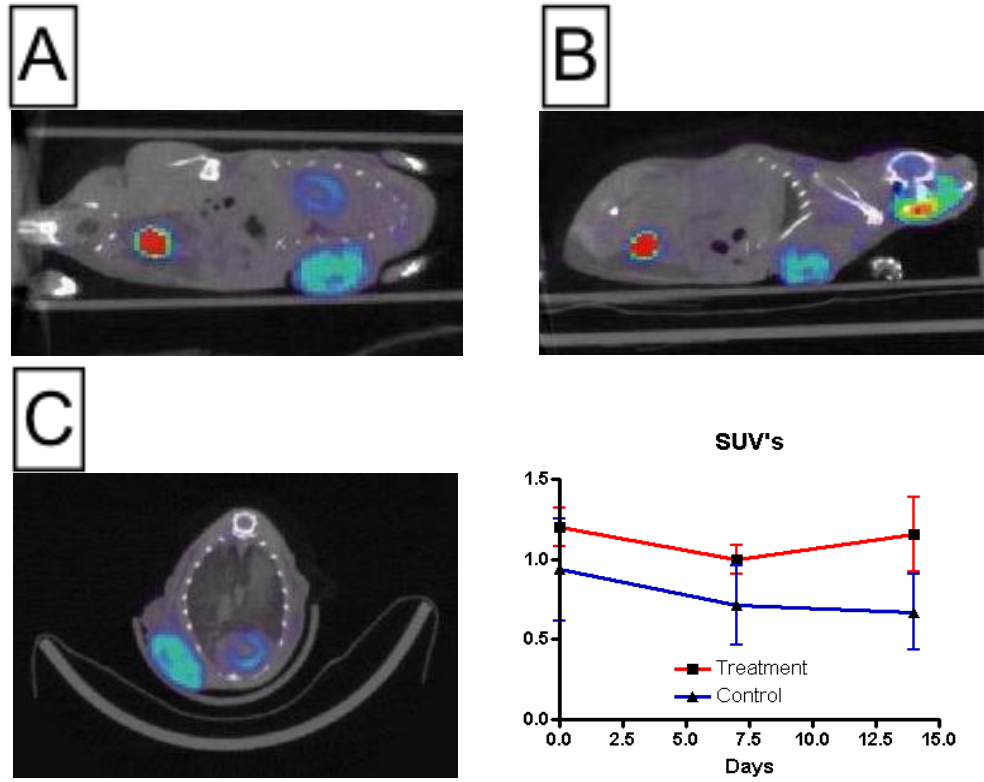
Figure 20: FDG-PET and micro-CT to Monitor Response to Therapy
FDG-PET and micro-CT were performed on all mice in the pilot study n=4 for treated and n=3 controls. PET and CT images overlayed to demonstrate tumor uptake in the coronal, sagital, transverse views (B-C). SUV values were tabulated for each animal using Amide™ software (D).

Synthesis and Characterization of Nanodendron Prodrug ND[Pxl]

Nanodendron prodrug (ND[Pxl]) was constructed on a 2- (benzyloxycarbonyl)-2-methylpropane-1,3-diyl-bis(3-hydroxy-2-(hydroxymethyl)-2-methylpropanoate) dendron (Figure 21, compound (1)) . The dendron is modified by attaching formyl benzoic acid to provide aldehyde groups for oxime ligations between the dendron and the MMP9 substrate (Figure 21, compound (2)). The MMP9 substrate H2N-[AHX]-AVRW*LLTA-[AHX]-DprAOA-Amide was attached in 0.3 M ammonium acetate buffer at pH 4.5 in DMSO with 100 mM concentration of aniline to yield an average of 4 substrates per dendron. The H2N-[Ahx]-AVRWLLTA-[Ahx]-Dendron (Figure 21, compound (3)) was reacted with a PXL derivative, PXL-COOH to complete the prodrug. PXL-COOH was prepared by modification as previously described by Majoros et al. [24] to provide a carboxylic acid linked to the C2 hydroxyl position by reaction with succinic anhydride in methylene chloride to give PXL-COOH. PXL-COOH was coupled to the amine terminus of the peptide-dendron using EDCI and DIEA in anhydrous DMF. The reaction was followed using SEC-HPLC to monitor the disappearance of H2N-[Ahx]-AVRWLLTA-[Ahx]-Dendron and the appearance of a new peak that was eluted from the column earlier than the other peaks, indicating the formation of a larger molecule. The H2N-[Ahx]-AVRWLLTA-[Ahx]-Dendron elutes between 12-17 minutes while after 24 hours, a new peak at 7.5 minutes appeared (Figure 21, compound 5) with no further reaction after 24 hours.
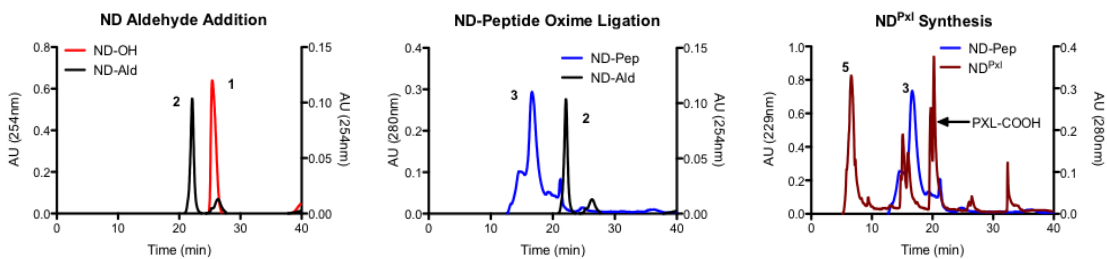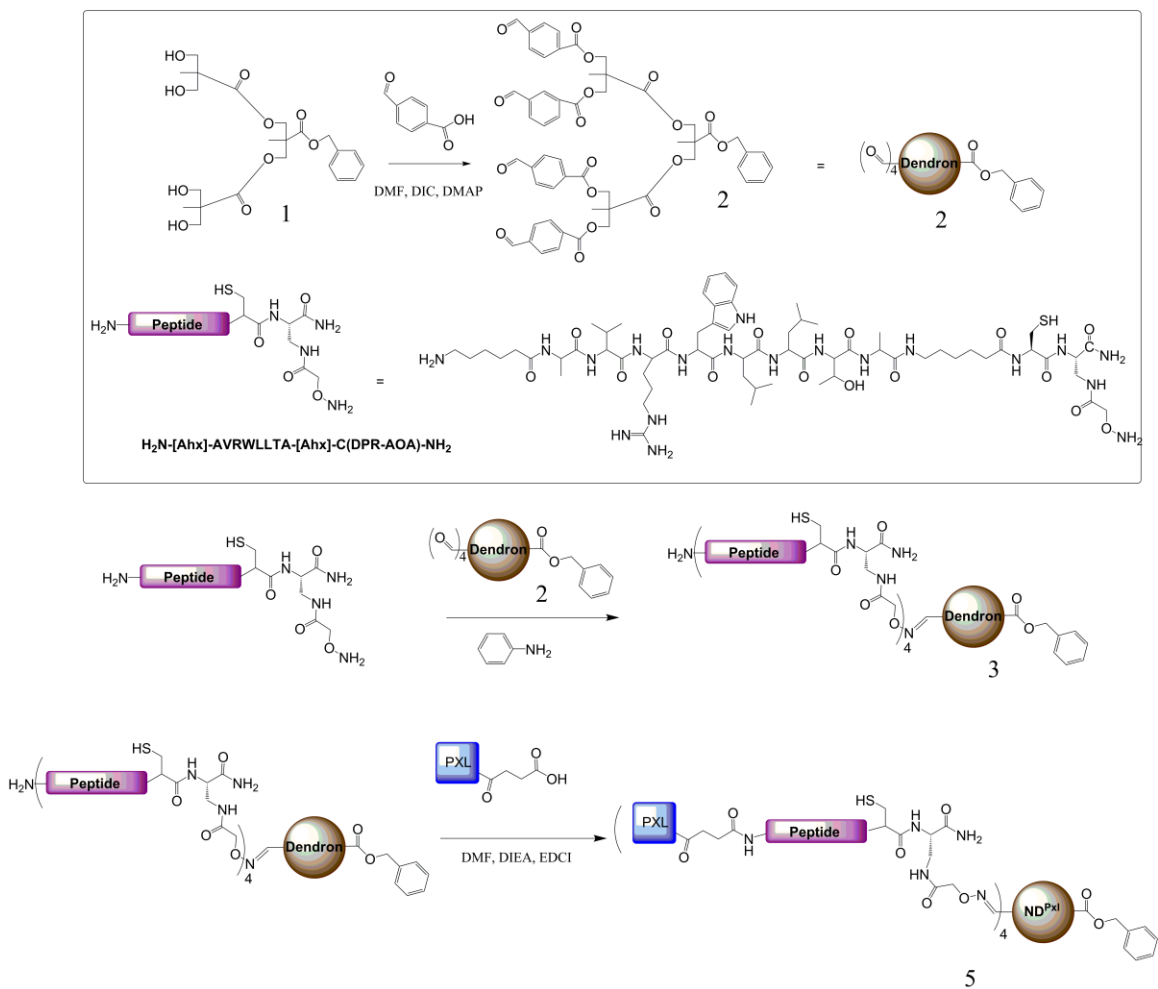
Figure 21: Schematic illustrating the synthetic steps utilized to build ND^Pxl and SEC HPLC traces to validate synthesis of the compound. Refer to numbers throughout the schematic to relate to products found in the SEC HPLC traces

Treatment of PyVT1-luc tumors with ND^{Pxl}

Forty mice were injected with MMTV-PyVT1-luc mammary tumor cells and given one week to establish palpable growths. Luminescence imaging was performed 2 days post injection of the cells to ensure successful injection into the second mammary gland and was utilized therafter to image tumor response to therapy. Mice were randomly divided into 4 groups of 10: Controls, Abraxane at 25 mg PXL/kg, ND^{Pxl} at 12.5 mg PXL/kg, and ND^{Pxl} at 3.13 mg PXL/kg. Abraxane was administered to mice every 4 days for 3 cycles of treatment. ND^{Pxl} was administered every 2 days at the high and low dose for 6 cycles. ND^{Pxl} required 40% DMSO in sterile 0.9% saline to remain in solution at the 12.5 mg/kg concentration. ND^{Pxl} at 3.13mg/kg required 10% DMSO to maintain the compound in solution. Luminescence data plotted over time shows that Abraxane is the only compound to have an effect on bioluminescence as an index of the number of tumor cells (Figure 22, B). It is interesting to note that the volumes recorded by digital calipers tell a much different story; ND^{Pxl} at the 3.13 mg/kg concentration also reduced tumor size (Figure 22, C-E). At ten days post treatment tumor volumes in the control mice average 303mm^3, whereas the Abraxane treated tumors average 65mm^3 indicating a 79% reduction in tumor volume (p=0.005, Figure 22, D) ND^{Pxl} at 3.13mg/kg reduced tumor volumes 58% from 303mm^3 to 129mm^3 (p=0.05), although the higher dose of 12.5mg/kg showed no significant reduction in tumor volume (Figure 22, D). Five days after the last treatment, the gap has widened between the control mice with the Abraxane and ND^{Pxl} 3.13mg/kg groups decreasing tumor volume by 91% from 658mm^3 to 53mm^3 in the Abraxane treated animals (p=0.0001) and by

60% from 658mm^3 to 260mm^3 in the ND^{Pxl} treated animals, p=0.001 (Figure 22 C, E).

FDG-PET was performed at the beginning of the study prior to any treatment and at the end of the study at day 12 (Figure23 A, B). Average values for SUV were calculated pre and post treatment with ND^{Pxl} and abraxane. Control tumors show a large reduction in SUV that could be attributed to necrotic or cystic cores developing in the tumors; this is also a possibility for the 12.5mg/kg ND^{Pxl} group (Figure 23 A). The average SUV for the abraxane treated mice indicates there is little change in SUV values for the group as a whole, however when looking at % change in SUV values for individual mice, there is one mouse in which SUV decreases by 25% and one that increases by 15%. SUV values increase for all animals treated with ND^{Pxl} in both the high and low dose groups (Figure 23 A, B). This data in combination with the FDG-PET done in the abraxane pilot study (Figure 20, 23), indicate that this method of measuring response to therapy in our model of breast cancer is feasible but does not reflect tumor response to therapy using size as a standard.
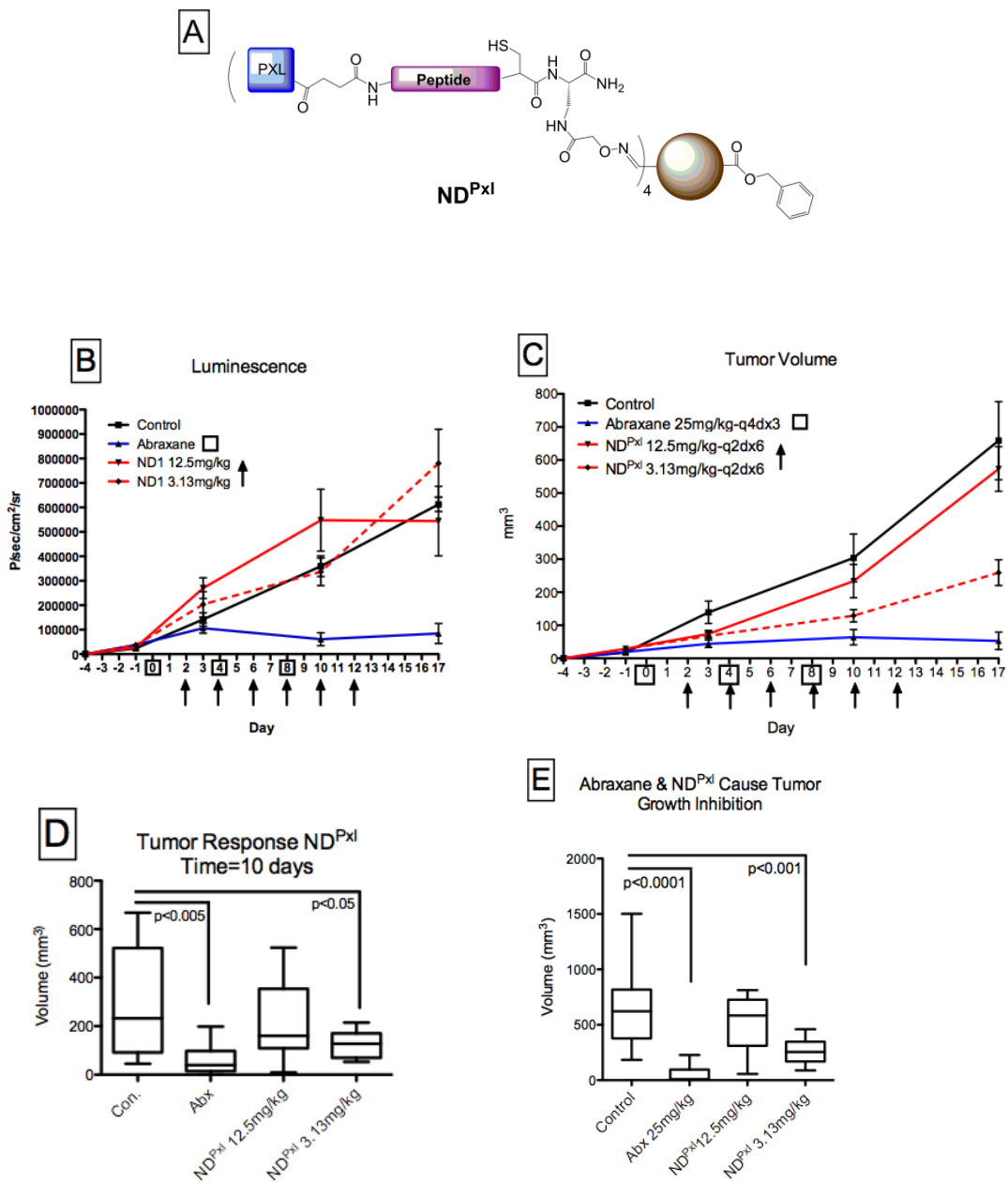
Figure 22: NDPxl study against PyVT1-luc mammary tumors (n=10/group)

Structure of NDPxl (A). Tumor luminescence (mean ± SEM) was monitored to determine cell number over the duration of the study (B). Tumor volume (mean ± SEM) was recorded with digital calipers over the course of the study (C) and indicates an effect in the 25mg/kg Abx group as well as the 3.13mg/kg NDPxl group with p values <0.005 and <0.05 at 10 days post start of the study (D) and <0.0001 and <0.001 for the end point of the study (E), for each group respectively. The box plots (D, E) show the range, mean and standard deviation for each cohort.
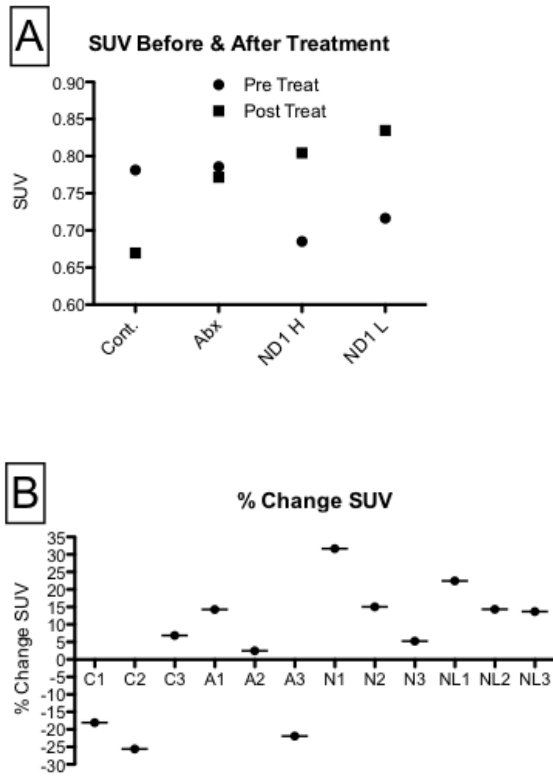
Figure 23: FDG-PET for Response to Treatment Analysis
FDG-PET was used to quantitate average SUV values for three mice from each group pre and post treatment (A). %Change SUV was calculated for each mouse individually with C1-3 being controls, A1-3 abx, N1-3 ND^{Pxl} 12.5mg/kg, and NL1-3 ND^{Pxl} 3.13mg/kg (B)

Generation 3 Nanodendron Prodrug (ND$_3$^{Pxl}) and Proteolytic Beacon (ND$_3$^{PB}):

Design, Synthesis, and Click Reactions

Generation 2 dendrons required 40% DMSO to dissolve the high dose ND^{Pxl}. To improve the solubility of ND^{Pxl}, we first tested increasing the size of the dendron vehicle used to generation 3 (G3) dendrons with 8 versus 4 surface hydroxyls of the G2 dendron. Generation 3 (G3) dendrons with azide and alkyne cores were used to build the second generation of the prodrug and proteolytic beacons (ND$_3$^{Pxl} and ND$_3$^{PB}) (Figure 24 & 25). G3 dendrons were modified by adding formyl benzoic acid using DCC/DMAP coupling in 1:1 methylene chloride:tetrahydrofuran (Figure 24 & 25, compound (7, 11)). This reaction was monitored with SEC HPLC and was purified by flash chromatography. H2N-AHX-AVRWLLTA-AHX-Dpr(AOA)-Amide was then attached to the dendron aldehyde to give an average of 4 equivalents peptide per dendron and monitored with SEC HPLC, giving a new product peak at 14 minutes (Figure 24 & 25, compound (8, 12)).

ND$_3$^{Pxl} and ND$_3$^{PB} were made from H2N-[Ahx]-AVRWLLTA-[Ahx]-C-Dendron. PXL-COOH was coupled to the amine terminus of the azide peptide-dendron using EDCI and DIEA in anhydrous DMF. The reaction was followed using C18 RP-HPLC to monitor the disappearance of H2N-[Ahx]-AVRWLLTA-[Ahx]-C-Dendron and the appearance of a new peak that was eluted from the column between the peptide-dendron and PXL-COOH peaks, indicating that PXL had attached to the peptide dendron to form G3 version of the pro-PXL of ND$_3$^{Pxl} (Figure 24, compound (9)). A total of 8 syntheses were performed to produce enough ND$_3$^{Pxl} for planned animal studies. The alkyne dendron was modified in the exact fashion as described for the

azide dendron, with the substrate including a cysteine for the addition of AF700-NHS ester and AF750 maleimide (Figure 25). An average of four of both fluorophores was attached to each dendron based on absorption spectra. The reaction was monitored with C18 RP-HPLC with a new peak occurring at thirteen minutes with both the 700 and 750 absorbances indicating the formation of the $ND_3{}^{PB}$ optical beacon (Figure 25, compound 13).

$ND_3{}^{Pxl}$ and $ND_3{}^{PB}$ were designed to be linked together to form a single compound $ND_3{}^{Pxl}ND_3{}^{PB}$ via the copper-catalyzed azide-alkyne cycloaddition (CuAAC) reaction "click chemistry" (Figure 26). CuAAC, first reported by Sharpless and coworkers in 2001 [71], has been utilized recently for the functionalization of biological, polymeric, inorganic, and carbon nanoscale objects. Click reactions are reliable and form desired bonds under diverse reaction conditions with no, or conveniently removed, by-products [109]. $ND_3{}^{Pxl}$ and ND^{PB} (Compound 9, 13) were clicked together in DMF with H_2O using tetrakis-(acetonitrile)copper(I) hexafluorophosphate as the Cu(I) source and TBTA as a stabilizing ligand for this reaction [73]. This reaction was monitored with SEC HPLC and C18 HPLC (Data not shown). Absorbance of purified compound indicates the reaction was successful with ~63% yield of $ND^{Pxl}ND^{PB}$ (Figure 26, compound 14). $ND_3{}^{Pxl}$ (compound 9) was also clicked to a non-functionalized alkyne dendron (compound 10) to improve the solubility of the molecule, however the resulting compound it only slightly improved the solubility of the overall construct requiring at least 30% DMSO in saline for solution at 25mg PXL/kg $ND_3{}^{Pxl}D$ (Figure 27, compound 15).
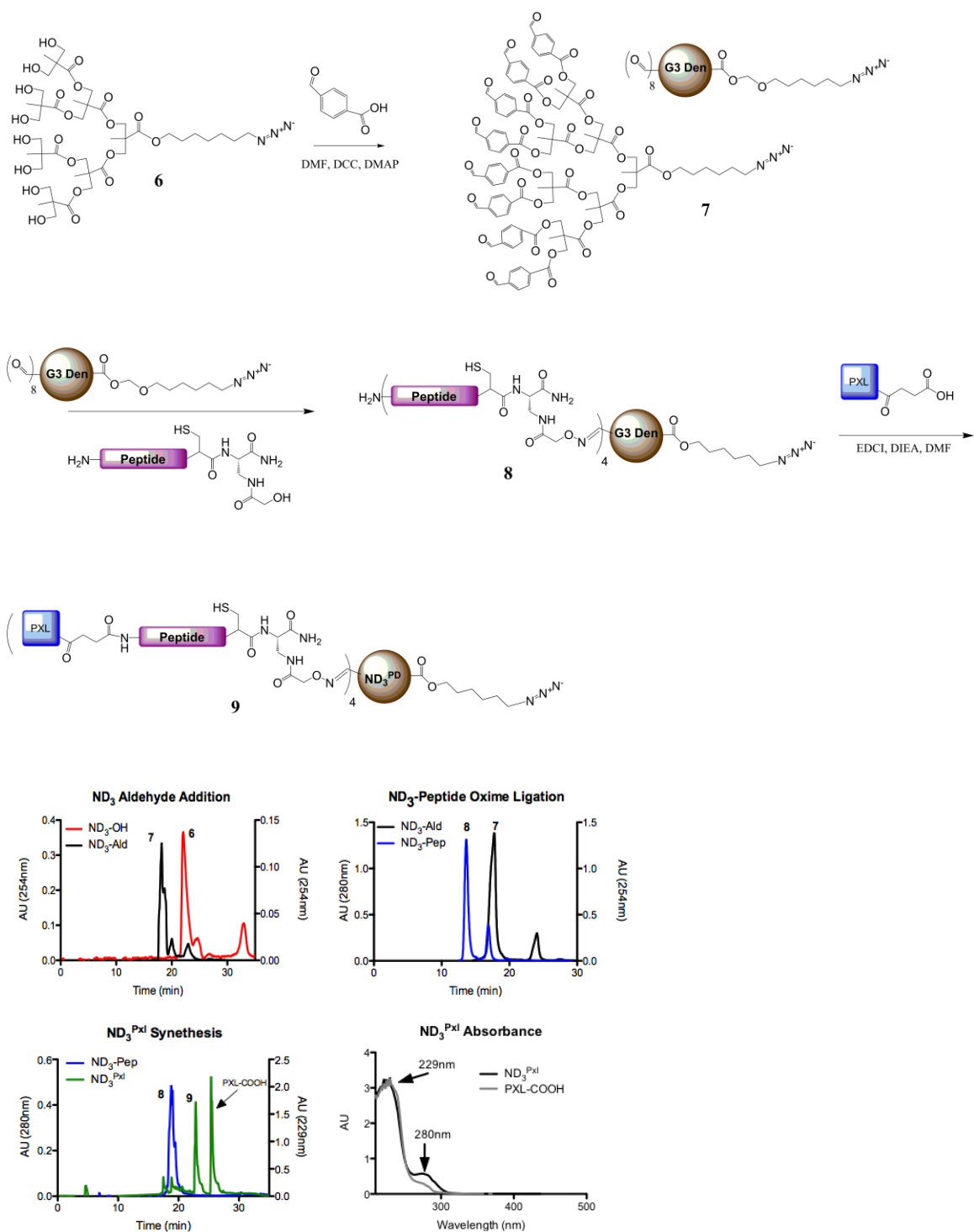
Figure 24: Schematic illustrating the synthesis steps used to build the second formulation ND$_3$^{Pxl} with SEC and C18 HPLC traces to validate synthetic steps
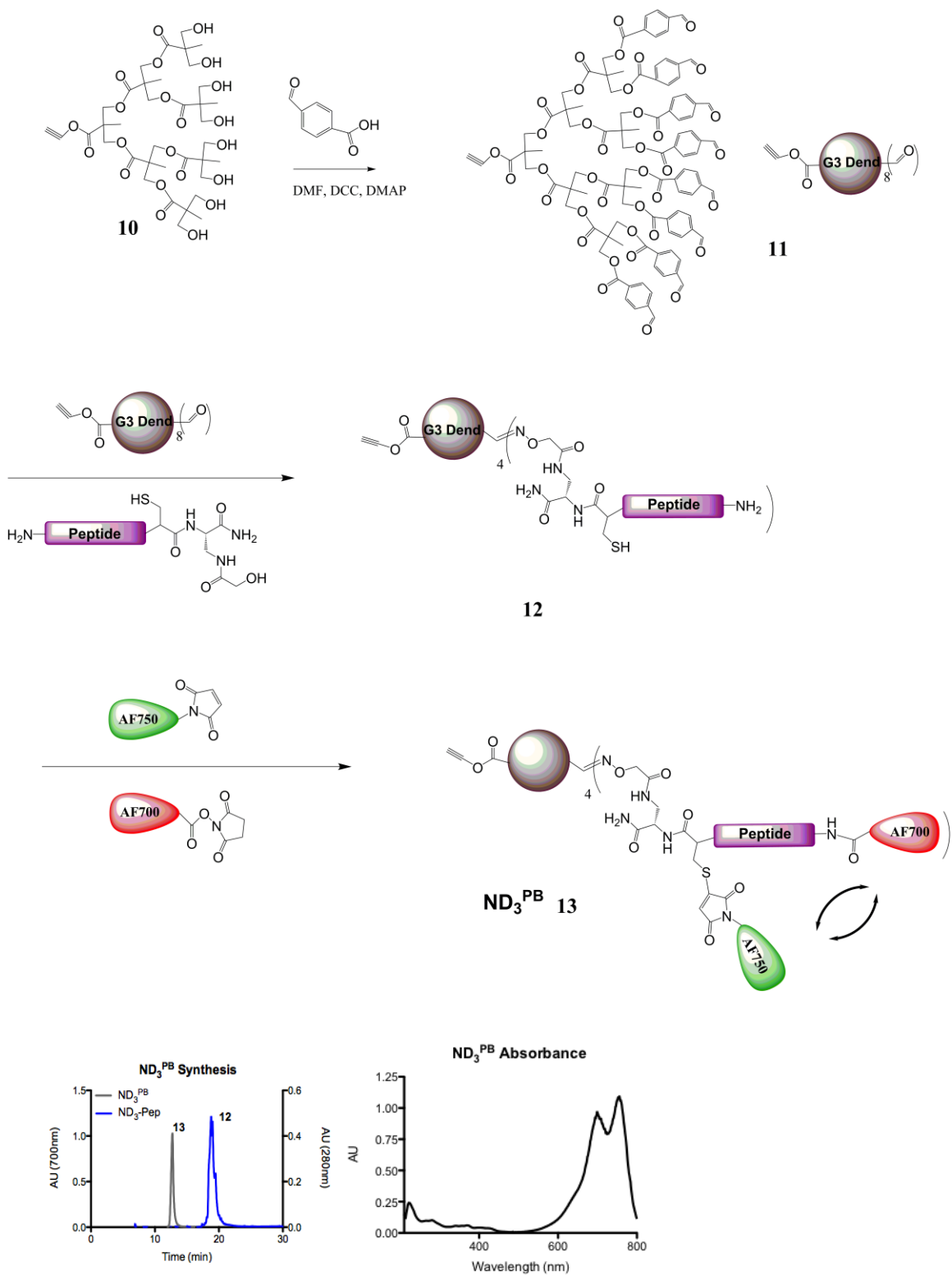
Figure 25: Schematic illustrating the synthesis steps used to build the second generation ND₃^{PB} with SEC and C18 HPLC traces to validate synthetic steps
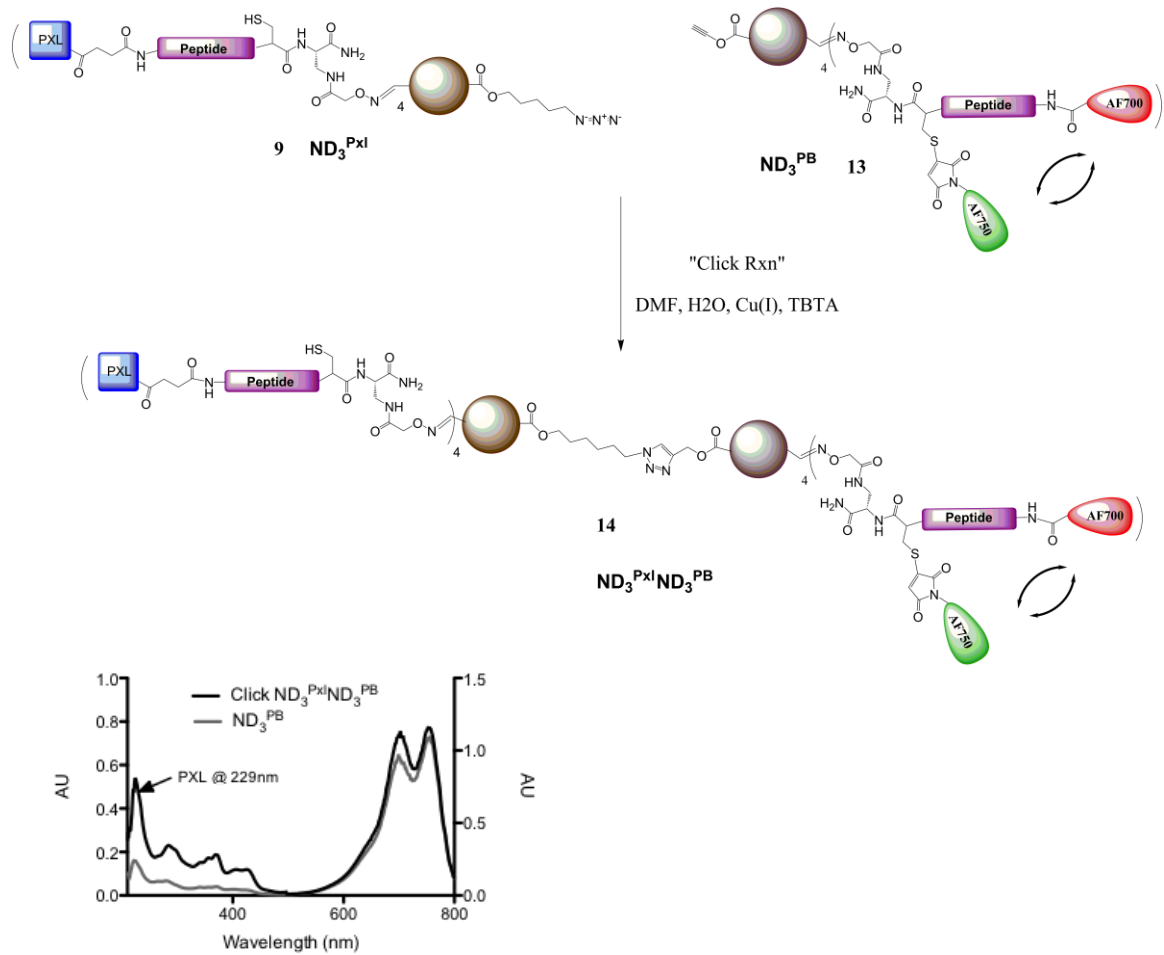
Figure 26: Schematic ND$_3$^{Pxl}ND$_3$^{PB} Click Reaction and Absorbance
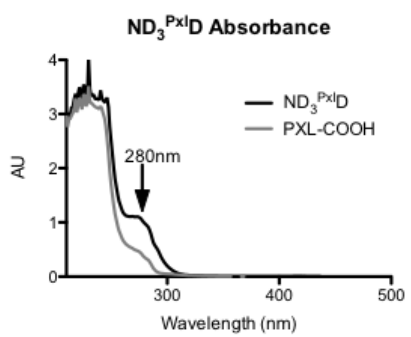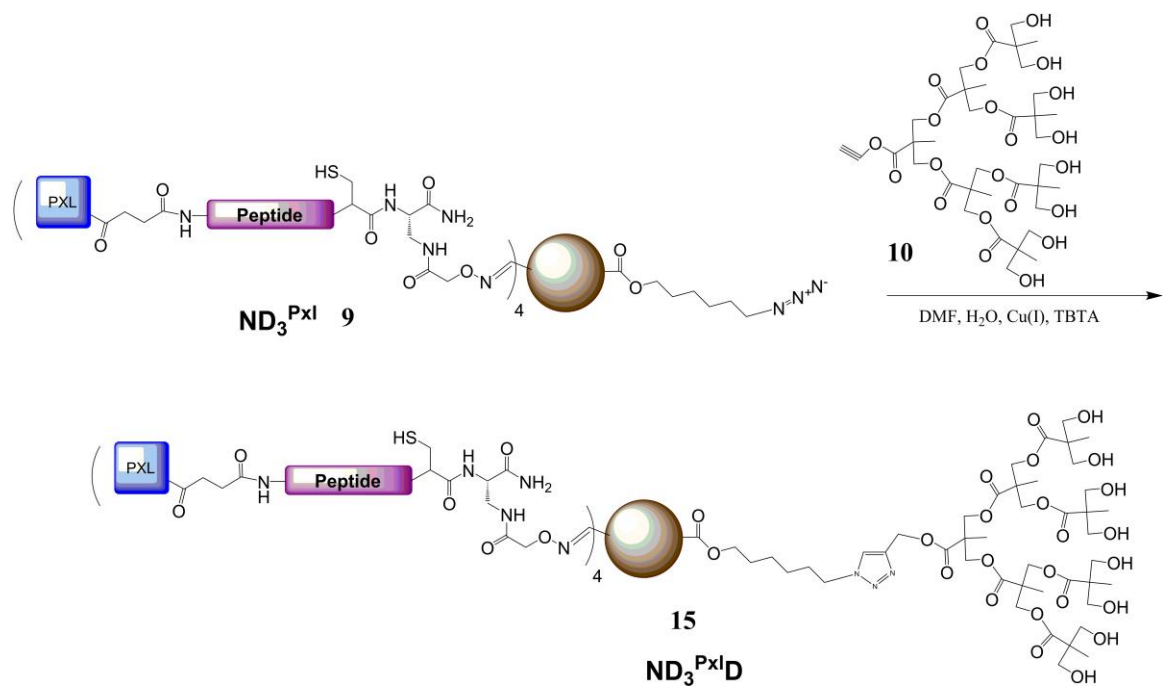
Figure 27: Schematic of ND$_3$^{Pxl}D and Absorbance of Compound

Thirty mice were injected with MMTV-PyVT1-luc cells in mammary gland 2 and given one week to develop palpable tumors. Cell number was monitored with bioluminescence imaging starting 2 days post injection of the breast cancer cells. Tumor volume was recorded with digital calipers. Mice were divided into five groups of five mice each. Five mice were imaged with 1.0nMol of $ND_3^{Pxl}ND_3^{PB}$ in sterile 0.9% saline to determine tumor protease activity and estimate the amount of PXL effectively delivered using this prodrug therapy. Sensor, reference, and S/R ratios were tabulated for these tumors four hours post injection. Sensor signal averaged 3268 in tumor tissue and reference values averaged 405 with S/R ratios approximately 7, n=5. Comparing the S/R ratio to a known concentration of ND^{PB} 100% cleaved in Matrigel indicates 25% of the beacon has been activated in the tumor. Linear regression analysis was performed on these data points to give a formula for % ND cleaved vs. uncleaved sample. Using both phantom studies, sensor signal indicates approximately 25% of proteolytic activation of $ND_3^{Pxl}ND_3^{PB}$. Dosing levels of $ND_3^{Pxl}D$ were determined from this estimate by assuming 100% of PXL is delivered via Abraxane. Abraxane was effective at 12.5 mg/kg retroorbitally, therefore, taking 12.5 mg/kg times 4 (estimated delivery, conservatively) would equal the amount of $ND_3^{Pxl}D$.

Mice were administered saline/DMSO, Abraxane 12.5mg/kg and 4.1mg/kg of PXL, $ND_3^{Pxl}D$ at 25mg/kg, 12.5mg/kg, and 4.1mg/kg PXL. Animals were dosed every two days IP or every day for the 25mg/kg group, as a first round of retro-orbital injections of $ND_3^{Pxl}D$ caused death in 4 mice presumably due to embolism. Tumor

luminescence imaging provides an early indication of response to therapy out to 10 days, but the end point of this study lacked sufficient power to distinguish between responding groups (Figure 29 A, B). Average tumor volumes for each group were plotted over the duration of the study and showed an effective suppression of tumor volume in the ND$_3^{Pxl}$D at 25mg/kg and 12.5mg/kg groups, p<0.05. Average tumor volume for the control mice at day 12 was 1122mm^3 versus 133 and 102mm^3 for the ND$_3^{Pxl}$D at 25mg/kg and 12.5 mg/kg PXL doses, respectively. The lowest dose of ND$_3^{Pxl}$D and both of the Abraxane doses were not significantly different from the control groups. The Abraxane group tumor volume at 12.5mg/kg dose averaged 291mm^3 with the low dose Abraxane group not having much of a response at 1005mm^3. The 4.1mg/kg dose of ND$_3^{Pxl}$D had a similar effect as the Abraxane group at 12.5 mg/kg with an average tumor volume of 500mm^3. Tumor growth inhibition (TGI) was calculated for each group with ND$_3^{Pxl}$D having 88, 91, and 55% for each dose respectively with Abraxane TGI at 74.0, and 10.4% for the 12.5 and 4.1mg/kg doses. The same dose of PXL is therefore more effective in inhibiting tumor growth when administered IP as ND$_3^{Pxl}$D (90.9%) compared to Abraxane (74.0%).

FDG-PET analysis was performed on 3 animals from the control, ND$_3^{Pxl}$D 25 and 12.5mg/kg, and the Abraxane 12.5mg/kg groups. Coronal images are shown for the control, ND$_3^{Pxl}$D 25mg/kg, and Abx 12.5mg/kg groups, and demonstrate that tumor activity is relatively low in the treated groups. However, calculated SUV values are difficult to interpret.
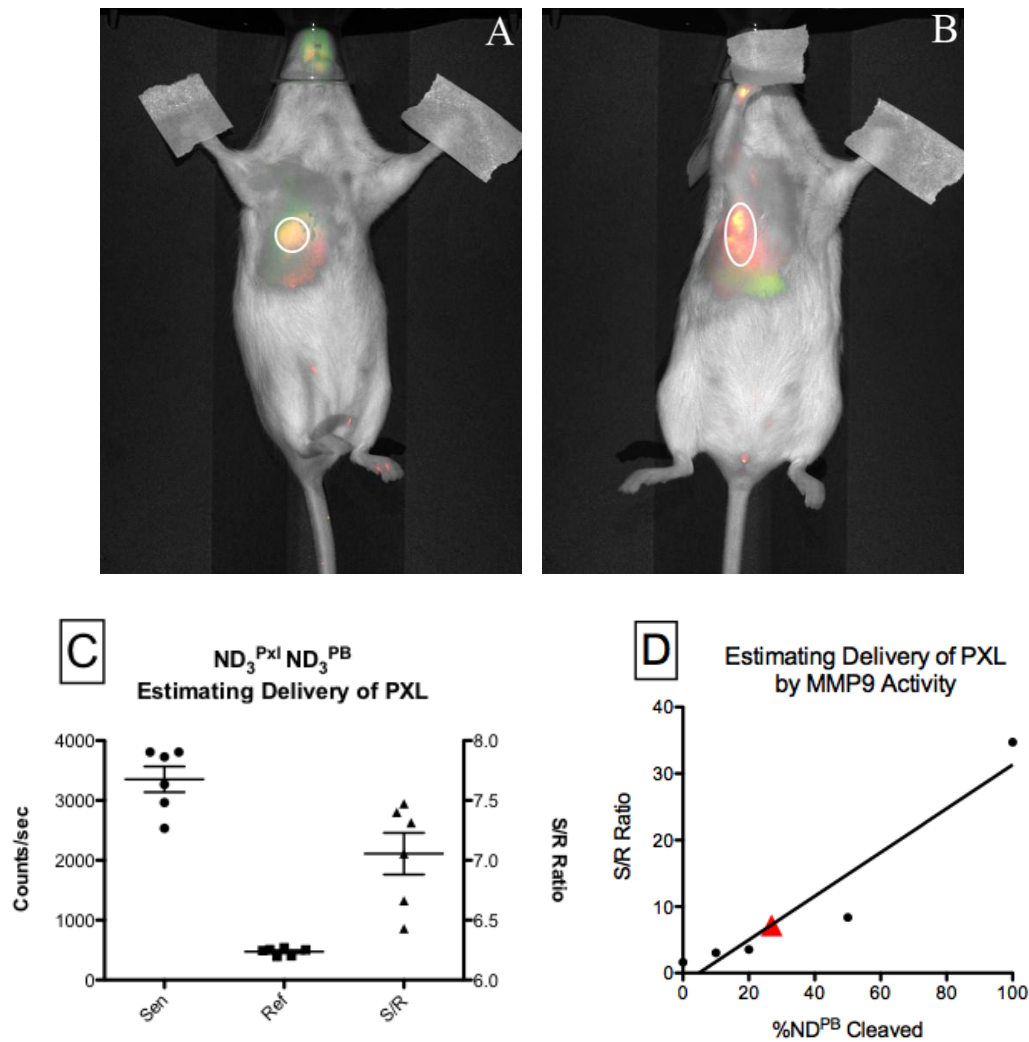
Figure 28: Using ND₃^PxlND₃^PB to estimate delivery of therapy and tumor protease activity
1.0nMoles of ND₃^PxlND₃^PB was administered retro-orbitally to FVB-WT mice bearing PyVT1-luc tumors that were averaged ~ 100mm³ (A & B). Sensor, reference, and S/R ratios were tabulated for these mice and then compared to phantom concentration curves from earlier studies (C). Linear regression analysis was performed to give the equation y=0.33x-1.6 (y=counts/sec; x=%ND cleaved), giving an estimated approximate delivery of 25% of PXL based on ND^PB activity (D).
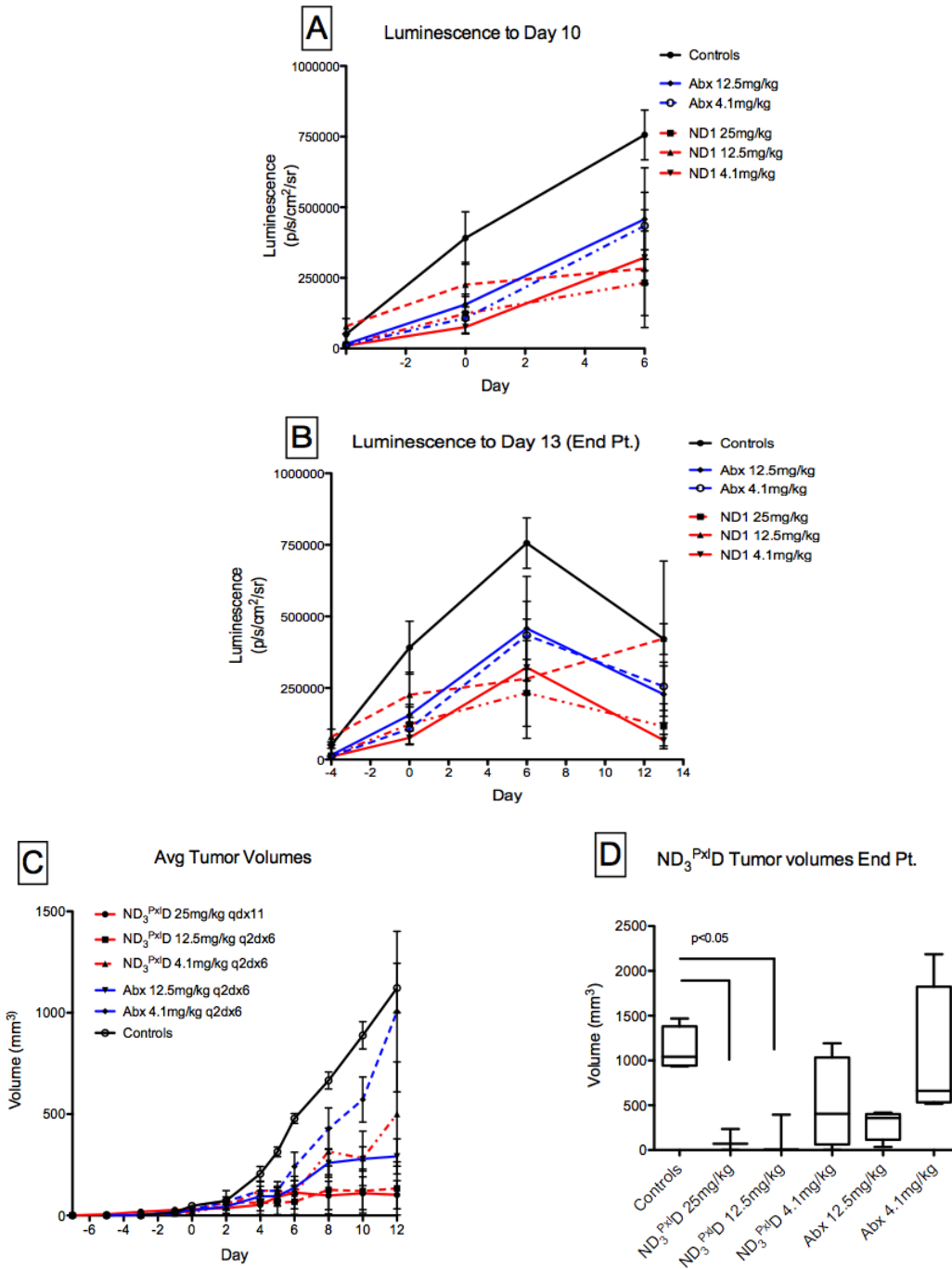
Figure 29: ND$_3$^{Pxl}D Toxicity study versus PyVT1-luc mammary tumors in FVB-WT mice: Tumor Luminescence provides an early indication of response versus the PyVT1-luc mammary tumors at day 10 (A). By the end point of the study, luminescence is not capable of differentiating between groups (B). Average tumor volumes were recorded over the duration of the experiment with digital calipers (C). Box and Whiskers plot displaying the mean, max and min values for tumors in each group. Tumor growth suppression is significant for the ND$_3$^{Pxl}D 25 and 12.5mg/kg groups with p values <0.05 (C)
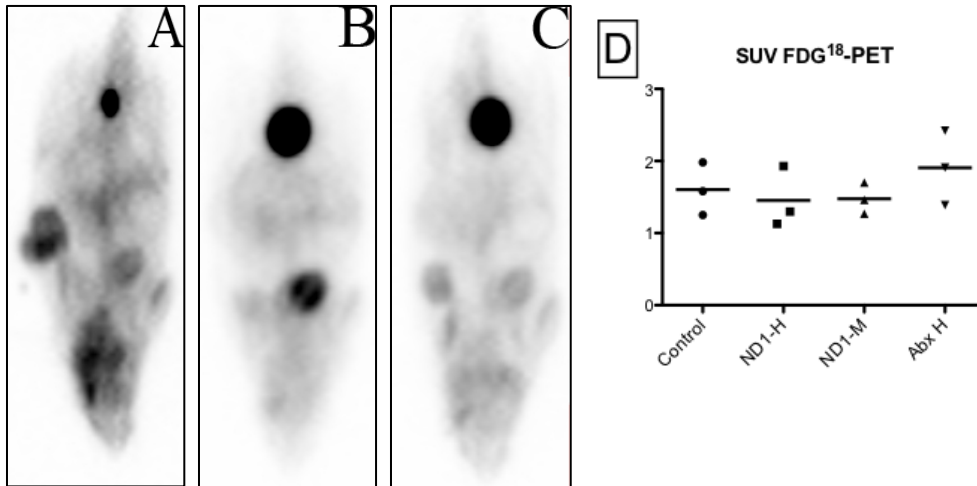
Figure 30: FDG-PET analysis was performed on 3 mice from the control, $ND_3^{Pxl}D$ 25 and 12.5mg/kg groups, as well as the 12.5mg/kg Abraxane group. SUV values were tabulated for these groups and indicate a lower SUV value trend that may be occurring in animals that respond to treatment, though differences are not significant. Coronal images of single mice from the control (A), $ND_3^{Pxl}D$ 25mg/kg (B), and Abx 12.5 mg/kg groups (C) summing the total SUV values not the low tumor uptake in the $ND_3^{Pxl}D$ 25mg/kg group as compared to the control and Abx treated animals (D).

Peripheral Neuropathy Analysis

PXL dosing regimes in the clinic are often limited by the peripheral neuropathy side effects that develop. An overarching goal of ND^{Pxl} and ND$_3$^{Pxl}D is to reduce the side effects of PXL by delivering the drug selectively to tissues expressing MMP9. Mice in selected cohorts from the final study were evaluated and scored for tests that evaluate aspects of the nervous system. The results of two of these studies are displayed in Figure 31 and trend towards improvements with the ND$_3$^{Pxl}D treated animals. Rotorod and hot plate analysis on each group suggests that the ND$_3$^{Pxl} therapies are trending towards a reduction in peripheral neuropathy. Mice in the Abraxane 12.5 mg/kg group trended towards worse performed in all studies than mice from other groups, suggesting that ND^{Pxl} therapy may provide a means to reduce the side effects of PXL therapy.
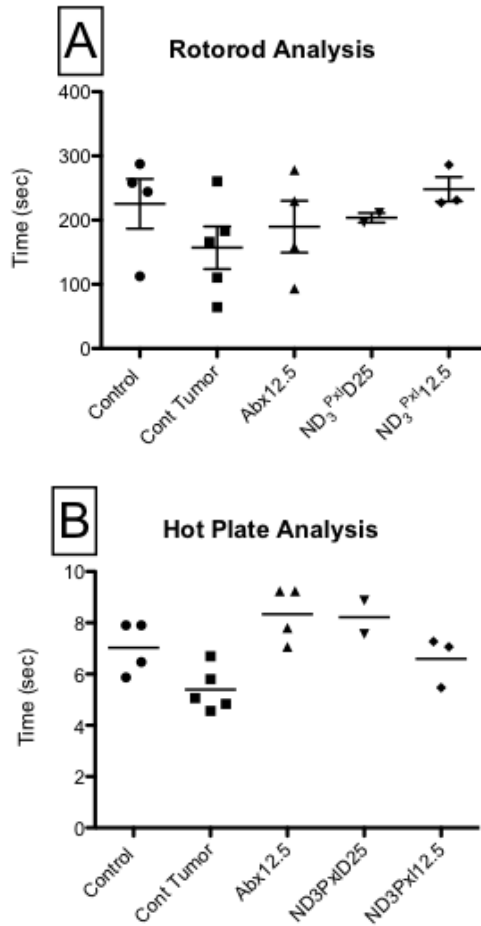
Figure 31: Rotorod and Hot Plate Analysis Testing PXL's Side Effects
Rotorod analysis and Hot Plate analysis was performed on each group 2 days after the last dose in triplicate for each animal (n=4 for controls and Abx, n=3 for $ND_3{}^{Pxl}D$ treated). Shorter time periods of performance are indicators of poor response and neurological side-effects (A) Hot plate analysis was performed at 55°C in triplicate for each animal and average time on the hot plate is plotted for each group (B). With the hot plate test, longer lag times indicate nerve damage. (Controls without tumor n=4, controls with tumor n=5, Abraxane at 12.5mg/kg n=4, $ND_3{}^{Pxl}D$ at 25mg/kg n=2, $ND_3{}^{Pxl}D$ 12.5 mg/kg n=3)

Conclusions

There is an overwhelming need for the development of compounds that are capable of early detection of metastatic disease and personalized medicine to treat these lesions in a manner that reduces side effects. This chapter focuses on an approach to build and test multifunctional nanoparticles that can be linked in various manners to detect and treat breast cancer in mouse models. The development of a novel synthetic route to build a new generation of proteolytic beacons was achieved and successfully tested in animal models. Using this synthetic knowledge, a prodrug therapy was developed with the goal to enhance therapy and minimize the side effects of PXL. The first compound of ND^{Pxl} has some solubility issues that were somewhat remedied in the second version of the compounds. However, adverse outcomes from retro-orbital injection of $ND_3^{Pxl}D$ dictated testing this compound by IP injectin. The second compound, $ND_3^{Pxl}D$, demonstrates the effective inhibition of tumor growth and performs better than the current standard of PXL administration Abraxane. Preliminary tests for peripheral neuropathy suggest that our new formulation of PXL as an MMP-activated prodrug may alleviate peripheral neuropathy in treated animals. Our studies suggest that this is a step towards personalized medicine that will improve therapies geared towards treating metastatic disease by targeting MMPs.

CHAPTER V

DISCUSSION, FUTURE DIRECTIONS, AND CONCLUSIONS

<u>Discussion</u>

Optical Imaging of MMP7 Activity In Vivo Using a Proteolytic Nanobeacon

Non-invasive imaging techniques provide an extraordinary opportunity for the molecular imaging of cancer. PB-M7NIR is an enhanced version of a previously developed proteolytic nanobeacon built on a commercially available dendrimer scaffold with peptide switches selective for cleavage by MMP7 and optical sensors based on FRET [80]. PB-M7NIR improves upon this previous work by utilizing near-infrared sensor and reference fluorochromes to increase the efficiency of light traveling through tissue[110]. The inclusion of an internal reference fluorophore also allows for the detection of both the un-cleaved and cleaved reagent facilitating quantitative analysis and providing a much-needed means to evaluate protease activity. We have demonstrated the ability of the proteolytic nanobeacon to selectively assess MMP activity using models that either over-express or eliminate endogenous MMP7 activity, while the efficiency of PB-M7NIR at detecting the relatively small areas of protease activity in the APC[Min] model demonstrates the applicability of this technology for the early detection of pre-malignant lesions.

The PB-M7NIR reagent described in the present study is comparable to proteinase activated NIR probes developed by Weissleder and co-workers [100, 111],

but PB-M7NIR differs from the graft co-polymer based reagents in the PAMAM dendrimer scaffold utilized as the vehicle for circulation and in the use of both sensor and reference fluorophores. PAMAM dendrimers have well-defined structures that facilitate flexibility to improve the overall bioavailability of the fluorogenically labeled peptide substrates and enhance its sensitivity [112]. PB-M7NIR relies on quenching of sensor fluorophores by both homotransfer self-quenching and FRET with the internal reference fluorophores. The internal reference fluorophore provides quantitative analysis of the concentration of the substrate and is useful to evaluate the pharmacokinetics of PB-M7NIR. We showed that the S/R ratios of PB-M7NIR is a useful indicator of relative MMP7 activity *in vivo,* but agents such as this may be able to assess absolute levels of MMPs in normal and diseased tissue. Our further studies focus on absolute quantitative measurements of MMP activity by agents like PB-M7NIR that could be applied to human tumors.

In vivo imaging of subcutaneous xenograft tumors using PB-M7NIR showed selective imaging of MMP7 activity. In these studies, both xenograft tumors were derived from the same SW480 human colon cancer cell line expressing several MMP family members [113] and only differing in the overexpression of MMP7 in the SW480mat cells. They were injected on opposite sides of the same animal to maintain similar tumor environments and minimize animal-to-animal variation. Accumulation of biocompatible macromolecules has been reported for a variety of solid tissue tumors due to the enhanced permeability and retention effect of probes in the tumor due to leaky and constricted vasculature [114, 115]. The SW480 mat and neo tumors develop with consistent sizes and masses and have been shown by

histological analysis to show no significant differences in vasculature [116]. Therefore, the SW480neo xenograft tumors serve as an appropriate control for the SW480mat xenograft tumors from a physiological perspective. It is noted that, although the SW480neo control cells express undetectable levels of MMP7 mRNA and protein in culture [116], MMP7 can be contributed by infiltrating inflammatory cells [117]. Variable levels of these host bone-marrow-derived inflammatory cells in the SW480 neo tumors may account for the variability in S/R ratios seen in tumors from the present study, and the modest average enhancement of signal in the expressing vs. non-expressing xenograft tumors as compared with the much larger difference in APC^{Min} mice with and without MMP7 expression. Host MMP7 activity can be eliminated by the use of MMP7-deficient mice, as in the APC^{Min}-7-null mice, but become more complicated for the xenograft studies that would require concomitant inactivation of the immune system to accept the human tumor xenografts.

When evaluating PB-M7NIR cleavage by MMP7 in the xenograft tumors, S/R ratios were much higher in the *ex vivo* sections than the S/R ratios seen *in vivo*, most likely due to the lack of the absorption properties of tissue and attenuation of signal due to depth of the source. The S/R ratios seen in the sections serve to localize the activation of PB-M7NIR at the cellular level, although only a small fraction of the tumor can be imaged at one time. MMP7 was found to be localized at the tumor boundary, corresponding to previous data showing MMP7 activity in macrophages [117, 118], vascular endothelial cells adjacent to the tumor [119], and mononuclear phagocytes [120]. Although some MMP7 activity was found within the xenograft tumors, results suggest that MMP7 predominately cleaves PB-M7NIR at the tumor-

stroma interface with high activity being detected in the dermal ECM. The results suggest that MMP7 physically associates with ECM components in an active form. MMP7 may be associated with its substrates, such as the proteoglycan versican or tenascin-C (2), both which can be found in non-basement membrane matrices.

The APC[Min] mouse provides an ideal model for evaluating the sensitivity of PB-M7NIR due to the large number of adenomas that develop in the intestinal tract at various sizes. APC[Min] mice have a mutation in the adenomatous polyposis coli gene that predisposes them to develop multiple benign adenomas throughout the entire intestinal tract at an early age, mimicking the human condition Familial Adenomatous Polyposis Coli [121]. The adenomas express the mRNA for several MMP family members, most notably MMP7, which localizes to the epithelial component of the tumors [42, 90]. MMP7 expression has been reported in early-stage, benign tumors of the gastrointestinal (GI) tract [43], and reduction in MMP7 activity specifically [90] or MMP activity generally [122] reduces the number of polyps suggesting that MMP7 represents an appropriate target for prevention strategies [123]. PB-M7NIR was found to show significant sensor signal in *ex vivo* imaged adenomas as small as 0.01 cm^2 with S/R ratios being independent of tumor size. This size tumor is very difficult to detect with white light, suggesting that PB-M7NIR could be applied to enhance the detection of very small intestinal adenomas by colonoscopy. The specificity of PB-M7NIR was also demonstrated by the significant reduction in signal in all polyps of APC[Min]-MMP7-null mice compared to APC[Min] mice. It is not currently clear if MMP-based PBs can be sufficiently quantitative to be useful for prognostic significance, for example in distinguishing benign from malignant tumors. This application may

require an absolute difference, the presence or absence of a specific MMP, rather than an alteration in the levels of expression and/or activation to be feasible.

Sagital sections of intestinal adenomas from APC[Min] mice found effective localization of MMP7 in the epithelial compartment of the adenomas that correspond to histochemical analysis using an MMP7 antibody. At the subcellular level, we observed MMP7 staining in the basolateral region of the tumor cells. However, MMP7 activity appeared to be present throughout the cell. It is not clear if this represents the distribution of active MMP7 and/or the distribution of the product throughout the cell. It is interesting that the signal did not localize to the basement membrane or ECM between glands in the adenomas, in contrast to the abundant ECM staining in the stroma surrounding the subcutaneous tumors. This may be a result of the extreme loss of polarity with the SW480 colon carcinoma cells compared to the benign adenomas, since in cultured polarized epithelial cells MMP7 activity is primarily localized to the apical compartment [124]. It is also interesting that the MMP7-attributable signal is enhanced approximately 300-fold in the xenograft tissues compared to the 6-fold enhancement in the intestinal tissues. Factors that may contribute to this difference include the overexpression of MMP7 in the SW480mat tumor cells compared to the endogenous levels of MMP7 in the adenomas, the more abundant ECM in the dermis compared to the intestine, and the possibility that there is selective retention of either the enzyme or PB-M7NIR proteolytic products by an ECM component that is differentially expressed in these tissues. Additional studies using high-resolution multi-photon microscopy are currently underway to assist in addressing these possibilities.

Mix-&-Match Nanodendrons for Detection and Treatment of Breast Cancer Metastases

A new class of nanoparticle-based imaging and therapeutic compounds has been developed with molecular recognition and targeting capabilities. These nanoparticles have been designed with the ability to link together in various combinations for multifunctional purposes in early detection and targeted treatment of metastatic breast cancer. The development of this novel class of NDs expands upon the current capabilities of modern proteinase-based optical beacons and prodrugs, and is a step towards developing personalized medicine. The PB and PD reagents described in this study (ND^{Pxl} and ND^{PB}) are comparable to proteinase-activated NIR probes [refer to chapter 3, [57, 80]] differing by utilizing biocompatible polyester dendrons and with targeting toward MMP9 rather than MMP7. The functionalized versions of ND^{Pxl} and ND^{PB} built on dendron scaffolds allow for quantitative and selective component additions required to synthesize nano-related compounds. These final compounds have internal cores that can be modified in a manner to allow linkage of ND^{Pxl} and ND^{PB} together and could be modified further to include other functionalities. The use of dendron scaffolds also improves the specificity when building functionalized nanomaterials by having known reactive sites for specific positioning of components when building prodrugs or proteolytic beacons. This is one major difference from previous compounds built on PAMAM scaffolds.

Imaging MMP9 Activity with ND[PB]'s

ND[PB] and ND$_3$[PB] rely on quenching of sensor fluorophores by both homotransfer self-quenching and FRET with the internal reference fluorophores. We tested a set of six FRET pairs using the LI-COR PEARL® imaging system to determine the most effective fluorophore pair to be utilized in building ND[PB]. It is important to note that optimization is based on this system and may not reflect total FRET properties of these dyes or their performance with other linking platforms. The internal reference fluorophore, AF750, provided quantitative analysis of the concentration of the substrate and was useful to evaluate the pharmacokinetics of ND[PB]'s. We also built the D-amino acid (D-AA) version of ND[PB], which cannot be cleaved enzymatically, and used this compound to confirm that ND[PB] is activated via MMP proteolytic cleavage. We showed that the S/R ratios of ND[PB] is a useful indicator of relative MMP9 activity *in vivo* and improved the overall FRET of this molecular probe from our previous generation of beacons by moving the donor and acceptor pairs closer together. *In vivo* studies with ND[PB] investigate the limits of detection for this optical agent using phantoms containing the MMP9 cleaved version of this probe. ND[PB] cleaved by MMP9, and uncleaved controls of ND[PB] with EDTA, and ND[PB]-DAA were injected in mice and demonstrated the ability to detect ND[PB] at levels down to 0.1 μM of the activated probe. Developing concentration curves and incorporating ND[PB]-DAA with the cleaved version of ND[PB] provided the ability to generate a standard curve that was used to estimate proteolytic activity at tumor and diseased tissue sites. Thus, we are able to evaluate specific tumors to

determine if prodrug therapy would be an effective means of treatment and estimate delivered doses of prodrug therapies.

Some tumors did not express significant MMP9 activity while others had robust activity as detected with ND[PB] (Figure 16 p. 94). Thus, this approach allows for selection of specific tumors (or patients) who are likely to respond to MMP9-activated prodrug therapy. *In vivo* imaging of subcutaneous xenograft tumors using ND[PB] showed selective imaging of MMP9 activity. In these studies, both xenograft tumors were derived from the same LLC cancer cell line and express several MMP family members but differed only in the over-expression of recombinant MMP9 in the LLC-MMP9 positive cells ([92], unpublished data). MMP9 positive and negative cells were injected on opposite sides of the same animal to maintain similar tumor environments and minimize animal-to-animal variation. Accumulation of biocompatible macromolecules has been reported for a variety of solid tissue tumors due to the enhanced permeability and retention effect of probes in the tumor due to leaky and constricted vasculature [114, 115]. The LLC-MMP9 (+) and MMP9 (-) tumors develop with consistent sizes and masses. Therefore, the LLC-MMP9 (-) xenograft tumors serve as an appropriate control for the LLC-MMP9 (+) xenograft tumors. It is noted that, although the LLC-MMP9 (-) control cells express undetectable levels of MMP9 mRNA and protein in culture but in both tumors [LLC-MMP9 (+) and LLC-MMP9 (-)] MMP9 can be contributed by infiltrating inflammatory cells [117]. Variable levels of these host bone-marrow-derived inflammatory cells in the LLC-MMP9 negative tumors may account for the variability in S/R ratios seen in tumors from the ND[PB] studies. Also these cell lines

are known for their anti-angiogenic nature [107] which could reflect the lower levels of activity detected in these tumors in comparison to the mammary tumors described below.

The Matrisian laboratory isolated and characterized a series of cell lines from primary tumors in MMTV-PyVT FVB mice [28]. The highly aggressive PyVT antigen/E-cadherin positive cell line, MMTV-PyVT1, form compact, rapidly growing unifocal tumors in the mammary fat pad of syngeneic FVB mice. The morphology of these tumors is consistent with the poorly differentiated component within spontaneously formed MMTV-PyVT mammary tumors [26, 27]. For *in vivo* studies, MMTV-PyVT cells were modified to express luciferase deriving PyVT1-luc cells (51). These cells are known to express MMP9 (personal communication) and in combination with the FVB mouse model provided an ideal model to study ND[PB's] and ND[Pxl's].

In vivo imaging of PyVT1-luc mammary tumors using ND[PB] demonstrate the ability to image MMP9 activity in this model. S/R ratios were higher in this model than in the LLC xenograft tumors and may be attributed to the different vascular networks within these tumors as well as the fully intact immune system of the FVB mice that will provide infiltrating inflammatory cells that produce MMP9. We tested the ability of ND[PB] to detect the inhibition of proteinase activity by treating mice with GM6001 (a broad spectrum MMP inhibitor) for three days and imaged before and after with ND[PB]. The initial ND[PB] response is significantly higher than after 3 cycles of GM6001 treatment (6.6 fold reduction in signal p<0.0001). Further demonstration that ND[PB] was imaging MMP activity was provided by the

observation that the D-AA version (ND^{PB}-DAA) generated no detectable signal and maintained low S/R ratios in mice with mammary tumors. This data demonstrated that the D-AA version of the MMP9 substrate will act as an ideal control for future studies involving prodrug deliveries.

Monitoring and delivery of MMP-Activated PXL to Mammary Tumors

ND^{Pxl} and ND$_3$^{Pxl} are novel nanoparticle based prodrugs that are designed to specifically release a cytotoxic chemotherapeutic, PXL, in the vicinity of tumors or metastatic tumor cells expressing MMP9 to reduce concomitant side effects on normal cells. Two generations of ND^{Pxl}, the first built on a generation 2 dendron (4 Hydroxyl groups) and the second on a generation 3 dendron (8 Hydroxyl groups) were tested using the PyVT1-luc mammary tumor model described above. The first formulation of ND^{Pxl} was administered and compared to Abraxane retro-orbitally and demonstrated significant inhibition of tumor growth in the low dose (3.13mg/kg qdx6) group that performed similarly to the Abraxane treated group at a higher dose (25mg/kg qdx3). Interestingly, the higher dose of ND^{Pxl} did not elicit a significant response. ND^{Pxl} had solubility issues at the highest concentration and required dissolution in 40% DMSO for injection, leading us to conclude that this construct may not be effectively delivering PXL as a result of its relative insolubility in the murine vasculature. The second formulation had somewhat improved solubility, but adverse outcomes from i.v. injection dictated delivery via i.p. injection.

The overall goal of this project was to use the quantitative estimates of tumor associated MMP activity determined with ND^{PB} to assess the delivery of PXL prodrug from ND^{Pxl}. The second formulation ND$_3^{Pxl}$ was built on an azide core generation 3 dendron and was successfully linked to a second formulation of ND$_3^{PB}$ built on an acetylene core generation 3 dendron by click chemistry creating ND$_3^{PXL}$ND$_3^{PB}$. Before initiating the second treatment study, ND$_3^{PXL}$ND$_3^{PB}$ was administered to tumor bearing mice yielding an estimate that 25% of the beacon was activated in PyVT1 mammary tumors. To our knowledge, this is the first time delivery of a therapy has been visualized using a multifunctional dendron approach.

Therapeutic delivery of PXL using ND$_3^{PXL}$ND$_3^{PB}$ was not feasible due to the high concentrations of PXL required and the cost of equally high concentrations of optical fluorophores. Instead, ND$_3^{Pxl}$ was expanded to a size similar to ND$_3^{PXL}$ND$_3^{PB}$ by clicking a non-functionalized G3 alkyne dendron (D$_3$) to its core to form ND$_3^{PXL}$D$_3$. The addition of this compound improved the solubility of ND$_3^{Pxl}$ slightly by reducing the amount of DMSO required to keep ND$_3^{PXL}$ in solution to 30%. However, ND$_3^{Pxl}$D injected retro-orbitally at either 25 or 12.5 mg/kg caused morbidity in 2/5 mice, possibly due to the generation of occlusive emboli. Thus, ND$_3^{Pxl}$D was injected intraperitoneally at 25, 12.5, and 4.1mg/kg to improve solubility and delivery.

Luminescence imaging, tumor volume by calipers, and FDG-PET were used to monitor tumor response to therapy. Luminescence imaging appeared to be more sensitive than calipers for early detection of tumor response to therapy; however, long-term therapy response was not distinguishable due to saturation of signal in larger tumors. Caliper measurements were a better means to determine tumor

response to therapy and displayed the most robust difference between treatment groups and for calculating tumor growth inhibition. FDG-PET is the current standard for determining tumor metabolic activity, but it has yet to be determined if tumor metabolic activity increases or decreases upon therapy administration for many types of chemotherapeutics. The SUV values calculated in all studies with $ND_3{}^{Pxl}D_3$ were unable to determine tumor response in an effective manner.

Treatment of mice with $ND_3{}^{Pxl}D$ at either 25 or 12.5 mg/kg doses demonstrated robust responses in their respective treatment groups outperforming the Abraxane treated animals at the same doses. However, there was one animal in each group that didn't respond as well as the other two animals indicating that an optimal dose may be somewhere in between this range. It is important to note that the study with $ND_3{}^{Pxl}ND^{PB}$ indicated that 25% of the therapeutic was being delivered. The variation in tumor response may be a result of lower MMP activity in the tumors of the more poorly responding mice. In future studies, it would be useful to incorporate $ND_3{}^{Pxl}ND^{PB}$ into the treatment regimen to give readouts of MMP activity as an indication of response to therapy and to monitor delivery of PXL throughout the study.

An overarching goal of this study was to deliver toxic doses of PXL specifically to the tumor by virtue of their MMP9 proteolytic activity, thus reducing the exposure of normal tissue, including the nervous system to the toxic effects of PXL. In this pilot study, peripheral neuropathy demonstrated no significant difference in mouse treatment groups (data not shown), suggesting that longer-term studies may be required to elicit responses in the basic tests administered.

However, evaluation of the Abraxane and ND$_3^{Pxl}$D groups at the same dose using the rotorod and hot-plate response tests revealed a trend towards a greater effect in the Abraxane treated mice. One day after the last treatment was administered, there was a longer lag time in the hot-plate assay for the Abraxane group compared to the ND$_3^{Pxl}$D treated group. Rotorod tests were deemed to be inconclusive as tumor size in the control mice caused biased results. A long-term study must be performed with animals not bearing tumors and administered ND$_3^{Pxl}$D versus Abraxane with both positive and negative control groups for a conclusive analysis.

Applications Targeting MMP Activity and Future Directions

Imaging of MMPs, or other proteinases, in cancer has many potential applications. Most obvious is perhaps to take advantage of the catalytic nature of proteinases as a means to enhance the sensitivity of screening methods for early cancer detection. For example, the proteinase-based optical beacons generated by the Weissleder and Matrisian groups demonstrated enhanced signal in a murine model of adenomatous polyps [125, 126]. The current use of screening colonoscopy to detect and remove colonic polyps could be enhanced by the addition of an MMP-based contrast agent to enhance detection of smaller polyps. The adaptation of endoscopes to include excitation wavelengths compatible with NIR probes has been achieved [127], making this one of the most translatable applications of MMP-based proteolytic beacons.

Utilizing the large amount of information published on the expression patterns of MMPs in normal vs. pathological tissues, and the association of various

MMP family members with overall survival in specific cancer types [51], represents an additional application of MMP-based imaging probes. It is reasonable to hypothesize that the presence or absence of a signal referable to the activity of a specific MMP would be a useful approach to more accurate diagnosis, staging, or prognosis of a suspicious mass. Similar to the use of FDG-PET as an indicator of the metabolic activity of a suspicious lesion [128], the application of PET, SPECT, or MRI-based probes that provide a read-out of the relative levels of MMP-specific activity may aid in treatment decisions. Optical detection approaches are relatively insensitive compared to PET/SPECT probes and PET/SPECT versions of probes could be more readily used in the clinic. Utilizing these types of probes would require additional preclinical and translational activities for implementation. Taking advantage of animal models of cancer, the relationship between MMP protein or transcript expression as measured by techniques such as immunohistochemistry and *in situ* hybridization, and the activity of that MMP in intact tumor tissue *in vivo*, can be tested to provide a link between the published data on human pathological specimens and the application of this knowledge to minimally or non-invasive imaging techniques. The validation of these types of probes as biomarkers for tumor stage or as a predictive/prognostic indicators would require appropriate prospective clinical trials, although it is noted that despite the widespread use of FDG-PET it has not yet achieved this level of evidence [129].

MMP-based imaging probes may also provide a means to assess response to therapy. Many of these probes were designed for the pharmacokinetic or pharmacodynamic assessment of synthetic MMPIs, and would still provide an

essential tool for the development of such agents by dictating appropriate doses and identifying an appropriate cohort of patients. Perhaps a more broadly applicable use of these imaging agents is as an indicator of alterations in tumor physiology as a result of drug treatment. MMP family members are downstream effectors of a variety of pathways that are targets of cancer therapy, including EGF and VEGF signaling cascades [38]. Proteolysis of the ECM is considered to be an essential step in tumor growth and in tumor angiogenesis. An imaging agent that detects changes in proteolytic activity as a surrogate for effects of processes that alter tumor growth or angiogenesis would provide an early indicator of tumor responsiveness for a specific drug, and an indication of whether further treatment with that agent is likely to result in an efficacious response. Preclinical studies of MMP-based contrast agents for this purpose are a first step to determine whether a change in MMP activity, in general or for specific family members, is capable of predicting response to targeted cancer agents.

A particularly promising application of MMP-based imaging probes is in conjunction with the selective delivery of a therapeutic agent as part of a targeted pro-drug approach as described in Chapter 4. There have been several examples of protease-activated prodrugs designed to delivery toxic agents specifically to tumor cells, reducing dose-limiting toxic side effects to normal tissues. Albright et al described a prodrug approach that incorporates doxorubicin (DOX) attachment to MMP2 and 9 substrates that showed much higher therapeutic indexes than DOX alone in MMP-expressing xenografts [130]. Other targeted approaches utilize MMP activated carrier-peptide conjugates, MMP activated peptide and protein delivery,

MMP activated DNA delivery, as well as ligand and liposome targeting that are nicely reviewed by Vartak et al [131]. The addition of a proteolytic beacon, using the same protease "switch", with proteinase-activated prodrugs provides the opportunity to monitor drug deliver efficiency. This approach is particularly amenable for the development of multifunctional nanoparticles that permit the assembly of both prodrug and proteinase beacon on the same particle. The next step could be to incorporate a central core that allows for the attachment of multiple different dendrons with specific functionalities to elicit information about the tumor. It would be fairly straightforward to design next generation NDs that would provide signals for apoptosis, targeting ligands, or that contain SPECT/MRI/PET agents for colocalization of imaging modalities.

The future of medicine lies in nanotechnology with its' limits only being that of the human mind.
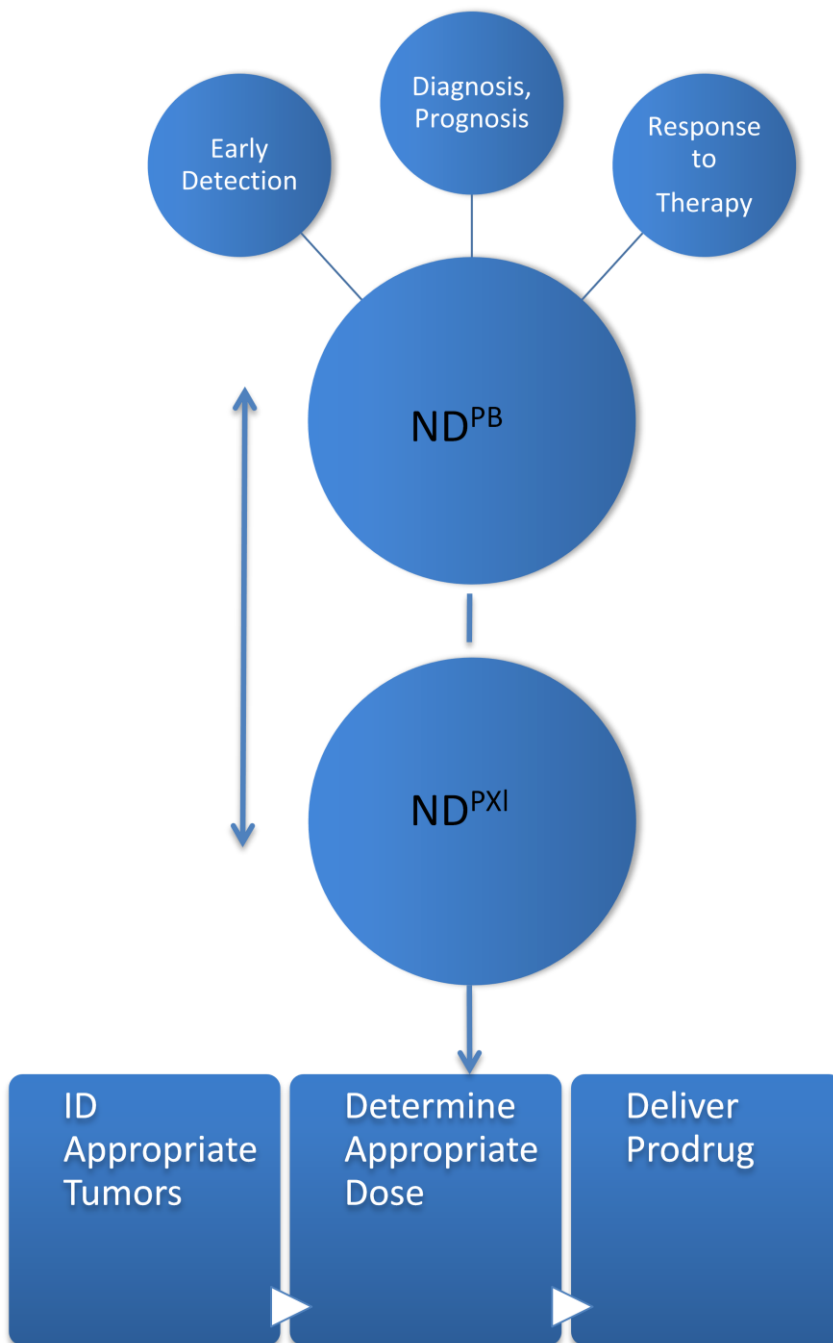
Figure 32: Diagram of possible applications of ND proteolytic beacons and prodrugs

Conclusions

The results of my thesis demonstrated:

- PB-M7NIR is the first of the dendrimeric near-infrared fluorescent probes designed for the *in vivo* detection and imaging of MMP7 activity.

- The intravenous administration of PB-M7NIR allowed for the sensitive and selective visualization and localization of MMP7 activity in whole animals and in tissue sections.

- A novel synthetic application to building nanodendron proteolytic beacons and prodrugs

- ND^{PB} is the first dendron type near infrared probe designed to detect MMP9 activity *in vivo*.

- Linked $ND_3^{Pxl}ND_3^{PB}$ to provide estimated delivery of PXL prodrug therapies.

- ND_3^{Pxl} performed better than Abraxane therapy in a mouse model of breast cancer and indicates a trend towards reducing peripheral neuropathic side-effects of PXL therapies.

REFERENCES

1. Edwards, B.K. et al. Annual report to the nation on the status of cancer, 1975-2006, featuring colorectal cancer trends and impact of interventions (risk factors, screening, and treatment) to reduce future rates. *Cancer* (2009).

2. Jemal, A. et al. Cancer statistics, 2005. *CA: A Cancer Journal for Clinicians* **55**, 10-30 (2005).

3. Weinberg, R.A. The Biology of Cancer. (Garland Science, Taylor & Francis Group, New York; 2007).

4. Coussens, L.M., Fingleton, B. & Matrisian, L.M. Matrix metalloproteinase inhibitors and cancer: trials and tribulations. *Science* **295**, 2387-2392 (2002).

5. Mayoclinic (2009) www.mayoclinic.com

6. Mekhail, T.M. & Markman, M. Paclitaxel in cancer therapy. *Expert opinion on pharmacotherapy* **3**, 755-766 (2002).

7. Orr, G.A., Verdier-Pinard, P., McDaid, H. & Horwitz, S.B. Mechanisms of Taxol resistance related to microtubules. *Oncogene* **22**, 7280-7295 (2003).

8. Rivera, E. et al. Phase II study of paclitaxel in patients with metastatic breast carcinoma refractory to standard chemotherapy. *Cancer* **89**, 2195-2201 (2000).

9. Holmes, F.A. et al. Phase II trial of taxol, an active drug in the treatment of metastatic breast cancer. *J Natl Cancer Inst* **83**, 1797-1805 (1991).

10. Sledge, G.W. et al. Phase III trial of doxorubicin, paclitaxel, and the combination of doxorubicin and paclitaxel as front-line chemotherapy for metastatic breast cancer: an intergroup trial (E1193). *J Clin Oncol* **21**, 588-592 (2003).

11. Jassem, J. et al. Doxorubicin and paclitaxel versus fluorouracil, doxorubicin and cyclophosphamide as first-line therapy for women with advanced breast cancer: long-term analysis of the previously published trial. *Onkologie* **32**, 468-472 (2009).

12. Biganzoli, L. et al. Doxorubicin and paclitaxel versus doxorubicin and cyclophosphamide as first-line chemotherapy in metastatic breast cancer: The European Organization for Research and Treatment of Cancer 10961 Multicenter Phase III Trial. *J Clin Oncol* **20**, 3114-3121 (2002).

13.   Jassem, J. et al. Doxorubicin and paclitaxel versus fluorouracil, doxorubicin, and cyclophosphamide as first-line therapy for women with metastatic breast cancer: final results of a randomized phase III multicenter trial. *J Clin Oncol* **19**, 1707-1715 (2001).

14.   Henderson, I.C. et al. Improved outcomes from adding sequential Paclitaxel but not from escalating Doxorubicin dose in an adjuvant chemotherapy regimen for patients with node-positive primary breast cancer. *J Clin Oncol* **21**, 976-983 (2003).

15.   Mamounas, E.P. et al. Paclitaxel after doxorubicin plus cyclophosphamide as adjuvant chemotherapy for node-positive breast cancer: results from NSABP B-28. *J Clin Oncol* **23**, 3686-3696 (2005).

16.   Scripture, C.D., Figg, W.D. & Sparreboom, A. Peripheral neuropathy induced by Paclitaxel: recent insights and future perspectives. *Current neuropharmacology* **4**, 165-172 (2006).

17.   Lee, J.J. & Swain, S.M. Peripheral neuropathy induced by microtubule-stabilizing agents. *J Clin Oncol* **24**, 1633-1642 (2006).

18.   Sparreboom, A. et al. Comparative preclinical and clinical pharmacokinetics of a cremophor-free, nanoparticle albumin-bound paclitaxel (ABI-007) and paclitaxel formulated in Cremophor (Taxol). *Clin Cancer Res* **11**, 4136-4143 (2005).

19.   Gralow, J. et al. Novel taxane formulations in the treatment of breast cancer: a thought leader discussion and consensus roundtable. *Clin Breast Cancer* **8**, 33-37 (2008).

20.   Gradishar, W.J. et al. Phase III trial of nanoparticle albumin-bound paclitaxel compared with polyethylated castor oil-based paclitaxel in women with breast cancer. *J Clin Oncol* **23**, 7794-7803 (2005).

21.   Auzenne, E. et al. Superior therapeutic profile of poly-L-glutamic acid-paclitaxel copolymer compared with taxol in xenogeneic compartmental models of human ovarian carcinoma. *Clin Cancer Res* **8**, 573-581 (2002).

22.   Yang, T. et al. Antitumor effect of paclitaxel-loaded PEGylated immunoliposomes against human breast cancer cells. *Pharm Res* **24**, 2402-2411 (2007).

23.   Lee, H., Lee, K. & Park, T.G. Hyaluronic acid-paclitaxel conjugate micelles: synthesis, characterization, and antitumor activity. *Bioconjug Chem* **19**, 1319-1325 (2008).

24. Majoros, I.J., Myc, A., Thomas, T., Mehta, C.B. & Baker, J.R., Jr. PAMAM dendrimer-based multifunctional conjugate for cancer therapy: synthesis, characterization, and functionality. *Biomacromolecules* **7**, 572-579 (2006).

25. Guy, C.T., Cardiff, R.D. & Muller, W.J. Induction of mammary tumors by expression of polyomavirus middle T oncogene: a transgenic mouse model for metastatic disease. *Molecular and Cellular Biology* **12**, 954-961 (1992).

26. Qiu, T.H. et al. Global expression profiling identifies signatures of tumor virulence in MMTV-PyMT-transgenic mice: correlation to human disease. *Cancer Res* **64**, 5973-5981 (2004).

27. Lin, E.Y. et al. Progression to malignancy in the polyoma middle T oncoprotein mouse breast cancer model provides a reliable model for human diseases. *American Journal of Pathology* **163**, 2113-2126 (2003).

28. Martin, M.D. et al. Effect of ablation or inhibition of stromal matrix metalloproteinase-9 on lung metastasis in a breast cancer model is dependent on genetic background. *Cancer Res* **68**, 6251-6259 (2008).

29. Woessner, J.F. & Nagase, H. Matrix Metalloproteinases and TIMPs. (Oxford University Press,Inc., New York; 2000).

30. Massova, I., Kotra, L.P., Fridman, R. & Mobashery, S. Matrix metalloproteinases: structures, evolution, and diversification. *FASEB Journal* **12**, 1075-1095 (1998).

31. Sternlicht, M.D. & Werb, Z. How matrix metalloproteinases regulate cell behavior. *Annual Review of Cell and Developmental Biology* **17**, 463-516 (2001).

32. Nagase, H., Visse, R. & Murphy, G. Structure and function of matrix metalloproteinases and TIMPs. *Cardiovasc Res* **69**, 562-573 (2006).

33. McKerrow, J.H. et al. A functional proteomics screen of proteases in colorectal carcinoma. *Molecular Medicine* **6**, 450-460 (2000).

34. Nelson, A.R., Fingleton, B., Rothenberg, M.L. & Matrisian, L.M. Matrix metalloproteinases: biologic activity and clinical implications. *Journal of Clinical Oncology* **18**, 1135-1149 (2000).

35. MacDougall, J.R., Bani, M.R., Lin, Y., Rak, J. & Kerbel, R.S. The 92-kDa gelatinase B is expressed by advanced stage melanoma cells: suppression by somatic cell hybridization with early stage melanoma cell. *Cancer Research* **55**, 4174-4181 (1995).

36. Vaisanen, A., Tuominen, H., Kallioinen, M. & Turpeenniemihujanen, T. Matrix metalloproteinase-2 (72 kd type IV collagenase) expression occurs in the early stage of human melanocytic tumour progression and may have prognostic value. *Journal of Pathology* **180**, 283-289 (1996).

37. Davies, B. et al. Levels of matrix metalloproteases in bladder cancer correlate with tumor grade and invasion. *Cancer Research* **53**, 5365-5369 (1993).

38. Sternlicht, M.D. & Bergers, G. Matrix metalloproteinases as emerging targets in anticancer therapy: status and prospects. *Emerging Therapeutic Targets* **4**, 609-633 (2000).

39. Martin, M.D. & Matrisian, L.M. The other side of MMPs: Protective roles in tumor progression. *Cancer Metastasis Rev* (2007).

40. Wilson, C.L., Matrisian, L.M., Parks, W.C. & Mecham, R.P. in Matrix Metalloproteinases 149-184 (Academic Press, San Diego; 1998).

41. Wagenaar-Miller, R.A., Gorden, L. & Matrisian, L.M. Matrix metalloproteinases in colorectal cancer: is it worth talking about? *Cancer Metastasis Review* **23**, 119-135 (2004).

42. Newell, K.J., Witty, J.P., Rodgers, W.H. & Matrisian, L.M. Expression and localization of matrix-degrading metalloproteinases during colorectal tumorigenesis. *Molecular Carcinogenesis* **10**, 199-206 (1994).

43. Shattuck-Brandt, R.L., Lamps, L.W., Heppner Goss, K.J., DuBois, R.N. & Matrisian, L.M. Matrilysin and cyclooxygenase-2 are differentially expressed in intestinal and colorectal neoplasms. *Molecular Carcinogenesis* **24**, 177-187 (1999).

44. Yamashita, K., Azumano, I., Mai, M. & Okada, Y. Expression and tissue localization of matrix metalloproteinase 7 (matrilysin) in human gastric carcinomas Implications for vessel invasion and metastasis. *International Journal of Cancer* **79**, 187-194 (1998).

45. Mylona, E. et al. The multifunctional role of the immunohistochemical expression of MMP-7 in invasive breast cancer 1. *APMIS* **113**, 246-255 (2005).

46. Rudolph-Owen, L.A., Chan, R., Muller, W.J. & Matrisian, L.M. The matrix metalloproteinase matrilysin influences early-stage mammary tumorigenesis. *Cancer Research* **58**, 5500-5506 (1998).

47. Leeman, M.F., Curran, S. & Murray, G.I. New insights into the roles of matrix metalloproteinases in colorectal cancer development and progression. *J Pathol* **201**, 528-534 (2003).

48. Wilson, C.L., Heppner, K.J., Labosky, P.A., Hogan, B.L. & Matrisian, L.M. Intestinal tumorigenesis is suppressed in mice lacking the metalloproteinase matrilysin. *Proc Natl Acad Sci U S A* **94**, 1402-1407 (1997).

49. Liotta, L.A. et al. Metastatic potential correlates with enzymatic degradation of basement membrane collagen. *Nature* **284**, 67-68 (1980).

50. Lauer-Fields, J.L., Sritharan, T., Stack, M.S., Nagase, H. & Fields, G.B. Selective hydrolysis of triple-helical substrates by matrix metalloproteinase-2 and -9. *Journal Biological Chemistry* **278**, 18140-18145 (2003).

51. Martin, M.D. & Matrisian, L.M. Matrix metalloproteinases as prognostic factors for cancer. *Clinical Lab.Invest.* **28**, 16-18 (2005).

52. Coussens, L.M. & Werb, Z. Matrix metalloproteinases and the development of cancer. *Chemistry and Biology* **3**, 895-904 (1996).

53. McCawley, L.J. & Matrisian, L.M. Matrix metalloproteinases: multifunctional contributors to tumor progression. *Molecular Medicine Today* **6**, 149-156 (2000).

54. Bergers, G. et al. Matrix metalloproteinase-9 triggers the angiogenic switch during carcinogenesis. *Nature Cell Biology* **2**, 737-744 (2000).

55. Overall, C.M. & Dean, R.A. Degradomics: systems biology of the protease web. Pleiotropic roles of MMPs in cancer. *Cancer Metastasis Rev* **25**, 69-75 (2006).

56. Lopez-Otin, C. & Overall, C.M. Protease degradomics: a new challenge for proteomics. *Nature Reviews Molecular Cell Biology* **3**, 509-519 (2002).

57. Scherer, R.L., McIntyre, J.O. & Matrisian, L.M. Imaging matrix metalloproteinases in cancer. *Cancer Metastasis Rev* **27**, 679-690 (2008).

58. Albert, A. Chemical aspects of selective toxicity. *Nature* **182**, 421-422 (1958).

59. Rautio, J. et al. Prodrugs: design and clinical applications. *Nature reviews* **7**, 255-270 (2008).

60. Wu, K.-M. A New Classification of Prodrugs: Regulatory Perspectives. *Pharmaceuticals* **2**, 77-81 (2009).

61. Knox, R.J. & Connors, T.A. Prodrugs in Cancer Chemotherapy. *Pathol Oncol Res* **3**, 309-324 (1997).

62. Kline, T., Torgov, M.Y., Mendelsohn, B.A., Cerveny, C.G. & Senter, P.D. Novel antitumor prodrugs designed for activation by matrix metalloproteinases-2 and -9. *Molecular pharmaceutics* **1**, 9-22 (2004).

63. Seligson, A.L., Terry, R.C., Bressi, J.C., Douglass, J.G., 3rd & Sovak, M. A new prodrug of paclitaxel: synthesis of Protaxel. *Anticancer Drugs* **12**, 305-313 (2001).

64. Skwarczynski, M., Hayashi, Y. & Kiso, Y. Paclitaxel Prodrugs: Toward Smarter Delivery of Anticancer Agents. *Journal of Medicinal Chemistry* **49**, 7253-7269 (2006).

65. Feynman, R. in Miniaturization. (ed. H.D. Gilbert) (Reinhold, New York; 1961).

66. Ferrari, M. Cancer nanotechnology: opportunities and challenges. *Nature Reviews Cancer* **5**, 161-171 (2005).

67. Sanvicens, N. & Marco, M.P. Multifunctional nanoparticles--properties and prospects for their use in human medicine. *Trends in biotechnology* **26**, 425-433 (2008).

68. Lee, C.C., MacKay, J.A., Frechet, J.M. & Szoka, F.C. Designing dendrimers for biological applications. *Nat Biotechnol* **23**, 1517-1526 (2005).

69. Gillies, E.R. & Frechet, M.J. Dendrimers and dendritic polymers in drug delivery. *Drug Discovery Today* **10**, 35-43 (2005).

70. Samuelson, L.E., Sebby, K.B., Walter, E.D., Singel, D.J. & Cloninger, M.J. EPR and affinity studies of mannose-TEMPO functionalized PAMAM dendrimers. *Organic & biomolecular chemistry* **2**, 3075-3079 (2004).

71. Kolb, H.C., Finn, M.G. & Sharpless, K.B. Click Chemistry: Diverse Chemical Function from a Few Good Reactions. *Angewandte Chemie (International ed* **40**, 2004-2021 (2001).

72. van Dijk, M., Rijkers, D.T., Liskamp, R.M., van Nostrum, C.F. & Hennink, W.E. Synthesis and applications of biomedical and pharmaceutical polymers via click chemistry methodologies. *Bioconjug Chem* **20**, 2001-2016 (2009).

73. Chan, T.R., Hilgraf, R., Sharpless, K.B. & Fokin, V.V. Polytriazoles as copper(I)-stabilizing ligands in catalysis. *Org Lett* **6**, 2853-2855 (2004).

74. Dirksen, A. & Dawson, P.E. Rapid oxime and hydrazone ligations with aromatic aldehydes for biomolecular labeling. *Bioconjug Chem* **19**, 2543-2548 (2008).

75. Dirksen, A., Hackeng, T.M. & Dawson, P.E. Nucleophilic catalysis of oxime ligation. *Angewandte Chemie (International ed* **45**, 7581-7584 (2006).

76. Cho, K., Wang, X., Nie, S., Chen, Z.G. & Shin, D.M. Therapeutic nanoparticles for drug delivery in cancer. *Clin Cancer Res* **14**, 1310-1316 (2008).

77. Nie, S., Xing, Y., Kim, G.J. & Simons, J.W. Nanotechnology applications in cancer. *Annu Rev Biomed Eng* **9**, 257-288 (2007).

78. Van de Wiele, C. & Oltenfreiter, R. Imaging probes targeting matrix metalloproteinases. *Cancer Biother Radiopharm* **21**, 409-417 (2006).

79. Weissleder, R. & Ntziachristos, V. Shedding light onto live molecular targets. *Nat Med* **9**, 123-128 (2003).

80. McIntyre, J.O. et al. Development of a novel fluorogenic proteolytic beacon for in vivo detection and imaging of tumour-associated matrix metalloproteinase-7 activity. *Biochemical Journal* **377**, 617-628 (2004).

81. McIntyre, J.O. & Matrisian, L.M. Molecular imaging of proteolytic activity in cancer. *Journal of Cellular Biochemistry* **90**, 1087-1097 (2003).

82. Tsien, R.Y. Building and breeding molecules to spy on cells and tumors. *FEBS Letters* **579**, 927-932 (2005).

83. Weissleder, R., Tung, C.H., Mahmood, U. & Bogdanov, A., Jr. In vivo imaging of tumors with protease-activated near-infrared fluorescent probes. *Nature Biotechnology* **17**, 375-378 (1999).

84. Bremer, C., Tung, C.H. & Weissleder, R. In vivo molecular target assessment of matrix metalloproteinase inhibition. *Nature Medicine* **7**, 743-748 (2001).

85. Shalinsky, D.R. et al. Broad antitumor and antiangiogenic activities of AG3340, a potent and selective MMP inhibitor undergoing advanced oncology clinical trials. *Annals of the New York Academy of Sciences* **878**, 236-270 (1999).

86. Kubota, K. From tumor biology to clinical Pet: a review of positron emission tomography (PET) in oncology. *Ann Nucl Med* **15**, 471-486 (2001).

87. Fonovic, M. & Bogyo, M. Activity-based probes as a tool for functional proteomic analysis of proteases. *Expert review of proteomics* **5**, 721-730 (2008).

88.   Jiang, T. et al. Tumor imaging by means of proteolytic activation of cell-penetrating peptides. *Proceedings of the National Academy of Sciences of the United States of America* **101**, 17867-17872 (2004).

89.   Welch, A.R. et al. Purification of human matrilysin produced in escherichia coli and characterization using a new optimized fluorogenic peptide substrate. *Archives of Biochemistry and Biophysics* **324**, 59-64 (1995).

90.   Wilson, C.L., Heppner, K.J., Labosky, P.A., Hogan, B.L.M. & Matrisian, L.M. Intestinal tumorigenesis is suppressed in mice lacking the metalloproteinase matrilysin. *Proceedings of the National Academy of Sciences of the United States of America* **94**, 1402-1407 (1997).

91.   Fingleton, B., Powell, W.C., Crawford, H.C., Couchman, J.R. & Matrisian, L.M. A rat monoclonal antibody that recognizes pro- and active matrix metalloproteinase-7 indicates polarized expression in vivo. *Hybridoma* (2008)

92.   Acuff, H.B., Carter, K.J., Fingleton, B., Gorden, D.L. & Matrisian, L.M. Matrix metalloproteinase-9 from bone marrow-derived cells contributes to survival but not growth of tumor cells in the lung microenvironment. *Cancer Research* **66**, 259-266 (2006).

93.   Wu, P. et al. Multivalent, bifunctional dendrimers prepared by click chemistry. *Chemical communications (Cambridge, England)*, 5775-5777 (2005).

94.   Tung, C.H., Mahmood, U., Bredow, S. & Weissleder, R. In vivo imaging of proteolytic enzyme activity using a novel molecular reporter. *Cancer Research* **60**, 4953-4958 (2000).

95.   Petrovsky, A., Schellenberger, E., Josephson, L., Weissleder, R. & Bogdanov, A., Jr. Near-infrared fluorescent imaging of tumor apoptosis. *Cancer Research* **63**, 1936-1942 (2003).

96.   Ntziachristos, V., Bremer, C. & Weissleder, R. Fluorescence imaging with near-infrared light: new technological advances that enable in vivo molecular imaging. *Eur Radiol* **13**, 195-208 (2003).

97.   Achilefu, S. et al. Synthesis, in vitro receptor binding, and in vivo evaluation of fluorescein and carbocyanine peptide-based optical contrast agents. *Journal of Medicinal Chemistry* **45**, 2003-2015 (2002).

98.   Achilefu, S. Lighting up tumors with receptor-specific optical molecular probes. *Technology in Cancer Research and Treatment* **3**, 393-409 (2004).

99. Chen, Y. et al. Metabolism-enhanced tumor localization by fluorescence imaging: in vivo animal studies. *Optics Letters* **28**, 2070-2072 (2003).

100. Bremer, C., Bredow, S., Mahmood, U., Weissleder, R. & Tung, C.H. Optical imaging of matrix metalloproteinase-2 activity in tumors: feasibility study in a mouse model. *Radiology* **221**, 523-529 (2001).

101. Bremer, C. et al. Optical imaging of spontaneous breast tumors using protease sensing 'smart' optical probes. *Invest Radiol* **40**, 321-327 (2005).

102. Pham, W., Choi, Y., Weissleder, R. & Tung, C.H. Developing a peptide-based near-infrared molecular probe for protease sensing. *Bioconjug Chem* **15**, 1403-1407 (2004).

103. Wu, P. & Brand, L. Resonance energy transfer: methods and applications. *Anal Biochem* **218**, 1-13 (1994).

104. Gaind, V., Webb, K.J., Kularatne, S. & Bouman, C.A. Towards in vivo imaging of intramolecular fluorescence resonance energy transfer parameters. *Journal of the Optical Society of America* **26**, 1805-1813 (2009).

105. Packard, B.Z., Toptygin, D.D., Komoriya, A. & Brand, L. Characterization of fluorescence quenching in bifluorophoric protease substrates. *Biophysical chemistry* **67**, 167-176 (1997).

106. Acuff, H.B. et al. Analysis of host- and tumor-derived proteinases using a custom dual species microarray reveals a protective role for stromal matrix metalloproteinase-12 in non-small cell lung cancer. *Cancer Res* **66**, 7968-7975 (2006).

107. O'Reilly, M.S. et al. Angiostatin: a novel angiogenesis inhibitor that mediates the suppression of metastases by a Lewis lung carcinoma. *Cell* **79**, 315-328 (1994).

108. Volk, L.D. et al. Nab-paclitaxel efficacy in the orthotopic model of human breast cancer is significantly enhanced by concurrent anti-vascular endothelial growth factor A therapy. *Neoplasia* **10**, 613-623 (2008).

109. Jeremiah, A.J., Finn, M.G., Jeffrey, T.K. & Nicholas, J.T. Construction of Linear Polymers, Dendrimers, Networks, and Other Polymeric Architectures by Copper-Catalyzed Azide-Alkyne Cycloaddition ldquoClickrdquo Chemistry. *Macromolecular Rapid Communications* **29**, 1052-1072 (2008).

110. Weissleder, R. A clearer vision for in vivo imaging. *Nature Biotechnology* **19**, 316-317 (2001).

111. Kircher, M.F., Weissleder, R. & Josephson, L. A dual fluorochrome probe for imaging proteases. *bioconjug chem* **15**, 242-248 (2004).

112. Boas, U. & Heegaard, P.M.H. Dendrimers in drug research. *Chemical Society Reviews* **33**, 43-63 (2004).

113. Giambernardi, T.A. et al. Overview of matrix metalloproteinase expression in cultured human cells. *Matrix Biology* **16**, 483-496 (1998).

114. Fang, J., Sawa, T. & Maeda, H. Factors and mechanism of "EPR" effect and the enhanced antitumor effects of macromolecular drugs including SMANCS. *Adv Exp Med Biol* **519**, 29-49 (2003).

115. Maeda, H., Sawa, T. & Konno, T. Mechanism of tumor-targeted delivery of macromolecular drugs, including the EPR effect in solid tumor and clinical overview of the prototype polymeric drug SMANCS. *J Control Release* **74**, 47-61 (2001).

116. Witty, J.P. et al. Modulation of matrilysin levels in colon carcinoma cell lines affects tumorigenicity in vivo. *Cancer Research* **54**, 4805-4812 (1994).

117. Haro, H. et al. Matrix metalloproteinase-7-dependent release of tumor necrosis factor-alpha in a model of herniated disc resorption. *Journal of Clinical Investigation* **105**, 143-150 (2000).

118. Haro, H. et al. Matrix metalloproteinase-3-dependent generation of a macrophage chemoattractant in a model of herniated disc resorption. *Journal of Clinical Investigation* **105**, 133-141 (2000).

119. Nagashima, Y. et al. Expression of matrilysin in vascular endothelial cells adjacent to matrilysin-producing tumors. *International Journal of Cancer* **72**, 441-445 (1997).

120. Shapiro, S.D., Campbell, E.J., Senior, R.M. & Welgus, H.G. Proteinases secreted by human mononuclear phagocytes. *Journal of Rheumatology* **18 Suppl. 27**, 95-98 (1991).

121. Moser, A.R., Pitot, H.C. & Dove, W.F. A dominant mutation that predisposes to multiple intestinal neoplasia in the mouse. *Science* **247**, 322-324 (1990).

122. Goss, K.J., Brown, P.D. & Matrisian, L.M. Differing effects of endogenous and synthetic inhibitors of metalloproteinases on intestinal tumorigenesis. *International Journal of Cancer* **78**, 629-635 (1998).

123. Fingleton, B. Matrix metalloproteinases: roles in cancer and metastasis. *Front Biosci* **11**, 479-491 (2006).

124. Harrell, P.C., McCawley, L.J., Fingleton, B., McIntyre, J.O. & Matrisian, L.M. Proliferative effects of apical, but not basal, matrix metalloproteinase-7 activity in polarized MDCK cells. *Exp.Cell Res.* **303**, 308-320 (2005).

125. Marten, K. et al. Detection of dysplastic intestinal adenomas using enzyme-sensing molecular beacons in mice. *Gastroenterology* **122**, 406-414 (2002).

126. Scherer, R., VanSaun, M., McIntyre, J.O. & Matrisian, L.M. Optical imaging of matrix metalloproteinase-7 activity in vivo using a proteolytic nanobeacon. *Journal Biomedical Optics*, submitted (2007).

127. Funovics, M.A. et al. Miniaturized multichannel near infrared endoscope for mouse imaging. *Mol.Imaging* **2**, 350-357 (2003).

128. Kawada, S. et al. [Cancer screening with PET: advantages and limitations]. *Rinsho Byori* **55**, 656-667 (2007).

129. Kelloff, G.J. et al. Progress and promise of FDG-PET imaging for cancer patient management and oncologic drug development. *Clin Cancer Res* **11**, 2785-2808 (2005).

130. Albright, C.F. et al. Matrix metalloproteinase-activated doxorubicin prodrugs inhibit HT1080 xenograft growth better than doxorubicin with less toxicity. *Mol Cancer Ther* **4**, 751-760 (2005).

131. Vartak, D.G. & Gemeinhart, R.A. Matrix metalloproteases: underutilized targets for drug delivery. *J Drug Target* **15**, 1-20 (2007).